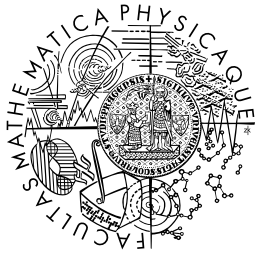

FACULTY
OF MATHEMATICS
AND PHYSICS
Charles University

MASTER THESIS

Jaroslav Hofierka

Convergence of the embedding scheme

Institute of Theoretical Physics

Supervisor of the master thesis: Mgr. Jiří Klimeš, Ph.D.
Study programme: Physics
Study branch: Theoretical Physics

Prague 2019

I declare that I carried out this master thesis independently, and only with the cited sources, literature and other professional sources.

I understand that my work relates to the rights and obligations under the Act No. 121/2000 Sb., the Copyright Act, as amended, in particular the fact that the Charles University has the right to conclude a license agreement on the use of this work as a school work pursuant to Section 60 subsection 1 of the Copyright Act.

In ..... date ..... signature of the author

I would like to thank my supervisor, Jiří Klimeš, for his guidance and his valuable advice. Also, I am grateful to Marcin for allowing me to use his RPA code. Also the rest of the group, Sirous and Lu, for their help and positive attitude. Finally, I am grateful to my family and my fiancée for their love and support.

Title: Convergence of the embedding scheme

Author: Jaroslav Hofierka

Institute: Institute of Theoretical Physics

Supervisor: Mgr. Jiří Klimeš, Ph.D., Department of Chemical Physics and Optics

Abstract: To obtain accurate adsorption energies of molecules on surfaces is a challenging task as the methods with sufficient accuracy are too computationally demanding to be applied to the systems of interest. Embedding theories provide a natural remedy: focus the computation on a small region and incorporate the effects of the environment. In this thesis, embedding schemes and the response of many-electron systems to an adsorbed impurity are investigated. To this end, two approaches are used: tight-binding and ab initio. In the tight-binding method, the single-particle Green's function formalism is studied and explicit expressions for Green's functions of various one- and two-dimensional models are obtained. Using this formalism, we study qualitatively the local density of states and adsorption energies. In the second part of this thesis, state-of-the-art ab initio methods are employed to study convergence of the subtractive embedding scheme for adsorption energies of small closed-shell systems on two-dimensional graphene and hexagonal boron nitride. The efficiency and applicability of the scheme are assessed for neon and hydrogen fluoride as adsorbates. We found that the studied embedding method works better for neon compared to hydrogen fluoride, which may be explained by the use of a two-body dispersion correction.

Keywords: embedding adsorption tight-binding ab initio methods

Contents

1. Introduction

Computational modelling of large molecular structures and solids has seen rapid development in recent years. Various properties of these systems can now be described with accuracy that is well sufficient to understand experimental observations. An example is joint experimental and modelling research of the structure and dynamics of molecules adsorbed on solid surfaces [1]. To reach this goal, however, a quantum-mechanical description ("from first principles") is necessary. Unfortunately, the Schrödinger equation cannot be solved directly and exactly for large systems and approximations have to be made to obtain practical approaches. A popular method of choice, Kohn-Sham density functional theory (DFT) is exact in principle, but its widely used approximations often lack predictive power when it comes to systems where weak interactions, such as van der Waals forces, are important, or systems showing effects of both strong chemical and weak physical forces. These are exactly the effects important for the correct description of adsorption phenomena. As a consequence, accurate prediction of the binding energy between a molecule and a surface remains a challenge. For example, some molecules have two possible adsorption configurations, a chemisorbed state where the molecule is bonded in a chemical sense to the surface and a physisorbed state, where it interacts with the surface via van der Waals interactions. Many theoretical methods in practical use nowadays have problems with predicting the stability of either configurations.

To obtain accurate adsorption energies is far from straightforward as the methods with sufficient accuracy are too computationally expensive to be applied to the systems of interest. There are two main techniques, wave-function and electron-density based methods that originate from quantum chemistry and solid-state physics, respectively. High-level quantum chemical methods are only applicable to small systems due to steep computational scaling, e.g., the coupled cluster method with singles, doubles, and perturbative triples contributions (CCSD(T)) scales as $O(N^7)$ with N being the number of basis functions, which depends on the number of electrons in the system. Therefore, adsorption at surfaces has been studied so far mainly using cheaper DFT methods. In the next few paragraphs, let us explain shortly why the many-electron problem is so difficult to solve and what approximations are typically employed.

1.1 Many-electron problem

The interactions between solids and molecules can be described by the Schrödinger equation. Usually we seek stationary states given by the time-independent version of Schrödinger equation $\hat{H}\,|\psi_n\rangle = E_n\,|\psi_n\rangle$, where $\hat{H}$ is the electronic Hamiltonian. The stationary eigenstates $|\psi_n\rangle$ depend on positions of electrons of the system explicitly and on positions of nuclei parametrically. Nuclei are treated as a static background that causes an effective potential for the electrons, i.e., nuclei are "fixed" – this is the adiabatic (Born-Oppenheimer) approximation.

However, straightforward solution of the many-body Schrödinger equation is difficult due to the dimensionality of the problem: a many-body wavefunction, being a complex-valued function of $3N$ variables for N electrons in three

dimensions, does not factorize because of the electron–electron interaction. Inevitably, due to the complexity of the many-electron problem, arising from the instantaneous electron-electron interaction together with the indistinguishability of electrons as fermions, approximations have to be applied to simplify the problem. If we neglect the electronic Coulomb interaction completely, we speak of the independent-electron approximation, and the wavefunction factorizes. To account for the fermionic nature of electrons, we write the many-body wavefunction as a Slater determinant.[1] Perhaps the most popular approximation so far is the mean-field theory, which replaces the electron interaction with its average effects. This averaging means that there is a common potential for all the electrons. The most widely used mean-field schemes are the Hartree-Fock approach and density functional theory. A mean-field solution usually provides about 99% of the total energy, and, if one does not look at the fine details, most of the electron density. If the mean-field theory is qualitatively correct, quantitative accuracy can be achieved by introducing perturbative corrections. The corrections reintroduce the explicit interactions between electrons and it turns out that they affect the most the electrons around the Fermi surface. Methods such as the *GW* approximation [2] for calculation of electronic quasi-particle energies, random phase approximation (RPA) [3], and many-body perturbation theory [4] and coupled clusters (CC) [5] from quantum chemistry, are examples of improving on top of the mean-field theory. An alternative set of schemes to obtain total energy are quantum Monte Carlo methods [6]. But even the simplest of them, variational Monte Carlo, requires a guess of the wavefunction from a mean-field approach.

Recent progress in quantum computing, especially the algorithm development and experimental realizations of quantum simulation, seems to provide an alternative path to overcome the fundamental exponential barrier. However, despite the decades-long efforts of scientists and engineers there is still much work to be done [7].

The principle of locality[2] allows ignoring some long-range interactions in calculations, and has been applied to reduce the computational cost of many mean-field based methods (such as the linear-scaling density functional theory [8], local correlation techniques [9] and many-body expansion), as well as develop non-perturbative electronic structure methods that do not rely on the mean-field theory (such as density matrix renormalization group (DMRG) and other tensor network methods [10]). Lastly, locality puts forward the idea of embedding, one of central topics of this thesis.

1.2 Embedding

The problem of interest is the adsorption of a single molecule on a solid surface. One way to approach this is to take a small cluster representing the surface. The size of the cluster is then gradually increased until convergence of properties

[1] In the independent-electron approximation, only one determinant is needed. One can work with wavefunction methods that scale as M^3, with M being the size of the basis, or better, as opposed to the exponential scaling of the interacting many-body problem.

[2] Although quantum mechanics itself allows entanglement between quantum objects infinitely far apart, the interactions between electrons decay with distance, and thus for low energy states the correlation functions eventually vanish at long distance.

in question is observed. However, increasing the cluster size typically leads to a drastically increased computer cost and the convergence of properties can be slow as the effects of the environment are neglected. Embedding theories provide a natural way to focus computation on a small region of interest within a larger environment. Specifically, the purpose of the embedding is to provide a computational recipe for the properties of a finite cluster (e.g., adsorbate with nearest substrate atoms), taking into account its environment (rest of the substrate), without the computational cost of treating the full problem. For this idea behind quantum mechanics/molecular mechanics (QM/MM) or quantum mechanics/quantum mechanics (QM/QM) methods, the 2013 Nobel Prize in Chemistry was awarded to M. Karplus, M. Levitt, and A. Warshel.

There have been several embedding strategies developed over the years. The two main ones are the subtractive and additive embedding. In both, the region of interest (I) is treated with a more accurate method, giving energy contribution E_I^{acc}. Now in the additive scheme, the total energy is obtained by adding the energy of the environment (II) obtained with a less accurate method E_{II}^{approx} and an interaction term E_{I-II}. On the other hand, in the subtractive scheme, these two terms are substituted by the energy difference $E_{I+II}^{\mathrm{approx}} - E_I^{\mathrm{approx}}$ obtained with the less accurate (cheaper) method. The benefit of this latter approach is that there is no interaction term, the drawback is that the cheaper method must be able to describe the region I at least qualitatively correctly. The subtractive scheme is applied in Chapter 4 of this thesis.

An example of the additive scheme is the so-called electrostatic embedding QM/MM method, applicable, e.g., to ionic solids. Here, the cluster itself is treated quantum mechanically, whereas the environment is treated classically, e.g. as fixed point charges, involving interatomic electrostatic potentials (force fields) that are computationally far cheaper than QM calculations. These methods differ by the extent of mutual polarization included in the force fields [11]. However, in covalent or metallic crystals, as opposed to ionic solids, it is beneficial to go beyond electrostatics and account for electron correlation and the fact that the outermost atoms of the cluster are bonded to the rest of the system.

Further classification of embedding schemes is based on the physical quantity responsible for information transfer through the interface between the two regions, in order to include quantum-mechanical electron correlation effects. This quantity can be either the electron density (as in DFT methods), the single-particle Green's function, or the single-particle density matrix [12].

Several embedding schemes based on density functional theory (DFT) have been proposed, relying on some form of an embedding potential V_{emb} that mediates the interaction between the cluster and the environment. For example, in the approach of Carter and co-workers [13], the atomic cluster is placed in an energy-independent, local embedding potential $V_{\mathrm{emb}}(\boldsymbol{r})$ chosen so that the ground-state DFT electron density is the same as the density of the cluster plus the environment. However, local embedding potentials possess the disadvantage that no set of mutually orthogonal orbitals of the entire system exists. Consequently, evaluation of the total energy becomes challenging: in particular, the kinetic energy needs to be approximated [14]. More elaborate operator-based approaches, such as the one of Manby and co-workers [15] introduce a non-local embedding potential $V_{\mathrm{emb}}(\boldsymbol{r}, \boldsymbol{r'})$, in presence of which the region of interest (cluster) is treated

using a high-level method. Recently, operator-based embedding techniques were extended to bulk systems, treating point defects in semiconductors and insulators [14].

With the aim of modelling strongly correlated molecules and solids, another class of QM/QM embedding methods was developed using mostly time-dependent (dynamic) Green's functions. A popular scheme is the dynamical mean-field theory (DMFT) [16], allowing to study the properties of a large system by simulating a smaller "impurity" system that is coupled to a bath. In DMFT, the full problem of interest (commonly a crystal) is divided into fragments containing strongly correlated orbitals (typically transition metal d and f orbitals) for which a high-level self-energy approximation in each fragment is computed. These fragments are embedded in the rest of the system that is treated with more approximate methods. Most recent developments in the field of quantum embedding theories for correlated systems include the self-energy embedding theory (SEET) of Zgid and co-workers [17]. Note that some theories, also aiming at strongly correlated systems, partition density matrices instead of Green's functions, e.g., density matrix embedding theory (DMET) [18], utilizing the Schmidt decomposition of quantum states.

Green's function approaches using a local energy-independent embedding potential miss a proper treatment of the cluster wave-functions, so that they match the wave-functions in the substrate. There are two general approaches in which the wave-functions are properly embedded, classified by Grimley and Pisani [19] as *perturbed-crystal* and *perturbed-cluster* methods. In perturbed-crystal methods the solution for the perfect solid is modified to account for the presence of the defect, i.e., it is assumed that the defect introduces a perturbation relative to the perfect crystal, localized to the cluster. If the Green's function of the perfect crystal is known in any localized basis representation, and the matrix elements of the perturbation can be constructed, the Green's function of the perturbed crystal can be calculated, for example, using the Dyson equation. In case of perturbed-cluster methods, "the solution for a small region around the defect is modified to account for the rest of the crystal" [20]. In other words, an embedding potential is added to the cluster Hamiltonian, to account for the rest of the system (in a localized orbital basis, the embedding potential is usually called 'self-energy') [21]. Both of these schemes will be further discussed in this thesis.

Finally, it should be noted that the embedding method has a link with R-matrix theory, widely used in electron scattering calculations in atomic physics. The R-matrix is a generalised logarithmic derivative for the scattering electron wave-function, defined over a sphere containing the atomic electrons. It represents a many-body embedding potential, as the external electron can excite the atomic electrons in the process of scattering.

1.3 Low dimensional systems

Real solids usually have "ends" where periodicity is lost, but this is commonly ignored as a surface effect that has no influence on bulk properties. The finite size of actual solids normally leads to no observable effects, but as we scale down the size of structures, the discreteness of energy levels becomes comparable to the thermal energy k_BT leading to experimentally observable effects. This leads

to "size quantization" effects.

Over the last decades, miniaturization in the industry has fuelled theoretical and experimental research into low dimensional electron systems meaning that physical models of one- and two-dimensional electron systems remain of practical and fundamental interest. Fabrication of electronic devices, such as transistors, using these novel materials and incorporating new designs can exploit the quantum mechanical phenomena inherent to these materials. The hope is that a new paradigm could be found circumventing the limitations of the current silicon technology. This is the area where carbon-based nanomaterials like graphene and quasi one-dimensional carbon nanotubes (CNTs) show great promise due to their remarkable electronic properties. The usage of materials as electronic components relies on the control of the electronic band gap, which can be affected by the location and species of chemical dopants.

The understanding of low-dimensional physics was helped experimentally by the development of molecular beam epitaxy (MBE) that allows materials to be grown layer by layer. A combination of layers with different properties led to the production of a layered semiconductor nanostructure, where the electrons in a solid are trapped in a quantum well, forming a a two dimensional layer of high carrier concentration and high mobility, called 2-dimensional electron gas (2DEG). This layer can be further restricted with applied electric field to form a 1D electron waveguide, or even zero-dimensional structure – a quantum dot. When studying electronic conduction through small[3] conductors, various quantum phenomena have been observed, such as quantum Hall effect. The quantum Hall effect was first observed in a 2DEG [22] and led to two Nobel Prizes in Physics, of Klaus von Klitzing in 1985, and of Robert B. Laughlin, Horst L. Störmer and Daniel C. Tsui in 1998.

It was long believed that isolated two-dimensional structures such as a single graphene layer are unstable. Only in 2004, Geim and Novoselov extracted graphene monolayers from bulk graphite using sticky tape for the first time [23], for which they were awarded the 2010 Nobel Prize in Physics. The discovery of graphene and its tremendous impact on scientific research has initiated the search for other elemental two-dimensional (2D) honeycomb materials: in 2012, silicene was first synthesized under ultrahigh vacuum conditions on a silver(111) single crystal by Si molecular beam epitaxy (MBE) [24]. The synthesis of silicene further launched an intensive search for other 2D elemental materials synthesized under ultrahigh vacuum by MBE-like methods. The synthesis of germanene (2D germanium) was reported in 2014 [25] followed by the synthesis of stanene (2D tin) in 2015 [26].

However, note that of these 2D materials, only graphene is fully flat, which results from the pure sp^2 hybridization of its constituent carbon atoms. Other group IV elements energetically prefer hybridization with an additional sp^3 character when forming a 2D honeycomb layer. As a consequence of this mixed hybridization, the bonds between adjacent atoms of the lattice are buckled, resulting in a layer that is not completely flat. This buckling facilitates control of the 2D layer properties, for example, via chemical functionalization or external

[3]A system is considered small, if quantum effects become necessary for its description. This happens when its size becomes comparable to three characteristics lengths: the electron wavelength, the electron mean free path and the phase coherence length.

fields [27]. Another advantage of these new materials is the significant spin–orbit interaction, which increases with increasing atomic size of the involved elements. This opens the way to observe a quantum spin Hall effect [28], for example, in germanene or stanene in an accessible temperature range, possibly even at room temperature.

Interestingly, many other two-dimensional crystals have been fabricated. Two dimensional hexagonal boron nitride (2D-hBN) is an isomorph of graphene with a very similar layered structure. Although it is by itself an insulator, it can well be tuned by several strategies including doping, substitution, functionalization and hybridization [29]. 2D-hBN is considered as one of the most promising materials that can be integrated with other 2D materials, such as graphene and transition metal dichalcogenides, e.g., MoS_2, for the next generation microelectronic and other technologies.

1.4 Motivation and aims of this work

It is of utmost interest to understand the role of impurities in periodic structures modelling real solids. To this end, several one- and two-dimensional models are studied in this work with the aim of elucidating the response of electron systems to an adsorbed impurity, i.e., localized perturbation. It is assumed that the studied effects are local in the sense that the impurity (adsorbate) perturbs the system in some limited region, whose size, however, is not known a priori. In order to study the extent of this perturbed region and understand resulting electronic structure effects, various theoretical approaches and models can be employed. In particular, to study theoretically the local density of states and adsorption energies, which are properties of interest obtainable from experiments, formalism of Green's functions is appropriate. Indeed, Green's functions are widely used in many areas of physics to study, e.g., electron propagation in a system.

This thesis is organized as follows: in Chapter 2, single-particle, time-independent, zero-temperature Green's functions of tight-binding Hamiltonians are studied. First, we explain the motivation behind addressing the electronic structure problem with the Green's functions instead of traditional wave functions. Then, Green's function formalism for studying impurities is discussed.

In Chapter 3, one- and two-dimensional systems are studied using Green's functions. Namely, the local density of states on the impurity (adatom) and adsorption energies are calculated. To this end, we employ the tight-binding approximation, which is, in fact, the simplest possible model of a solid with the usual characteristic features such as energy band gaps [30]. It is a widely used scheme within independent-electron approximation. The *perturbed-crystal* embedding method and the Dyson equation are applied. Subsequently, we make use of the *perturbed-cluster* embedding method in LCAO formalism that restricts the calculation to a limited region of space and introduces the effect of the semi-infinite solid through a non-local energy dependent term in the Hamiltonian.

In Chapter 4, state-of-the-art ab initio methods are employed to study adsorption energies and convergence of the subtractive embedding scheme. Polyacetylene molecules of various lengths are considered as quasi-1D models. The effect of chain length on the interaction of the chain with an "adsorbate" is studied. Also, convergence of adsorption energies of small closed-shell systems on

two-dimensional graphene and hBN structures is studied. Due to the computational complexity of ab initio methods, we rely on the subtractive embedding method, applying the computationally demanding scheme only for the area (cluster) around the adsorption site and using a simpler approach for the rest of the system (environment). Here, simpler methods include Hartree-Fock, EXX, PBE functional within DFT and DFT-D3 dispersion correction. Higher-level methods include MP2 and RPA.

2. Formalism

To simulate many-electron problems, the precise form of a wavefunction is not always needed. Very early after the development of quantum mechanics, it was clear that the problem of dimensionality is very difficult to overcome and alternate methods to compute measurable properties of electronic systems without precise knowledge of the many-body wavefunctions must be developed. In this chapter one of these methods is discussed, namely, single-electron time-independent Green's functions. These are introduced along with the concepts of the linear combination of atomic orbitals (LCAO), the (local) density of states (DOS) and other quantities relevant for studying electronic states in materials.

2.1 LCAO approach and the tight-binding approximation

In periodic crystals, one-electron wavefunctions take the form of Bloch states, exploiting the discrete translational invariance of the system. In particular, if the system is described by a periodic mean-field Hamiltonian, i.e., Hamiltonian invariant under a translation by any lattice vector, the stationary states are the Bloch [31] states of the form $\psi_{n\boldsymbol{k}}(\boldsymbol{r}) = e^{i\boldsymbol{k}\cdot\boldsymbol{r}}u_{n\boldsymbol{k}}(\boldsymbol{r})$, where the function $u_{n\boldsymbol{k}}(\boldsymbol{r})$ has the same periodicity in $\boldsymbol{r}$ as the lattice potential. The quantum number $\boldsymbol{k}$ determines how much the phase changes when we propagate by a lattice vector $\boldsymbol{R}$, i.e., $\psi_{n\boldsymbol{k}}(\boldsymbol{r}+\boldsymbol{R}) = e^{i\boldsymbol{k}\cdot\boldsymbol{R}}\psi_{n\boldsymbol{k}}(\boldsymbol{r})$. Here, n indexes different single-electron states.

In practical calculations the functions $u_{n\boldsymbol{k}}(\boldsymbol{r})$ need to be represented, either on a grid or using some basis functions. For solids, plane waves seem to be the natural basis, since the expansion of the electronic wave functions in plane waves is computationally very efficient. This is true because the plane waves are eigenfunctions of the momentum operator and the kinetic energy operator is diagonal in momentum (reciprocal, or $\boldsymbol{k}$) space. Hence the kinetic energy can be easily computed in momentum space whereas the potential energy is more easily evaluated in real space. The switching between real and momentum space is done by Fast-Fourier-Transformation (FFT) techniques. However, in order to use plane waves for description of impurities and surface science problems, the surface has to be cast into a three-dimensional periodicity. This is achieved in the so-called supercell approach, in which a slab of finite width, containing the interface, is considered and periodic boundary conditions are applied. Clearly, the electronic structure of the surfaces of the slab is altered by quantum confinement along the normal of the surface and the vacuum layer between the slabs has to be sufficiently thick to avoid any interaction between the slab and its periodic images. This means that the accuracy of the slab approach to modeling a semi-infinite surface may critically depend on several parameters such as the slab and vacuum layer thickness. For example, convergence of adsorption energies can be slow with the number of bulk layers considered [32].

In order to model local phenomena, it is more useful to employ a localized basis set, e.g. the LCAO method (linear combination of atomic orbitals) by

writing the wavefunction as a sum of localized atomic orbital basis functions

$$\psi_n(\boldsymbol{r}) = \sum_{\alpha,\boldsymbol{r_j}} c_{n,\alpha\boldsymbol{r_j}} \phi_\alpha(\boldsymbol{r} - \boldsymbol{r_j}), \tag{2.1}$$

with $\phi_\alpha(\boldsymbol{r} - \boldsymbol{r_j})$ being atomic-like orbitals[1]. Here, j is a site index numbering atomic sites and α indicates the type of orbital, e.g., 3s, $3p_z$, etc. In the following, we will restrict ourselves to the case of a single orbital per atom, i.e., we neglect α.

The LCAO expansion can be applied to the single-particle Schrödinger equation to give the matrix equation

$$Hc_{n,j} = SE_n c_{n,j}, \tag{2.2}$$

with H and S being the Hamiltonian and overlap matrices, respectively, and $c_{n,j}$ column vectors with index j accounting for both $\boldsymbol{r_j}$ and α. The calculation of the Hamiltonian matrix elements involves at least one- and two-center integrals. The tight-binding method consists of parametrizing these integrals with orbital energies ϵ and (off-diagonal) hopping terms τ. The discussion of these parameters is postponed to the next chapter. Note that tight-binding is very similar to the Hückel method used in quantum chemistry. In solid-state theory, the LCAO tight-binding method is particularly appropriate when the overlap between neighboring atoms is relatively small, e.g., for describing the p bands of alkali halides and d bands of transition metals [33].

In general, orbitals on different sites are not mutually orthogonal, that is, $\langle\phi_i|\phi_j\rangle = S_{ij} \neq 0$, although we assume the orbitals to be normalized to 1. If S is orthogonal, calculations are simpler, if not, Löwdin orthogonalization is applied by transforming orbitals with the matrix $S^{-1/2}$, leading to $\tilde{H} = S^{-1/2}HS^{1/2}$ with the same eigenvalues as H. Note, however, that each of the new orbitals is now more spread out, thereby increasing the number of non-zero matrix elements in $\tilde{H}$.

As we apply the LCAO expansion to solids, we restrict ourselves to the simplest possible case by considering only one atom per primitive crystal cell and only one atomic orbital per atom. In this case, due to the Bloch theorem,[2] the coefficients $c_{\boldsymbol{r_j}}$ are equal to $\frac{1}{\sqrt{N}}\exp(i\boldsymbol{k}\cdot\boldsymbol{r_j})$ with $\boldsymbol{r_j}$ being atom positions and N number of unit cells in the solid. This was originally proposed by Bloch in 1928 [31] and further developed by Slater and Koster [34]. The quantum number $\boldsymbol{k}$ is restricted to a finite region in $\boldsymbol{k}$-space, called the first Brillouin zone (BZ). The eigenenergies $E_n(\boldsymbol{k})$ are continuous functions of $\boldsymbol{k}$ within each band n.

Bloch states are extremely useful as they allow to reduce the size of the simulation cell to the unit cell only. Moreover, the overlap and Hamiltonian matrices factorize in $\boldsymbol{k}$ allowing for reduced computational cost. However, Bloch states are delocalized across the whole system, and therefore they are unsuitable for description of local phenomena such as defects or adsorption. For example, at a surface, new electronic states arise, exhibiting very limited propagation into the

[1] These are functions of 3-dimensional vector $\boldsymbol{r}$ and they can be given numerically or analytically, but typically decaying exponentially as $e^{-\zeta r}$ for r radial distance measured from the center of the given orbital.

[2] It is easy to see that the Bloch condition $\psi_n(\boldsymbol{r}+\boldsymbol{R}) = e^{i\boldsymbol{k}\cdot\boldsymbol{R}}\psi_n(\boldsymbol{r})$ leads to $c_{\boldsymbol{r_j}+\boldsymbol{R}} = e^{i\boldsymbol{k}\cdot\boldsymbol{R}}c_{\boldsymbol{r_j}}$, or, equivalently, $c_{\boldsymbol{r_j}} = e^{i\boldsymbol{k}\cdot\boldsymbol{r_j}}c_0$, and we can choose $c_0 = 1/\sqrt{N}$ to satisfy orthonormality.

bulk. To study effects of impurities, therefore, real space description is preferred. Hence, in the following sections, we will explore the real space representations of relevant physical quantities, such as Green's functions.

2.2 Density of states

There are many properties of interest that can be calculated and at the same time compared to experiments. For example, the density of states (DOS) is accessible from photoelectron spectroscopy (PES). However, it should be noted that PES is hard to be reproduced due to the difficulty in obtaining the DOS of correlated electrons (quasi-particles). In simple one-electron methods, once we know the eigenvalues E_n and eigenfunctions ψ_n of the Hamiltonian $\hat{H}$, we can evaluate the local density of states (LDOS) in the following way:

$$n(E, \boldsymbol{r}) = \sum_n |\psi_n(\boldsymbol{r})|^2 \delta(E - E_n). \tag{2.3}$$

Using the LCAO expansion coefficients $c_{n,j}$ we can rewrite the definition above as

$$n_j(E) = \sum_n |c_{n,j}|^2 \delta(E - E_n), \tag{2.4}$$

which measures the probability of finding an electron with energy E at j-th atom.

The global density of states (DOS) can be calculated as a sum of local densities and tells how many states are in a given energy interval at E

$$n(E) = \sum_j n_j(E) = \sum_n \delta(E - E_n), \tag{2.5}$$

since we assume the wavefunction to be normalized.

For large systems, the density of states does not depend much on the boundary conditions. In general, the local density of states depends on the boundary conditions only a few electron wavelengths away from the boundaries. The comparison of the LDOS in the neighbourhood of a surface (or any defect) with the perfect bulk density of states enables us to study the range of the perturbation due to the surface. In any case, the effects of boundary conditions tend to cancel when one integrates $n(E, \boldsymbol{r})$ (or $n_j(E)$) with respect to E. At the same time, even though a small perturbation may change individual ψ_n by a large amount, it can often leave the sum $\sum_n |c_{n,j}|^2$ invariant. Thus the LDOS does not have such extreme sensitivity to small perturbations that wavefunctions have [33].

If we had to evaluate the LDOS from the $|\psi_n(r)|^2$, or $|c_{n,j}(r)|^2$ respectively, then nothing would have been gained because we would first have had to calculate the eigenstates ψ_n and eigenvalues E_n. The states ψ_n are very sensitive to perturbations, therefore it is more feasible to work with DOS, and Green's functions. In fact, $n(E, \boldsymbol{r})$ can be obtained even without the knowledge of ψ_n, since it is related to the imaginary part of the Green's function $g(\boldsymbol{r}, \boldsymbol{r'}, E)$ by the equation:

$$n(E, \boldsymbol{r}) = -\frac{1}{\pi} \operatorname{Im} g(\boldsymbol{r}, \boldsymbol{r}, E), \tag{2.6}$$

and the Green's function has many marvellous mathematical properties so that it can be solved for directly without ever involving oneself with the wavefunctions $\psi_n(\boldsymbol{r})$. This is the standard way done nowadays when quasi-particle states are obtained within the GW approximation for the self-energy [35].

2.3 Green's functions

Green's functions are used to find solutions to differential equations and are encountered in many parts of physics. Green's functions represent the impulse response of a system to a singular input, and specifically in condensed matter physics, they are used as an efficient method to investigate the behaviour of many-body systems. They contain a lot of information about a system, for example the density of states and transport properties representing the propagation of an electron through the system.

In general, a Green's function $g(\boldsymbol{r}, \boldsymbol{r'}; z)$ for a time-independent, hermitian, linear differential operator $L(\boldsymbol{r})$ with a complete set of eigenfunctions $\phi_n(\boldsymbol{r})$ is defined as the solution to an inhomogeneous differential equation

$$[z - L(\boldsymbol{r})]g(\boldsymbol{r}, \boldsymbol{r'}; z) = \delta(\boldsymbol{r} - \boldsymbol{r'}), \tag{2.7}$$

where vectors $\boldsymbol{r}, \boldsymbol{r'}$ belong to domain Ω and boundary conditions for $\boldsymbol{r}, \boldsymbol{r'}$ lying on the surface S must be the same for $g(\boldsymbol{r}, \boldsymbol{r'}; z)$ as well as $\phi_n(\boldsymbol{r})$.

Introducing a Hilbert space, and using the Dirac bra-ket notation as

$$\phi_n(\boldsymbol{r}) = \langle \boldsymbol{r} | \phi_n \rangle \tag{2.8}$$
$$\delta(\boldsymbol{r} - \boldsymbol{r'}) = \langle \boldsymbol{r} | \boldsymbol{r'} \rangle \tag{2.9}$$
$$\delta(\boldsymbol{r} - \boldsymbol{r'})L(\boldsymbol{r}) = \langle \boldsymbol{r} | L | \boldsymbol{r'} \rangle \tag{2.10}$$
$$g(\boldsymbol{r}, \boldsymbol{r'}; z) = \langle \boldsymbol{r} | g(z) | \boldsymbol{r'} \rangle , \tag{2.11}$$

we can rewrite Eq. 2.7 in the following way:

$$(z - L)g(z) = 1. \tag{2.12}$$

If the complex variable $z = \lambda + i\eta$ does not coincide with λ_n, i.e., if $z \neq \lambda_n$, then we can write formally

$$g(z) = \frac{1}{z - L}. \tag{2.13}$$

Then multiplying with the unitary operator $\sum_n |\phi_n\rangle \langle \phi_n|$ we obtain

$$g(z) = \sum_n \frac{|\phi_n\rangle \langle \phi_n|}{z - \lambda_n}, \; z \neq \lambda_n. \tag{2.14}$$

In this representation of $g(z)$ we can note that it is meromorphic with a finite number of poles, which correspond to the discrete eigenvalues of L. If we want to define $g(z)$ at $z = \lambda_n$, we have to do it by a limiting procedure. In the usual case, where the eigenstates associated with the continuous spectrum are propagating or extended, the side limits $\lim_{\eta \to 0+} g(\lambda \pm i\eta)$ exist[3] but are different from each other [36]. Thus, this type of continuous spectrum produces a branch cut in $g(z)$ along certain parts of the real axis.

[3]For unusual spectra associated with localized eigenstates in disordered systems there is the possibility of the non-existing side limits, but this is not of interest here. The line of singularity corresponding to such a spectrum is not a branch cut but what is called a natural boundary [36].

For the Hamiltonian operator $L = H$ with a complete set of eigenvectors $\phi_n = \psi_n$ with eigenvalues E_n, Eq. 2.14 gives the eigenvalue representation

$$\hat{g}(z) = \sum_n \frac{|\psi_n\rangle \langle\psi_n|}{z - E_n}, \tag{2.15}$$

Here, the choice of the sign of $\pm i\eta$ in the imaginary part of the argument of $g(z)$ determines the causality and the direction of electron propagation. The resulting functions are called the retarded and advanced Green functions respectively and correspond to perturbations acting forward (causal) or backwards in time. The retarded Green functions are chosen here, in accordance with convention when time-reversal symmetry exists for a problem – their use reflects the natural intuition.

In the basis of atomic orbitals ϕ_i, the matrix element of $\hat{g}(z)$ from Eq. 2.15 is given by

$$\hat{g}_{j,l}(z) = \sum_n \frac{\langle\phi_j|\psi_n\rangle \langle\psi_n|\phi_l\rangle}{z - E_n}. \tag{2.16}$$

Now we recall from the discussion above that the eigenstates of a periodic (tight-binding) Hamiltonian have the form

$$|\psi_{n\boldsymbol{k}}\rangle = \frac{1}{\sqrt{N}} \sum_{\boldsymbol{r_j}} e^{i\boldsymbol{k}\cdot\boldsymbol{r_j}} |\phi_j\rangle , \tag{2.17}$$

considering only one atom per primitive crystal cell and only one atomic orbital per atom. Thanks to the orthogonality of the atomic orbitals we obtain

$$\hat{g}_{j,l}(z) = \frac{1}{N} \sum_{\boldsymbol{k}} \frac{e^{i\boldsymbol{k}(\boldsymbol{r_j} - \boldsymbol{r_l})}}{z - E(k)}. \tag{2.18}$$

The most important feature of Green's functions, for us, is that the imaginary part of the onsite[4] Green's function g_{jj} gives the local density of states (LDOS):

$$n_j(E) = -\frac{1}{\pi} \operatorname{Im} g_{jj}(E), \tag{2.19}$$

where j is any site index. This fact was already mentioned in Eq. 2.6, however now we can understand where it comes from. First, note that the (retarded) Green's function of the Hamiltonian operator can be written using Eq. 2.15 formally as

$$\hat{g}(E) = \lim_{\eta \to 0+} ((E + i\eta) - \hat{H})^{-1}. \tag{2.20}$$

Using the well-known identity

$$\lim_{\eta \to 0+} \frac{1}{x \pm i\eta} = \text{p.v.}\frac{1}{x} \mp i\pi\delta(x), \tag{2.21}$$

one can easily obtain Eq. 2.19. Also, it follows that the global density of states (DOS) (Eq. 2.5) is the trace of imaginary part of Green's function, i.e., it is given by a sum over all atomic orbitals

$$n(E) = -\frac{1}{\pi} \operatorname{Im} \operatorname{Tr} g_{jj}(E). \tag{2.22}$$

[4]This is the diagonal element in the matrix representation.

While the form of g in Eq. 2.20 readily allows calculation via matrix inversion for small systems (taking $z = E + i\eta$, η small), for large systems, this method becomes impractical[5]. Alternatively, if we are interested in only a few elements of the matrix g, such as the diagonal ones giving the local density of states, we can apply methods of linear algebra to obtain these elements without the need to invert the whole matrix, as we will show later in this thesis.

Assuming an infinite periodic system, we can replace the sum with an integral in Eq. 2.15 by considering a finite domain Ω and taking the limit as Ω becomes infinite

$$\sum_{\boldsymbol{k}} \xrightarrow[\Omega\to\infty]{} \Omega \int \frac{d\boldsymbol{k}}{(2\pi)^d}. \tag{2.23}$$

Then we can rewrite Eq. 2.16 as

$$\hat{g}_{j,l}(z, \boldsymbol{r}) = \frac{\Omega}{N} \int_{BZ} \frac{d\boldsymbol{k}}{(2\pi)^d} \frac{e^{i\boldsymbol{k}(\boldsymbol{r_j}-\boldsymbol{r_l})}}{z - E(k)}, \tag{2.24}$$

i.e., the matrix elements of Green's function are now expressed as a d-dimensional integral over the Brillouin zone.

For infinite systems an exact solution can be found by exploiting the periodicity and homogeneity of the system[6]. While one-dimensional tight-binding systems can be quite easily treated by hand (see Chap. 3), Green's functions for two-dimensional tight-binding lattices can be expressed in terms of the complete elliptic integrals of the first kind. For three-dimensional lattices, one can similarly obtain a product of an algebraic expression and two elliptic integrals of the first kind, with moduli that are algebraic functions of the expansion parameter z [37].

For large systems the Green's function can be calculated recursively by piecewise connection of small regions of the entire system using either the continued fraction technique or the Dyson equation.

2.3.1 Continued Fraction

From the spectral decomposition of the diagonal Green function, Eq. 2.16 above, we see that the residue of each eigenvalue in $g(E)$ is positive. This forces the imaginary part of g to be negative for E in the upper half of the complex plane.

[5] As the $n \times n$ matrix H increases in size the computational complexity of calculating g directly through matrix inversion scales typically as $\mathcal{O}(n^3)$. Theoretically one could achieve $\mathcal{O}(n^{2.37})$ (Coppersmith–Winograd algorithm), but this is not used in practice.

[6] In cases of infinite periodic systems (lattices), we speak of the lattice Green's functions (LGFs) in tight-binding formalism, which are used in many areas of condensed matter physics.

The lattice Green's function $g_{i,j}(z)$ can be written as an inverse power series about $z = \infty$, where the coefficient of the z^{-n-1} term is related to the number of paths of length n from site i to site j. This series is useful for numerically evaluating the Green's function outside the unit disk ($|z| > 1$), and sometimes to evaluate the quantities $g(\pm 1)$, which are known as Watson integrals [37].

To obtain the real-space representation of the Green's function 'on the cut' (i.e., on either side of the branch cut), more sophisticated methods must be employed, since the power series diverges. The recursion method and the continued-fraction method can be used, or, alternatively, recently it was shown (see Ref. [38]) that Green's functions can be evaluated by converting their power series into Chebyshev series. This amounts to analytic continuation from the region $|z| > 1$ to the region $|z| < 1$.

By hermiticity, the imaginary part of $g(E)$ is positive for E in the lower half-plane. Thus the poles of $g(E)$, which occur at eigenvalues of H, are real and the zeros of $g(E)$ are also real and separate the poles along the real E axis. A function with the above properties can be written as a continued fraction [39].

Using methods of linear algebra, we can easily write down a continued fraction expression for a diagonal element of the matrix $g_{00}(E) = \langle 0|(E + i\eta - H)^{-1}|0\rangle$, where H is a tridiagonal symmetric matrix (representing tight-binding Hamiltonian) of the form

$$H = \begin{pmatrix} a_0 & b_1 & 0 & ... & & 0 \\ b_1 & a_1 & b_2 & 0 & ... & \\ 0 & b_2 & a_2 & b_3 & 0 & ... \\ & & & ... & & \\ ... & ... & 0 & ... & ... & b_N \\ 0 & ... & & 0 & b_N & a_N \end{pmatrix}.$$

Let us denote $A_0 = E - H$, and similarly let A_n be a square matrix with the first n rows and columns removed. The first element of the inverse matrix A_0^{-1} is given as the cofactor divided by determinant:

$$g_{00} = \frac{\det A_1}{\det A_0}.$$

We can expand the determinant as

$$\det A_0 = (E - a_0) \det A_1 - b_1^2 \det A_2,$$

leading to

$$g_{00} = \frac{1}{(E - a_0) - b_1^2 \frac{\det A_2}{\det A_1}},$$

therefore, the first diagonal element of the Green function is given by a continued fraction

$$g_{00}(E) = \cfrac{1}{E - a_0 - \cfrac{b_1^2}{E - a_1 - \cfrac{b_2^2}{E - a_2 - ...}}}. \tag{2.25}$$

This is the continued-fraction representation and it can be used to compute the local density of states by, in the finite case, introducing a small imaginary part to E (the effect is to broaden each delta function into a Lorentzian), or in the infinite case, replacing an infinite part of the fraction by an analytic approximation. This continued fraction truncated to level N can be written as a sum of rational functions and then the LDOS is given as a sum of delta functions. There are several ways to turn this into a smooth continuous function [39].

Since any matrix can be transformed into a tridiagonal matrix[7], any tight-binding model can be transformed into this pseudo-one-dimensional chain model [39]. Since any quantum system can be transformed into a chain model, we need only investigate such chain models in order to see the varieties of quantum phenomena that are possible. To understand a particular physical system, we only need to find a suitable chain model.

[7]The fact that any square matrix can be tridiagonalized follows from the theorem on the Jordan canonical form: any matrix with eigenvalues λ_i is similar to a matrix with these eigenvalues in the principal diagonal, with zeros and one along the first superdiagonal, and zeros elsewhere.

2.3.2 Dyson equation

In some cases we know the Green's function of a subsystem and we want to use it to find the full system's Green's function. This partitioning can occur not only in spatial sense, as in the treatment of defects, but also in a Hilbert space, as in the perturbation theory.

In later chapters, we will aim to model localized disorder in periodic systems. The Dyson equation is a useful way of formalizing the treatment of a localised perturbation applied to a regular crystal lattice. Writing the Hamiltonian of the perturbed system as $\hat{H} = \hat{H}_0 + \hat{V}$, we denote the Green's function of the unperturbed Hamiltonian as $\hat{g} = \frac{1}{z-\hat{H}_0}$ and similarly let $\hat{G}$ be a Green's function of $\hat{H}$. Then we can rewrite Eq. 2.20 as

$$\begin{aligned}
\hat{G}(z) &= (z - \hat{H})^{-1} \\
&= \left[(z - \hat{H}_0) \left(1 - \frac{1}{z - \hat{H}_0} \hat{V} \right) \right]^{-1} \\
&= \hat{g} \left[1 - \hat{g}\hat{V} \right]^{-1} \\
&= \hat{g} \left[1 + \hat{g}\hat{V} + (gV)^2 + ... \right] \\
&= \hat{g} + \hat{g}\hat{V}\hat{G}.
\end{aligned}$$

It is useful to define

$$\hat{T} = \frac{\hat{V}}{1 - \hat{g}\hat{V}}, \tag{2.26}$$

so that we can also write for the full Green's function

$$\hat{G} = \hat{g} + \hat{g}\hat{T}\hat{g} \Longrightarrow \Delta\hat{G} = \hat{g}\hat{T}\hat{g}. \tag{2.27}$$

The quantity $\hat{T}$ represents the (renormalized) perturbation modified by the effect of perturbation itself. If $\hat{V}$ is Coulomb interaction, $\hat{T}$ would be the screened interaction, usually denoted $\hat{W}$.

Let us now consider the construction of the inverse operator $1/(1 - gV)$ for potentials V of finite range in a specific matrix representation. From linear algebra, we know that the inverse of a matrix A is equal to the transpose of the cofactor matrix times the reciprocal of the determinant of A. A necessary and sufficient condition for the existence of an inverse is that the determinant must be non-zero. The determinant will vanish only for some specific values of the energy, which are the energies of the localized states. Consequently, in order to find the energy of a localized state, we look for a root of $\det(1 - gV)$.

We arrange the matrix V (corresponding to a finite-range potential) in block form, so that the portion of V containing nonzero elements forms a submatrix in the upper left. Then, g is arranged in a corresponding manner. Namely, we denote

$$V = \begin{pmatrix} V_{aa} & 0 \\ 0 & 0 \end{pmatrix}, \; g = \begin{pmatrix} g_{aa} & g_{ab} \\ g_{ba} & g_{bb} \end{pmatrix}. \tag{2.28}$$

Then we obtain

$$1 - gV = \begin{pmatrix} 1 - g_{aa}V_{aa} & 0 \\ -g_{ba}V_{aa} & 1 \end{pmatrix}, \tag{2.29}$$

where 1 represents a unit matrix.

By expanding according to minors, beginning at the lower right, we can easily verify that the determinant of the entire matrix is just the determinant of the upper-left part,

$$\det(1 - gV) = \det(1 - g_{aa}V_{aa}). \tag{2.30}$$

For example, if we have a single impurity with only a single nonzero matrix element V_{aa} of the impurity potential, we can immediately write that the energy of a localized (bound) state E_b is given implicitly by:

$$\operatorname{Re} g_{aa}(E_b) = \frac{1}{V_{aa}}. \tag{2.31}$$

Further, if we construct the inverse of the upper left matrix $1 - g_{aa}V_{aa}$, the inverse of the full matrix can be found immediately:[8]

$$(1 - gV)^{-1} = \begin{pmatrix} (1 - g_{aa}V_{aa})^{-1} & 0 \\ g_{ba}V_{aa}(1 - g_{aa}V_{aa})^{-1} & 1 \end{pmatrix}. \tag{2.32}$$

To construct T, we multiply this by V to get:

$$T = \begin{pmatrix} V_{aa}(1 - g_{aa}V_{aa})^{-1} & 0 \\ 0 & 0 \end{pmatrix}, \tag{2.33}$$

i.e., the nonzero part of T has the same dimensionality as the nonzero block of the potential.

2.3.3 Change in the density of states due to a perturbation

Let us now consider the local density of states $n_j(E)$, which is given by the imaginary part of the onsite Green's function, as shown in Eq. 2.19. By integrating $n_j(E)$ up to the maximally occupied level E_F, we obtain the electron occupation[9] of the j-th lattice orbital denoted as N_j:

$$N_j = -\frac{1}{\pi} \operatorname{Im} \int_{-\infty}^{E_F} g_{jj}(E) dE, \tag{2.34}$$

where the zero-temperature limit of the Fermi-Dirac distribution $f_{\mathrm{FD}}(E) \xrightarrow[T \to 0]{} \Theta(E_F - E)$ is assumed.

[8] Namely, we utilize the fact that, given a matrix partitioned in the block form

$$\begin{pmatrix} A & 0 \\ C & 1 \end{pmatrix},$$

its inverse is given by

$$\begin{pmatrix} A^{-1} & 0 \\ -CA^{-1} & 1 \end{pmatrix}.$$

[9] This quantity corresponds to the electronic charge density $\rho(\boldsymbol{r})$ in density functional theory calculations.

For example, let us consider an isolated electron occupying an orbital with an arbitrarily chosen energy level ϵ_a. The corresponding Green's function is according to Eq. 2.15 given by

$$g_{aa}(E) = \lim_{\eta \to 0+} \frac{1}{E + i\eta - \epsilon_a}. \tag{2.35}$$

Then from Eq. 2.34 we obtain for the occupancy of the level

$$N_a = -\frac{1}{\pi} \operatorname{Im} \int_{-\infty}^{E_F} g_{aa}(E) dE = \frac{\eta}{\pi} \int_{-\infty}^{E_F} \frac{1}{(E-\epsilon_a)^2 + \eta^2} dE = \frac{\pi + 2 \arctan\left(\frac{E_F - \epsilon_a}{\eta}\right)}{2\pi}. \tag{2.36}$$

Clearly, since $\eta > 0$, the result is $N_a = 1$ if $E_F > \epsilon_a$, i.e., the level is occupied, or $N_a = 0$ if $E_F < \epsilon_a$, i.e., the level is not occupied.

Here it may be useful to note that in this chapter the existence of spin degeneracy is ignored, since it has been assumed that only one electron can occupy one energy level.

In general, to calculate the change in the density of states of a perturbed Hamiltonian $H = H_0 + V$, where H and H_0 have eigenvalues E_j and ϵ_j respectively, one can write, as in [40], with the help of Eq. 2.21, that[10]

$$\begin{aligned} \Delta n(E) &= \sum_j (\delta(E - E_j) - \delta(E - \epsilon_j)) = \\ &= -\frac{1}{\pi} \operatorname{Im} \sum_j \left(\frac{1}{E - E_j + i\eta} - \frac{1}{E - \epsilon_j + i\eta} \right) = \\ &= -\frac{1}{\pi} \operatorname{Im} \frac{\partial}{\partial E} \log\det \left(\frac{E - H + i\eta}{E - H_0 + i\eta} \right) = \\ &= -\frac{1}{\pi} \operatorname{Im} \frac{\partial}{\partial E} \log\det(1 - gV). \end{aligned} \tag{2.38}$$

In a similar way, see, e.g., discussion in [40], we can derive for the density of states

$$n(E) = -\pi^{-1} \operatorname{Im} \frac{d}{dE} \log\det g(E + i\eta), \tag{2.39}$$

while for the integrated desity of states (number of electrons with energy below E):

$$N(E) = -\pi^{-1} \operatorname{Im}[\log\det g(E + i\eta)]_{-\infty}^{E}. \tag{2.40}$$

Since $\operatorname{Im} \log z = \arg z$, the above equation for the number of electrons in the system may be interpreted as follows. Near an energy eigenvalue, $g(E)$ is dominated by the pole at the eigenvalue, and the argument (phase) of $g(E + i\eta)$ changes by π as one goes halfway around the pole along a path just above the real axis. Therefore, a single pole contributes with 1.

[10] Here, we choose the principal branch of the complex logarithm. Also, determinants are invariant under change of basis and it is most convenient to use the orthonormal bases of eigenvectors so that

$$\det\left(\frac{E - H + i\eta}{E - H_0 + i\eta} \right) = \prod_j \frac{E - E_j + i\eta}{E - \epsilon_j + i\eta} \tag{2.37}$$

For any finite cluster of atoms, the energy levels form a discrete spectrum of eigenvalues E_n instead of a continuous band, and local DOS is given by a corresponding set of delta functions and is, strictly speaking, either zero or infinite, and it can easily change from one to the other if, by enlarging the cluster and changing the E we move onto or off one of the delta functions. In that mathematical sense, $n(E)$ does not converge as the size of the cluster is increased. In reality, the number of delta functions increases with the cluster size and the weight of one eigenfunction on a given atom decreases correspondingly. However, $N(E)$, its primitive function, must be convergent, since we require it to represent the total number of electrons in the system [33].

2.3.4 Lloyd equations

The Lloyd equations [41] are a set of equations that express the changes in the total number of electrons (ΔN) and total energy (ΔE) through a local perturbation V applied to the system. From the equations above, and using the fundamental theorem of calculus, we can write:

$$\Delta N(E) = -\frac{1}{\pi} \operatorname{Im} \log \det(1 - gV), \tag{2.41}$$

In the case of adsorption, for example, $\Delta N = 0$ is required because the perturbation acts only to connect the adatom and the host system. This act of connection cannot increase or decrease the number of electrons in the whole system, hence the total change must be zero. This quantity can thus be used as a self-consistent check condition. The total electronic energy change is expressed as

$$\Delta E = E_{\text{after}} - E_{\text{before}}, \tag{2.42}$$

where the total electronic energy of a system is given by

$$E_{\text{total}} = \int_{-\infty}^{E_F} E n(E) dE. \tag{2.43}$$

Problems in calculating ΔE directly in this manner arise as for large or infinite systems the numerical values of E_{after} and E_{before} are very large, but ΔE is typically several orders of magnitude smaller. This presents an obvious challenge for numerical calculation and doing this reliably is extremely difficult.

Obviously, due to linearity of the integral we can write

$$\Delta E = \int_{-\infty}^{E_F} E \Delta n(E) dE, \tag{2.44}$$

where $\Delta n(E)$ is a change of the density of states.

Next, substituting the definition of $\Delta n(E)$ from Eq. 2.38, we obtain an alternative expression for ΔE with only knowledge of the local perturbation V [40]:

$$\Delta E = -\frac{1}{\pi} \operatorname{Im} \int_{-\infty}^{E_F} E \frac{d}{dE} \log \det(1 - gV) dE. \tag{2.45}$$

In this thesis, the adsorption energy is by definition the difference in total electronic energies of the perturbed (with the adsorbate) and unperturbed (bare) systems. The electronic energy of the isolated adsorbate must be equal to $C\epsilon_a$,

where C is the number of electrons occupying the orbital. Since the perturbation V connects the impurity to the host system, it must be required that $\Delta N = 0$. An additional subtlety is that the disconnected impurity has an energy level which may or may not be occupied by electrons, but must be nevertheless considered in the calculations.

Using the result from Eq. 2.45, and integrating by parts, we obtain

$$E_{\text{ads}} = (2\theta(E_F - \epsilon_a) - C)\epsilon_a + \frac{2}{\pi}\,\text{Im}\int_{-\infty}^{E_F} \log\det(1 - g(E)V)dE, \tag{2.46}$$

where the factor 2 accounts for spin degeneracy.

2.4 LCAO Embedding

In the LCAO method, the wave-function for the whole system $\psi(\boldsymbol{r})$ is expanded in terms of local orbitals, which are typically atomic-like wave-functions. The Schrödinger equation becomes the matrix eigenvalue equation.

In the embedding problem, we split the orbitals into those in region I and those in region II. The orbitals in region I have coefficients in the wave-function expansion which we shall represent by the vector ϕ, and those in region II by ψ. The matrix Schrödinger equation for the whole system can then be written in block matrix form as [21]

$$\begin{pmatrix} H_{11} & H_{12} \\ H_{21} & H_{22} \end{pmatrix} \begin{pmatrix} \phi \\ \psi \end{pmatrix} = E \begin{pmatrix} O_{11} & O_{12} \\ O_{21} & O_{22} \end{pmatrix} \begin{pmatrix} \phi \\ \psi \end{pmatrix}. \tag{2.47}$$

The only non-zero elements of H_{12} and O_{12} are those which couple the orbitals across the boundary between the regions. This system of equations for ϕ and ψ can be rewritten using the Green function $g_{22} = (EO_{22} - H_{22})^{-1}$ for region II decoupled from I as

$$H_{\text{emb}}\phi = [H_{11} + \Sigma_{11}(E)]\phi = EO_{11}\phi, \tag{2.48}$$

where the self-energy (embedding) matrix is given by

$$\Sigma_{11}(E) = (H_{12} - EO_{12})g_{22}(H_{21} - EO_{21}). \tag{2.49}$$

The presence of the energy-dependent embedding potential $\Sigma(E)$, also called the self-energy, in Eq. 2.48 prevents the eigenvalues and eigenvectors from being obtained from a single matrix diagonalization. Nevertheless, this formulation is still very useful, and is used, e.g., for calculations of electron transport in LCAO formalism [42].

The embedded Green's function

The Green's function of region I is defined as

$$(EO_{11} - H_{\text{emb}})G_{11}(E) = [EO_{11} - (H_{11} + \Sigma_{11}(E))]G_{11}(E) = I, \tag{2.50}$$

where I is a unit matrix. This equation defines the embedding potential $\Sigma(E)$ and shows that it is calculable from the properties of the unperturbed system alone. Moreover, $\Sigma(E)$ is a boundary-localised potential, in that it is small unless both its row orbital and its column orbitals have substantial overlap with orbitals in the embedding region [43]. Let us finally note that, one can derive this result directly, without invoking the eigenvalue equation, using Dyson's equation of section 2.3.

3. Tight-binding calculations

In this chapter, tight-binding models are studied using the formalism developed in the previous chapter. After a short introduction on tight-binding in position representation, Green's functions for various one- and two-dimensional lattices are computed. Then, a localized impurity (adatom) is introduced and the resulting changes in the electronic structure of the composite systems are studied. The main properties of interest are the adatom density of states (DOS) and the adsorption energy.

3.1 Introduction

In this section, we seek to place the tight-binding approximation on a quantitative footing. To this end, consider a periodic crystal lattice of N unit cells, with a single atom per cell (simple cubic lattice), such that an electron in an isolated atom located at $\boldsymbol{r_j}$ is described by the atomic orbital $\phi(\boldsymbol{r}-\boldsymbol{r_j})$. This atomic orbital is assumed to be the only solution to the equation

$$(-\boldsymbol{\nabla}^2 + U(\boldsymbol{r}))\phi(\boldsymbol{r}) = \varepsilon\phi(\boldsymbol{r}), \tag{3.1}$$

where $U(\boldsymbol{r})$ is the potential energy of an electron moving in the field of an isolated atom.

If we expand the one-electron wave function of the whole crystal as a sum of these orbitals centered on different lattice sites (LCAO expansion), the Bloch theorem requires that the wave function has the form

$$\psi_{\boldsymbol{k}}(\boldsymbol{r}) = \sum_j c_{j\boldsymbol{k}}\phi(\boldsymbol{r}-\boldsymbol{r_j}) = \frac{1}{\sqrt{N}}\sum_j \exp(i\boldsymbol{k}\cdot\boldsymbol{r_j})\phi(\boldsymbol{r}-\boldsymbol{r_j}), \tag{3.2}$$

and satisfies

$$H\psi(\boldsymbol{r}) = (-\boldsymbol{\nabla}^2 + V(\boldsymbol{r}))\psi(\boldsymbol{r}) = E\psi(\boldsymbol{r}), \tag{3.3}$$

where $V(\boldsymbol{r}) \neq \sum_j U(\boldsymbol{r}-\boldsymbol{r_j})$, i.e., the potential is, in general, not equal to the sum of atomic potentials.[1]

Using Eq. 3.2 in 3.3, multiplying from the left by $\phi^*(\boldsymbol{r}-\boldsymbol{r_i})$ and integrating over whole space leads to [44]

$$\sum_j c_{j\boldsymbol{k}}\Bigg[\int \phi^*(\boldsymbol{r}-\boldsymbol{r_i})H\phi(\boldsymbol{r}-\boldsymbol{r_j})d\boldsymbol{r} - E\int \phi^*(\boldsymbol{r}-\boldsymbol{r_i})\phi(\boldsymbol{r}-\boldsymbol{r_j})d\boldsymbol{r}\Bigg] = 0. \tag{3.4}$$

This can be rewritten using Eqs. 3.1 to 3.3 as

$$\sum_j \exp(i\boldsymbol{k}\cdot\boldsymbol{r_j})\Bigg[\int \phi^*(\boldsymbol{r}-\boldsymbol{r_i})\Big(V(\boldsymbol{r})-U(\boldsymbol{r})\Big)\phi(\boldsymbol{r}-\boldsymbol{r_j})d\boldsymbol{r} + (\varepsilon - E)\int \phi^*(\boldsymbol{r}-\boldsymbol{r_i})\phi(\boldsymbol{r}-\boldsymbol{r_j})d\boldsymbol{r}\Bigg] = 0. \tag{3.5}$$

[1] Combining two hydrogen atoms, two Coulomb potentials would give us $V(\boldsymbol{r})$ for H_2^+, not for H_2.

The tight-binding approximation introduces the following parametrization:

$$\int \phi^*(\boldsymbol{r}-\boldsymbol{r_i})\Big(V(\boldsymbol{r})-U(\boldsymbol{r})\Big)\phi(\boldsymbol{r}-\boldsymbol{r_j})\mathrm{d}\boldsymbol{r} = \begin{cases} \epsilon_0 & \text{if } i=j \\ \tau & \text{if } i,j \text{ n.n.} \\ 0 & \text{otherwise,} \end{cases} \tag{3.6}$$

where n.n. means nearest neighbors. Here, we assume that all nearest neighbor contributions are the same, as is the case, e.g., if the orbitals are spherically symmetric. The Coulomb integral, parametrized by ϵ_0, is always negative, since $V(\boldsymbol{r})-U(\boldsymbol{r})<0$ to satisfy the minimum energy requirement. The sign of the hopping integral, parametrized by τ, depends on the signs of the overlapping parts of the involved orbitals. If they have the same sign, as in the case of s orbitals, $\tau<0$. This is what we will usually assume throughout this work. The hopping integrals τ are responsible for the broadening of the discrete atomic levels into an energy band. They are functions of the direction cosines of $\boldsymbol{r_i}-\boldsymbol{r_j}$ and of a limited number of parameters (Slater-Koster parameters [34]) which decrease rapidly with the interatomic distance (at least as r^{-2}).

If we assume that the orbitals do not overlap considerably, i.e., the electrons are *tightly bound* to the atoms, we can write

$$\int \phi^*(\boldsymbol{r}-\boldsymbol{r_i})\phi(\boldsymbol{r}-\boldsymbol{r_j})d\boldsymbol{r} = \delta_{ij}, \tag{3.7}$$

which allows us to simplify Eq. 3.5 with the help of Eq. 3.6 to obtain the dispersion relation

$$E(\boldsymbol{k}) = \epsilon_0 + \tau\sum_{\boldsymbol{\delta_i}} \exp(i\boldsymbol{k}\cdot\boldsymbol{\delta_i}), \tag{3.8}$$

where vectors $\boldsymbol{\delta_i}$ connect the atom at the origin with its nearest neighbours.

Note that we can rewrite Eq. 3.5 as follows:

$$\int \phi^* H\phi \mathrm{d}\boldsymbol{r} - \int \phi^*(V-U)\phi\mathrm{d}\boldsymbol{r} = \varepsilon, \tag{3.9}$$

meaning that if we set the atomic energy level to zero, $\varepsilon=0$, we can replace $V-U$ by H in Eq. 3.6. This justifies speaking of the parametrization of Eq. 3.6 as parametrization of Hamiltonian's H matrix elements.

3.2 One-dimensional systems

In this section, we will study Green's functions of one-dimensional tight-binding chains. We derive explicit formulae and discuss different boundary conditions. First, we present results for infinite chains, since the derivation is more straightforward. The discussion of finite chains will follow afterwards.

Let us first consider a linear chain of atoms with spacing a, such that each atom possesses a single electron orbital. These orbitals are assumed to be identical and mutually orthogonal. Then, using Eqs. 3.4 and 3.6 we obtain the set of equations

$$(E-\epsilon_0)c_{jk} - \tau(c_{(j+1)k} + c_{(j-1)k}) = 0,\ \ j=2,3,\ldots,N-1, \tag{3.10}$$

with the last two equations for $j = 1, N$ fixed by boundary conditions. To solve this equation, we use the ansatz

$$c_{jk} = Ae^{ijka} + Be^{-ijka}, \tag{3.11}$$

where a is the atomic spacing and A, B are constants. Alternatively, we can put $c_{jk} = \widetilde{A}\cos(jka) + \widetilde{B}\sin(jka)$. In the following sections we apply different boundary conditions to the chain.

3.2.1 A chain with periodic boundary conditions

If we apply periodic boundary conditions, i.e., write $c_{nk} = c_{(n+N)k}$, then the quantum number k is quantized according to the condition $e^{iNka} = 1$, i.e., we obtain $k = \frac{2\pi}{Na}m$, $m = -\frac{N}{2} + 1, ..., \frac{N}{2}$. The Hamiltonian matrix representation has the form of a tridiagonal matrix with added τs in the corners

$$\begin{pmatrix} \epsilon_0 & \tau & 0 & \cdots & & \tau \\ \tau & \epsilon_0 & \tau & 0 & \vdots & \\ 0 & \ddots & \ddots & \ddots & 0 & \vdots \\ \vdots & \cdots & 0 & \tau & \epsilon_0 & \tau \\ \tau & \cdots & 0 & 0 & \tau & \epsilon_0 \end{pmatrix}. \tag{3.12}$$

This is a circulant matrix and therefore diagonalizable in a Fourier basis. As discussed previously, the eigenvectors can be found by exploiting the periodicity, i.e., we obtain the Bloch states

$$c_{jk} = \frac{1}{\sqrt{N}}e^{ijka}, \tag{3.13}$$

or

$$|\psi_k\rangle = \frac{1}{\sqrt{N}}\sum_j e^{ijka}\,|\phi_j\rangle\,. \tag{3.14}$$

Note that all of these solutions are equally represented on each atom of the chain. They constitute a basis in which the Hamiltonian is diagonal and, from Eq. 3.8, its eigenspectrum (dispersion relation) has the form

$$E(k) = \epsilon_0 + 2\tau\cos(ka),\ k = \frac{2\pi}{Na}m\,,\ m = \frac{N}{2} + 1, \ldots, \frac{N}{2}, \tag{3.15}$$

or, equivalently:

$$E(k) = \epsilon_0 + 2\tau\cos\left(\frac{2k\pi}{N}\right),\ k = 1, 2, \ldots, N. \tag{3.16}$$

Once we know the eigenvectors and the dispersion relation, we can calculate Green's functions. From Eqs. 2.16 and 3.14, we can write the real space matrix element of the Green's function $\hat{g}$ for an infinite chain as a sum over "quasimomenta" k:

$$\hat{g}_{\mathrm{j,l}}(E) = \sum_k \frac{\langle\psi_j|\psi_k\rangle\,\langle\psi_k|\psi_l\rangle}{E - E(k)} = \frac{1}{N}\sum_k \frac{e^{ika(j-l)}}{E - E(k)}. \tag{3.17}$$

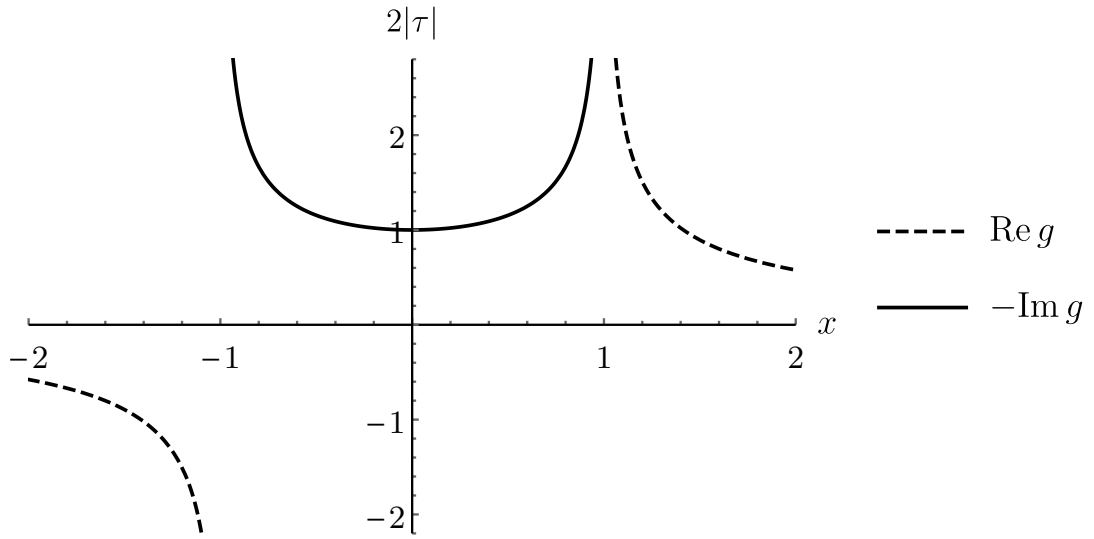

Figure 3.1: Real and imaginary parts of the Green's function of an infinite chain $g_{jj}(x)$ as a function of the reduced energy parameter $x = \frac{E-\epsilon_0}{2|\tau|}$.

Transforming the sum into an integral in the limit $N \to \infty$, we obtain

$$\hat{g}_{\mathrm{j,l}}(E) = \frac{a}{2\pi}\int_{-\pi/a}^{\pi/a} dk \frac{e^{ika(j-l)}}{E - \epsilon_0 - 2\tau\cos(ka)}. \tag{3.18}$$

The evaluation of this integral using the methods of complex analysis is presented in Appendix A. The result, which is valid for the scaled energy parameter $x = \frac{E-\epsilon_0}{2|\tau|} \in (-1, 1)$ defining the only continuous part of the spectrum (band) is given by

$$\hat{g}_{j,l}(x) = \frac{-i}{2|\tau|\sqrt{1-x^2}}\left(x - i\sqrt{1-x^2}\right)^{|j-l|}. \tag{3.19}$$

The real and imaginary parts of the diagonal matrix element ($j = l$) are plotted in Fig. 3.1. Note that the function is purely imaginary within the band, and outside the band it is real. Both real and imaginary parts have square root singularities at the band edges, which is typical of a 1D system [36]. These asymmetric spikes are a hallmark of low-dimensional systems (known as van Hove singularities), and indicate the presence of a flat region of the dispersion curve (i.e., zero derivative) with large accumulation of states.

Finally, the local density of states is

$$n_j(x) = \frac{-1}{\pi}\operatorname{Im}\hat{g}_{j,j}(E) = \frac{1}{2\pi|\tau|\sqrt{1-x^2}}, \text{ with } x = \frac{E-\epsilon_0}{2|\tau|} \in (-1, 1). \tag{3.20}$$

Note that $\int_{-1}^{1} n_j(x)dx = 1/(2|\tau|)$, so the total number of states per atom is one, as required.

3.2.2 A chain with fixed ends

Consider the condition $c_{0k} = c_{(N+1)k} = 0$, i.e. we have standing waves as solutions, namely,

$$c_n = \sin(kna). \tag{3.21}$$

From the condition $\sin((N+1)ka) = 0$ we have that $k = \frac{\pi m}{(N+1)a}$ for $m = 1, \ldots, N$.

Since we broke the invariance to lattice translations, the sites at the ends are no longer equivalent with the other sites in the system. The allowed momentum values cover only the positive half of the Brillouin zone (the negative k give the same eigenfunctions) but are twice as dense as those that we found with periodic boundary conditions. The eigenvectors and eigenvalues for this case are derived in Appendix B.

A Green's function for the semi-infinite chain can be derived analogously to the infinite chain discussed above. Namely, from Eqs. 2.16, 3.14, and 3.21, the matrix element of $\hat{g}$ is given by

$$\hat{g}_{\mathrm{j,l}}(E) = \sum_k \frac{\langle\psi_j|\psi_k\rangle\,\langle\psi_k|\psi_l\rangle}{E - E(k)} = \frac{1}{N}\sum_k \frac{\sin(jka)\sin(lka)}{E - E(k)}. \tag{3.22}$$

Transforming the sum into an integral we obtain

$$\hat{g}_{\mathrm{j,l}}(E) = \frac{a}{2\pi}\int_{-\pi/a}^{\pi/a} dk \frac{\sin(jka)\sin(lka)}{E - \epsilon_0 - 2\tau\cos(ka)}. \tag{3.23}$$

The evaluation of the integral for $j = l = 1$ is presented in Appendix A. The resulting Green's function $\hat{g}_{1,1}(E)$ is

$$\hat{g}_{1,1}(E) = \frac{1}{|\tau|}\begin{cases} \left(x - i\sqrt{1-x^2}\right) & \text{if } |x| \le 1, \\ \left(x - \mathrm{sgn}x\sqrt{x^2-1}\right) & \text{if } |x| > 1, \end{cases} \tag{3.24}$$

where the sgn$x$ assures that $\lim_{|\tau|\to 0+} g_{1,1}(E) = \frac{1}{E-\epsilon_0}$.[2]

Then, the local density of states has a characteristic semi-circular shape (as shown in Fig. 3.2)

$$n(E) = \frac{1}{\pi|\tau|}\sqrt{1-x^2}, \text{ with } x = \frac{E-\epsilon_0}{2|\tau|} \in [-1, 1]. \tag{3.25}$$

Let us briefly mention the case of a diatomic chain with alternating orbital energies of $\epsilon_0 \pm \Delta$. In this case, one can derive (see, e.g., [45]) the following generalization of the above Green's function expression (with $\delta = \Delta/2|\tau|$):

$$\hat{g}_{1,1}(E) = \frac{1}{|\tau|}\begin{cases} x + \delta - i\sqrt{\frac{x+\delta}{x-\delta} - (x+\delta)^2}, & \text{if } |\delta| < |x| \le \sqrt{1+\delta^2} \\ x + \delta - \mathrm{sgn}(x+\delta)\sqrt{(x+\delta)^2 - \frac{x+\delta}{x-\delta}}, & \text{if } |x| > \sqrt{1+\delta^2} \text{ or } |x| \le |\delta|. \end{cases} \tag{3.26}$$

The plot of this function is shown in Fig. 3.3. Interestingly, there is a gap in the local DOS of width δ dividing the energy band into two. Also, at δ, there is a van Hove singularity.

3.2.3 Green's functions for finite chains

In case of finite tight-binding chains of length N, the real space representation of the Green's function for small N can be most easily computed numerically

[2] To obtain the limit, we use the Taylor expansion for the square root: $\sqrt{x^2-1} = \pm x\sqrt{1-1/x^2} \approx \pm x(1-1/2x^2)$ for x large, i.e., τ small.

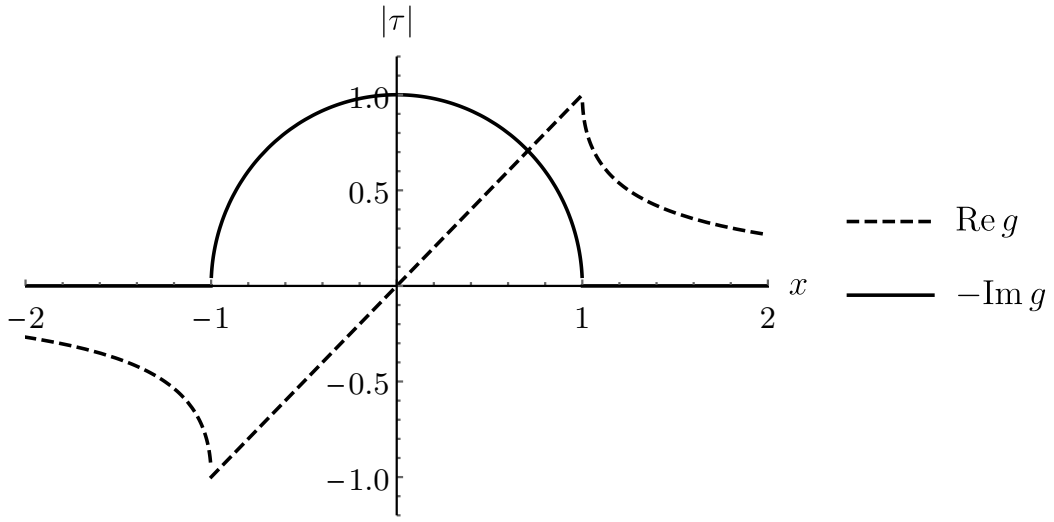

Figure 3.2: Real and imaginary parts of $g_{jj}(x)$ for a semi-infinite chain as a function of the reduced energy parameter $x = \frac{E-\epsilon_0}{2|\tau|}$.

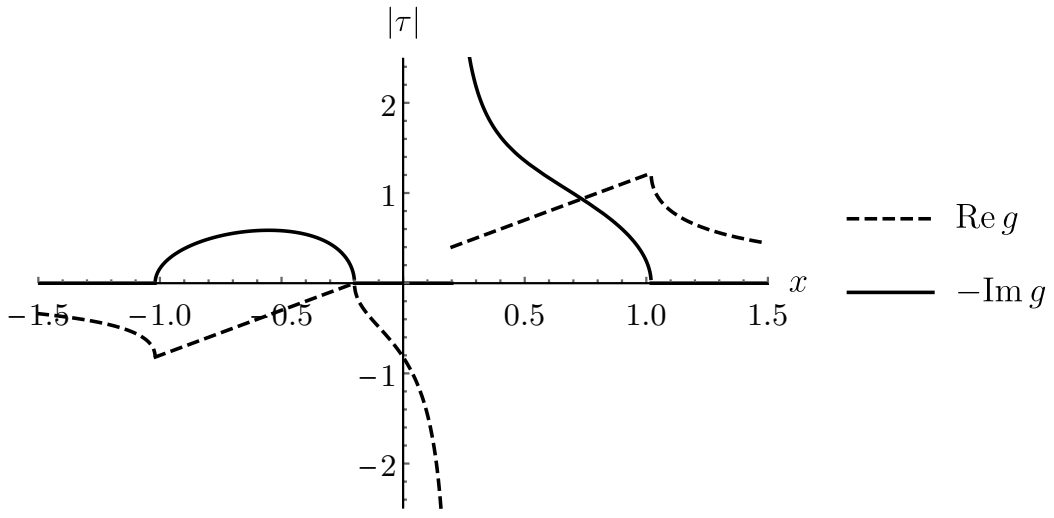

Figure 3.3: Real and imaginary parts of $g_{11}(x)$ for a diatomic semi-infinite chain with $\delta = \Delta/2|\tau| = 0.2$ as a function of the reduced energy parameter $x = \frac{E-\epsilon_0}{2|\tau|}$.

by matrix inversion $(E-H)^{-1}$. Alternatively, if we are interested in a diagonal element of $g(E)$, we can employ the continued fraction technique introduced in the previous chapter.

General expressions for Green's functions can also be derived as a simple closed expression in terms of Chebyshev polynomials for a wide range of different boundary conditions [46]. Here, we will follow the derivation of Bass, even though different approaches have since appeared in the literature (for example, Ref. [47]).

The crucial step is to notice that the equation for the Green's function[3]

$$zG_{n,m} - \tau(G_{n-1,m} + G_{n+1,m}) = \delta_{nm}, \tag{3.27}$$

is for $n \neq m$ and $\tau = 1/2$ the recurrence relation for Chebyshev polynomials. Chebyshev polynomials of the first kind can be defined as the unique polynomials satisfying

$$T_n(\cos\theta) = \cos n\theta, \tag{3.28}$$

for $n = 0, 1, 2, 3, ...$ while polynomials of the second kind satisfy

$$U_n(\cos\theta) = \frac{\sin(n\theta+\theta)}{\sin\theta}. \tag{3.29}$$

Since $U_{-1}(z) = 0$, it is easy to see that $-U_{|n-m|-1}(z)/2\tau$ is a particular solution to Eq. 3.27.

Due to the symmetry $G_{n,m}(z) = G_{m,n}(z)$, the Green's function can be written in a general form [46]

$$G_{n,m}(z) = a(z)T_{n-m}(z) + b(z)T_{n+m}(z) + c(z)U_{n+m-1}(z) - U_{|n-m|-1}(z), \tag{3.30}$$

where $a(z), b(z), c(z)$ are determined by boundary conditions.

Periodic boundary conditions

With periodic boundary conditions (PBC), we expect that $G_{n,m}$ depends only on the difference $n-m$, therefore:

$$G_{n,m}(z) = a(z)T_{n-m}(z) - U_{|n-m|-1}(z), \quad \text{(PBC)}. \tag{3.31}$$

Obviously, since $T_0(z) = 1$ and $U_{-1}(z) = 0$, we must have $G_{n,n} = a(z)$, and the PBC $G_{N,0} = G_{0,0}$ means that

$$G_{n,n}(z) = \frac{U_{N-1}(z)}{T_N(z)-1} = \frac{\sin N\theta}{2|\tau|(\cos(N\theta)-1)\sin\theta}, \text{ with } \theta = \arccos\frac{z}{2|\tau|}. \tag{3.32}$$

In Fig. 3.4, the plot of $-\operatorname{Im} G_{n,n}(z)$, representing the local DOS on any of the N atoms, is shown for $z = (E+i\eta)/2|\tau|$, with η small but large enough to smear out peaks. It can be seen that for N large, the shape of the plot is becoming increasingly similar to the one in Fig. 3.1 derived for an infinite chain. However, divergences at the band edges are only present for $N = 2$, not for N large.

[3]This corresponds to the N-atom lattice model with the equation of motion $2zu_n - u_{n+1} - u_{n-1} = 0$, where u_n is the displacement of the nth particle from its equilibrium position and $z = 1-\omega^2$ with ω dimensionless frequency. Also, note that in this section, we set the atomic level $\epsilon_0 = 0$.

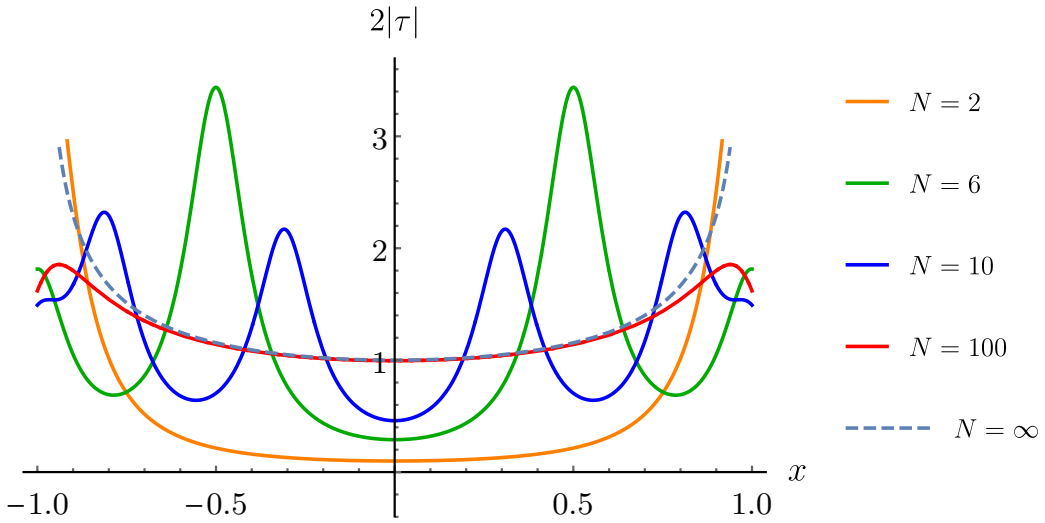

Figure 3.4: The plot of $-\operatorname{Im} G_{n,n}(z)$ as a function of scaled energy $z = (E + i\eta)/2|\tau|$, representing the local DOS on any atom of N-atom long tight-binding chains of atoms with periodic boundary conditions. Note that $\eta = 0.1$ to smear out peaks.

Fixed ends

In this case, the condition reads $G_{0,m} = 0 = G_{N+1,m}$ for all $m \geq 0$. The first condition applied to the general expansion in Eq. 3.30 results in

$$G_{0,m} = 0 = (a(z) + b(z))T_m(z) + (c(z) - 1)U_{m-1}(z), \tag{3.33}$$

meaning that $b(z) = -a(z)$ and $c(z) = 1$. The second condition gives

$$G_{N+1,m} = 0 = a(z)(T_{N+1-m}(z) - T_{N+1+m}(z)) + U_{N+m}(z) - U_{N-m}(z), \tag{3.34}$$

which can be rewritten using well-known identities [48]

$$T_{n+m}(z) - T_{n-m}(z) = 2(z^2 - 1)U_{n-1}U_{m-1} \tag{3.35}$$

$$U_{n+m-1}(z) + U_{n-m-1}(z) = 2U_{n-1}T_m \tag{3.36}$$

to obtain

$$G_{N+1,m} = 0 = [-2a(z)(z^2 - 1)U_N(z) + T_{N+1}(z)]U_{m-1}(z),$$

so that

$$a(z) = \frac{T_{N+1}(z)}{2(z^2 - 1)U_N(z)}$$

and the Green's function has the form [46]

$$G_{n,m}(z) = (T_{n-m}(z) - T_{n+m}(z))\frac{T_{N+1}(z)}{2(z^2 - 1)U_N(z)} + U_{n+m-1}(z) - U_{|n-m|-1}(z). \tag{3.37}$$

The onsite (diagonal) element is

$$G_{n,n}(z) = (1 - T_{2n}(z))\frac{T_{N+1}(z)}{2(z^2 - 1)U_N(z)} + U_{2n-1}(z). \tag{3.38}$$

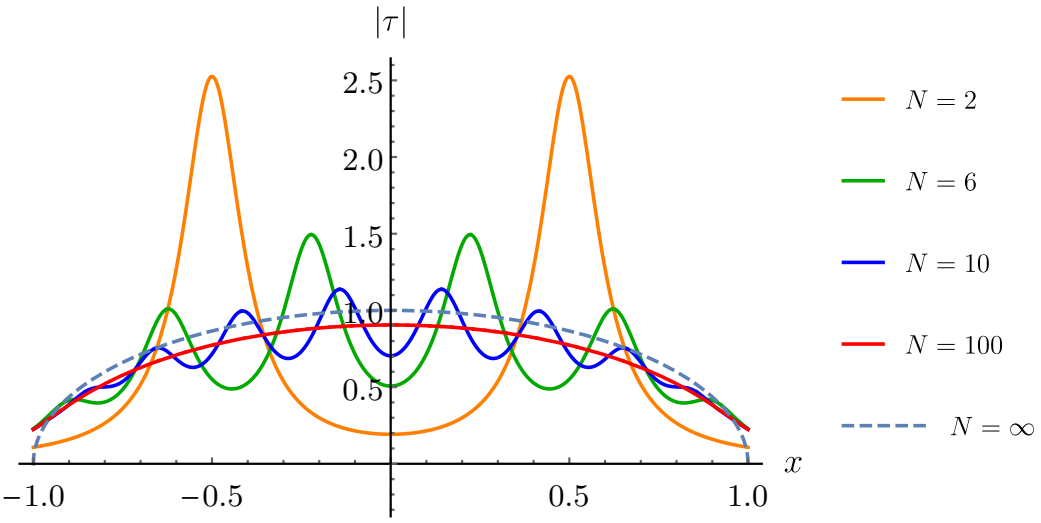

Figure 3.5: The plot of $-\operatorname{Im} G_{1,1}(z)$ as a function of scaled energy $z = (E + i\eta)/2|\tau|$, representing the local DOS on the first atom of N-atom long tight-binding chains of atoms with fixed ends according to Eq. 3.39. Here, $\eta = 0.1$.

If we fix $n = 1$ corresponding to the "surface" atom, and recall that $z = 2|\tau|\cos\theta$, we obtain:[4]

$$G_{1,1}(z) = (1-2z^2+1)\frac{\cos(N+1)\theta\sin\theta}{2|\tau|(z^2-1)\sin(N+1)\theta} + z/|\tau| = \frac{\sin N\theta}{|\tau|\sin(N+1)\theta}. \quad (3.39)$$

In Fig. 3.5, we show $-\operatorname{Im} G_{1,1}(z)$ (the local DOS on the first ("surface") atom) for various N (total number of atoms). Note that we set $\eta = 0.1$ to smear out the peaks. We can observe convergence towards the semi-infinite chain limit (compare with Fig. 3.2).

3.3 Two-dimensional systems

In this section, electronic properties of square and hexagonal two-dimensional lattices are discussed. Namely, we present analytical methods for obtaining Green's functions and derived quantities such as local density of states.

3.3.1 Square lattice

Consider a simple uniform square lattice with the lattice parameter a. A calculation of tight-binding Green's function is directly analogous to the calculation in the case of one-dimensional infinite chain (see Eqs. 3.17 and 3.18). However, instead of "quasimomenta" k in 1D case, here we speak of (2D) reciprocal lattice vectors $\boldsymbol{k}$.

From Eq. 3.8, considering four nearest neighbours, a dispersion relation can be obtained in the form

$$E(\boldsymbol{k}) = \epsilon_0 + 2\tau(\cos(k_x a) + \cos(k_y a)). \quad (3.40)$$

[4]Here, we use the definition of Chebyshev polynomials (Eqs. 3.28 and 3.29) together with the identity $\sin(a+b) = \sin a\cos b + \cos a\sin b$.

Let us denote a reciprocal lattice vector $\boldsymbol{k} = k_x\hat{x} + k_y\hat{y}$, similarly for direct lattice vectors $\boldsymbol{j}, \boldsymbol{l}$. The first Brillouin zone (BZ) is defined by $-\frac{\pi}{a} \leq k_x, k_y < \frac{\pi}{a}$. Then a direct space matrix element of the Green's function reads

$$g_{\boldsymbol{j},\boldsymbol{l}}(E) = \frac{a^2}{4\pi^2}\int_{-\pi/a}^{\pi/a} dk_x \int_{-\pi/a}^{\pi/a} dk_y \frac{e^{i\boldsymbol{k}\cdot(\boldsymbol{j}-\boldsymbol{l})a}}{E - \epsilon_0 + i\eta - 2\tau(\cos(k_x a) + \cos(k_y a))} \tag{3.41}$$

Let us now introduce a substitution $\phi_x = k_x a$, $\phi_y = k_y a$ and notation $m = (j_x - l_x)$, $n = (j_y - l_y)$ for m, n integers. To find the solution, we start by keeping only the even terms in the integral, since the domain is symmetric

$$g_{\boldsymbol{j},\boldsymbol{l}}(E) = \frac{1}{\pi^2}\int_0^{\pi} d\phi_x \int_0^{\pi} d\phi_y \frac{\cos(m\phi_x)\cos(n\phi_y)}{E - \epsilon_0 + i\eta - 2\tau(\cos(\phi_x) + \cos(\phi_y))} \tag{3.42}$$

To simplify the integral, it is useful to make a transformation[5] due to Morita [49], namely: $m' = m + n$, $n' = m - n$ and $\phi'_x = \frac{\phi_x + \phi_y}{2}$, $\phi'_y = \frac{\phi_x - \phi_y}{2}$. Then using the identity turning a sum into a product of cosines, we obtain

$$g_{\boldsymbol{j},\boldsymbol{l}}(E) = \frac{1}{\pi^2}\int_0^{\pi} d\phi_x \int_0^{\pi} d\phi_y \frac{\cos((m+n)\phi_x)\cos((m-n)\phi_y)}{E - \epsilon_0 + i\eta - 4\tau(\cos(\phi_x)\cos(\phi_y))} \tag{3.43}$$

An arbitrary matrix element $g_{\boldsymbol{j},\boldsymbol{l}}(E)$ can be determined through recurrence relations in terms of the diagonal elements, $g_{\boldsymbol{j},\boldsymbol{j}}(E)$ [50].

Along the diagonal ($m = n = 0$, corresponding to $\boldsymbol{j} = \boldsymbol{l}$) the numerator in the above equation is 1 and we can write

$$\begin{aligned} g_{\boldsymbol{j},\boldsymbol{j}}(z) &= \frac{1}{\pi^2}\int_0^{\pi} d\phi_x \int_0^{\pi} d\phi_y \frac{1}{z - \epsilon_0 - 4\tau(\cos(\phi_x)\cos(\phi_y))} \\ &= \frac{1}{\pi}\int_0^{\pi} d\phi_x \frac{1}{\sqrt{(z-\epsilon_0)^2 - 4\tau^2\cos^2(\phi_x)}}. \end{aligned}$$

This can be expressed in terms of the elliptic integral of the first kind defined as $\mathcal{K}(\lambda) = \int_0^{\pi} \frac{d\phi}{\sqrt{1-\lambda^2\cos^2\phi}}$, i.e.,

$$g_{\boldsymbol{j},\boldsymbol{j}}(E) = \frac{2}{\pi(E-\epsilon_0)}\mathcal{K}\left(\frac{4|\tau|}{E-\epsilon_0}\right), \; |E - \epsilon_0| > 4|\tau|. \tag{3.44}$$

This expression holds for energies outside the band, where $g_{\boldsymbol{j},\boldsymbol{j}}(E)$ is real. But for E within the band, the analytic continuation of $\mathcal{K}(\lambda)$ must be used [48]:

$$\mathcal{K}(1/k) = k\left(\mathcal{K}(k) + i\mathcal{K}(\sqrt{1-k^2})\right).$$

The density of states is then given by [36]

$$n(E) = -\frac{1}{\pi}\operatorname{Im} g_{\boldsymbol{j},\boldsymbol{j}}(E) = \frac{1}{2|\tau|\pi^2}\mathcal{K}\left(\sqrt{1 - \frac{(E-\epsilon_0)^2}{(4\tau)^2}}\right). \tag{3.45}$$

Note that the DOS exhibits at both band edges a discontinuity that produces the logarithmic singularities of the $\operatorname{Re} g$ at the band edges (see Fig. 3.6). This behavior is characteristic of the two-dimensionality of the system. Note also the singularity at the interior of the band (at $E = \epsilon_0$); the $\operatorname{Re} g$ is discontinuous there and $\operatorname{Im} g$ has a logarithmic singularity. The singularities of g within the band are associated with saddle points in the function $E(k)$. A minimum number of such saddle points exists and depends on the number of independent variables [36].

[5] This corresponds to rotating the coordinate axes in the square lattice by $\pi/4$.

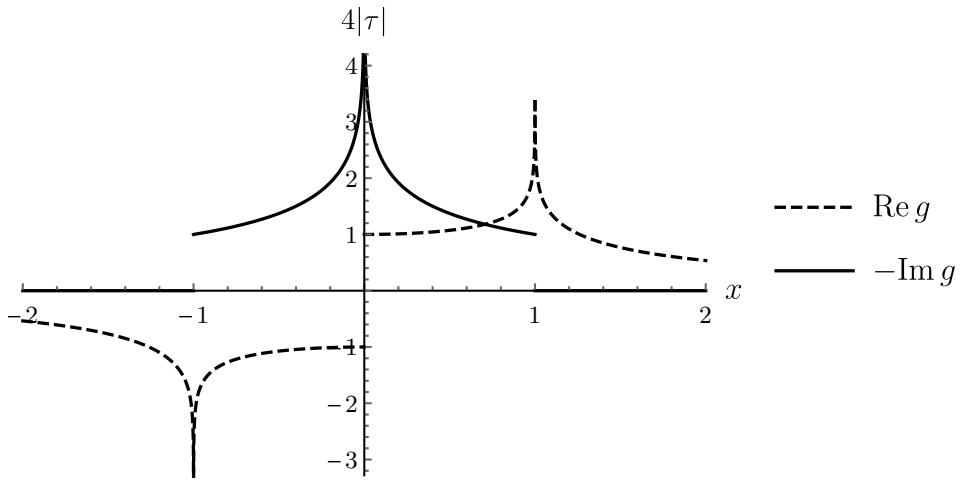

Figure 3.6: Real and imaginary parts of the diagonal Green's function $g_{00}(x)$ for the square lattice with the reduced energy parameter $x = \frac{E-\epsilon_0}{4|\tau|}$.

3.3.2 Hexagonal (honeycomb) lattice

The triangular lattice is the two-dimensional close-packed lattice. The honeycomb lattice contains two atoms per elementary cell and is composed of two triangular sublattices denoted A and B, each atom from sublattice A being surrounded by three atoms from sublattice B (see Fig. 3.7).

Let us choose lattice vectors conveniently as

$$\boldsymbol{a}_1 = a\begin{pmatrix} \frac{\sqrt{3}}{2} \\ \frac{3}{2} \end{pmatrix}, \boldsymbol{a}_2 = a\begin{pmatrix} -\frac{\sqrt{3}}{2} \\ \frac{3}{2} \end{pmatrix},$$

where a is the nearest neighbor distance[6] and the corresponding reciprocal lattice vectors are then:

$$\boldsymbol{b}_1 = \frac{2\pi}{\sqrt{3}a}\begin{pmatrix} 1 \\ \frac{1}{\sqrt{3}} \end{pmatrix}, \boldsymbol{b}_2 = \frac{2\pi}{\sqrt{3}a}\begin{pmatrix} -1 \\ \frac{1}{\sqrt{3}} \end{pmatrix}.$$

The unit cell area is $\frac{3\sqrt{3}a^2}{2}$ and the first Brillouin zone (BZ) of the reciprocal lattice, defined by the planes bisecting the vectors to the nearest reciprocal lattice points, has the area of $V_{BZ} = \frac{8\pi^2}{3\sqrt{3}a^2}$. It is clear that the six points at the corners of the BZ fall into two groups of three, so one needs to consider only two corners that we label K and K' as in the right hand side of Fig. 3.7. The BZ has a hexagonal shape which makes the integration over it inelegant. By exploiting the periodicity and symmetry of reciprocal space it is possible to choose instead a rectangular area that is fully equivalent to the hexagonal BZ (see Fig. 3.7), thus vastly simplifying the calculation of subsequent integrals.

Further, it is convenient to express the positions of neighboring atoms (see Fig. 3.7) as follows:

$$\boldsymbol{\delta}_1 = a\begin{pmatrix} \frac{\sqrt{3}}{2} \\ \frac{1}{2} \end{pmatrix}, \boldsymbol{\delta}_2 = a\begin{pmatrix} -\frac{\sqrt{3}}{2} \\ \frac{1}{2} \end{pmatrix}, \boldsymbol{\delta}_3 = a\begin{pmatrix} 0 \\ -1 \end{pmatrix}.$$

[6]The distance between nearest neighbours of the same sublattice is $\sqrt{3}a$

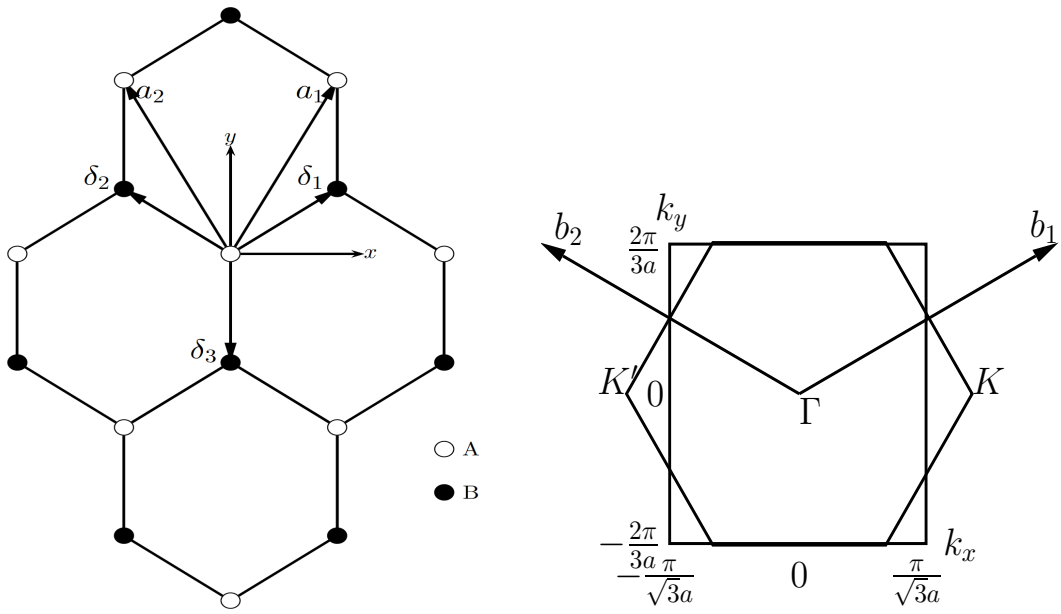

Figure 3.7: Hexagonal (honeycomb) lattice in the real space (left) and reciprocal space (right).

The choice of the tight-binding basis is not unique: two bases are widely used in the literature, differing by relative phase factors between their components [51]. The eigenfunctions of the tight-binding Hamiltonian and expectation values of operators describing physical quantities are of course independent of the choice of a basis. We write down the eigenstates of the lattice Hamiltonian as linear combinations of two Bloch functions corresponding respectively to the A and B atoms, but with a different phase factor attached to each atom [51]

$$\psi_{\boldsymbol{k}}(\boldsymbol{r}) = \frac{1}{\sqrt{N}} \sum_j \left[e^{i\boldsymbol{k}\cdot\boldsymbol{r}_j^{\boldsymbol{A}}} c_{\boldsymbol{k}}^A \phi(\boldsymbol{r} - \boldsymbol{r}_j^A) + e^{i\boldsymbol{k}\cdot\boldsymbol{r}_j^{\boldsymbol{B}}} c_{\boldsymbol{k}}^B \phi(\boldsymbol{r} - \boldsymbol{r}_j^B) \right], \tag{3.46}$$

ϕ represent orbitals (e.g. p_z) for two atoms A, B, in a unit cell, j runs through the N unit cells in the sheet. The tight-binding Hamiltonian in this basis is described by the 2×2 matrix

$$\hat{H}_0(\boldsymbol{k}) = \begin{pmatrix} \epsilon_A & tS(\boldsymbol{k}) \\ tS^*(\boldsymbol{k}) & \epsilon_B \end{pmatrix} \tag{3.47}$$

where $S(\boldsymbol{k}) = \sum_{\boldsymbol{\delta_i}} e^{i\boldsymbol{k}\cdot\boldsymbol{\delta_i}} = 2\exp(ik_y a/2)\cos\left(k_x a\sqrt{3}/2\right) + \exp(-ik_y a)$ is a geometric factor. In the nearest-neighbour approximation, there are no hopping processes within the sublattices; hopping occurs only between them. The hopping parameter t corresponds to τ from previous sections.

Let us now discuss the case of $\epsilon_A = \epsilon_B = 0$, representing a uniform hexagonal structure such as graphene. The symmetry group of the honeycomb lattice contains swapping the two sublattices. Hence, for each value of the quasimomentum $\boldsymbol{k}$ within the Brillouin zone, two states exist with energies $\pm\epsilon(\boldsymbol{k})$. Explicitly, the

two eigenvalues of the Hamiltonian matrix $\hat{H}_0(\boldsymbol{k})$ are given by

$$\epsilon_{\pm}(\boldsymbol{k}) = \pm t\sqrt{S^*(\boldsymbol{k})S(\boldsymbol{k})} = \pm t|1 + e^{-ik\cdot a_1} + e^{-ik\cdot a_2}| = \tag{3.48}$$

$$= \pm t\sqrt{1 + 4\cos\frac{3}{2}k_y a\cos\frac{\sqrt{3}}{2}k_x a + 4\cos^2\frac{\sqrt{3}}{2}k_x a}. \tag{3.49}$$

At the corners of the Brillouin zone, for example at $K = (\frac{4\pi}{3\sqrt{3}a}, 0)$ and $K' = (-\frac{4\pi}{3\sqrt{3}a}, 0)$, as shown in Fig. 3.7, the two bands touch, i.e. $\epsilon_+ = \epsilon_- = 0$. This is the well-known Dirac cone of graphene.

The eigenstates of the lattice Hamiltonian can be found using Eq. 3.46 in the form [51]

$$\psi_{k\pm}(\boldsymbol{r}) = \frac{1}{\sqrt{2N}}\sum_j \left[e^{i\boldsymbol{k}\cdot\boldsymbol{r_j^A}}\phi(\boldsymbol{r} - \boldsymbol{r_j^A}) \pm e^{i\theta}e^{i\boldsymbol{k}\cdot\boldsymbol{r_j^B}}\phi(\boldsymbol{r} - \boldsymbol{r_j^B})\right], \tag{3.50}$$

where $\theta(\boldsymbol{k}) = \arg S(\boldsymbol{k})$ is a geometric factor.

As usual, the Green's function in the k-representation is found by inverting the matrix $E\hat{I} - \hat{H}_0$, namely

$$g(E, \boldsymbol{k}) = \lim_{\eta\to 0+}\frac{1}{(E+i\eta)^2 - |\epsilon(k)|^2}\begin{pmatrix} E+i\eta & tS(\boldsymbol{k}) \\ tS^*(\boldsymbol{k}) & E+i\eta\end{pmatrix}. \tag{3.51}$$

We will focus on the first element, which reads

$$g_{AA}(E, \boldsymbol{k}) = \lim_{\eta\to 0+}\frac{E}{(E+i\eta)^2 - |\epsilon(k)|^2}. \tag{3.52}$$

The Green's function in the Hamiltonian eigenbasis is written formally as

$$g(E) = \sum_{\boldsymbol{k}}\left(\frac{|k+\rangle\langle k+|}{E - \epsilon_+(\boldsymbol{k})} + \frac{|k-\rangle\langle k-|}{E - \epsilon_-(\boldsymbol{k})}\right). \tag{3.53}$$

Fourier transforming to the real space, i.e., projecting onto two different states $|\phi_j, A\rangle$, $|\phi_l, A\rangle$, using Eq. 3.50:

$$\langle\phi_j, A|\hat{g}(E)|\phi_l, A\rangle = \frac{1}{2N}\sum_{\boldsymbol{k}}\left(\frac{e^{i\boldsymbol{k}\cdot(\boldsymbol{r_j}-\boldsymbol{r_l})}}{E - \epsilon_+(\boldsymbol{k})} + \frac{e^{i\boldsymbol{k}\cdot(\boldsymbol{r_j}-\boldsymbol{r_l})}}{E - \epsilon_-(\boldsymbol{k})}\right). \tag{3.54}$$

Note that for every $\boldsymbol{k}$, $\epsilon_+ = -\epsilon_-$ and also, transforming $\sum_{\boldsymbol{k}} = \frac{N}{V_{BZ}}\int_{\boldsymbol{k}\in B.Z.}$, we obtain

$$g_{j,l}^{A,A}(E) = \langle\phi_i, A|\hat{g}(E)|\phi_j, A\rangle = \frac{1}{V_{BZ}}\int_{\boldsymbol{k}\in B.Z.}\left(\frac{Ee^{ik\cdot(\boldsymbol{r_j}-\boldsymbol{r_l})}}{E^2 - \epsilon_+^2(\boldsymbol{k})}\right). \tag{3.55}$$

Since the shape of the first Brillouin zone can be transformed from a hexagon to a rectangle with the area of V_{BZ} (see Fig. 3.7), we can write

$$g_{j,l}^{A,A}(E) = \frac{3\sqrt{3}a^2}{8\pi^2}\int_{-\pi/\sqrt{3}a}^{\pi/\sqrt{3}a}dk_x\int_{-2\pi/3a}^{2\pi/3a}dk_y\left(\frac{Ee^{ik\cdot(\boldsymbol{r_j}-\boldsymbol{r_l})}}{E^2 - \epsilon_+^2(\boldsymbol{k}) + i\eta}\right). \tag{3.56}$$

We can perform the k_y integral analytically by means of contour integration [52]. The integration contour is extended from a straight line on the real axis

to the boundaries of a semi-infinite rectangle in the upper half of the complex plane. Since the integrand vanishes in the limit $\mathrm{Im}[k_y] \to \infty$ and because the parts of the contour that are parallel to the imaginary axis cancel each other out, the k_y integral can be evaluated by simply identifying a simple pole of the integrand lying inside the integration contour (due to the small imaginary η in the denominator) and finding their respective residues to obtain

$$g_{j,l}^{A,A}(E) = \frac{ia}{4\pi t^2} \int_{-\pi/\sqrt{3}a}^{\pi/\sqrt{3}a} dk_x \frac{E e^{ik_x \Delta_x} e^{iq(k_x)\Delta_y}}{\sin(q(k_x, E)) \cos\Big(\sqrt{3} k_x a/2\Big)}, \tag{3.57}$$

where $\Delta_x = (\boldsymbol{r_j} - \boldsymbol{r_l})_x$, $\Delta_y = (\boldsymbol{r_j} - \boldsymbol{r_l})_y$ and q is given by:

$$q(k_x, E) = \pm \arccos \frac{E^2/t^2 - 1 - 4\cos^2(\sqrt{3}k_x a/2)}{4\cos\Big(\sqrt{3}k_x a/2\Big)}, \tag{3.58}$$

with its sign selected by imposing that q must necessarily lie within the integration contour of the k_y integral.

The single integral above can be easily evaluated numerically. Of special interest is the case of or $j = l = 0$, denoted as $g_{00}(z)$, with its imaginary part corresponding to the (negative of) local DOS. The plot of $g_{00}(z)$ is presented in Fig. 3.8.

Several authors ([50], [53], [54]) found exact closed expressions for hexagonal lattice Green's functions in terms of the complete elliptic integrals of the first and second kind, defined recursively for higher values of j, l. Their results are presented in Appendix C.

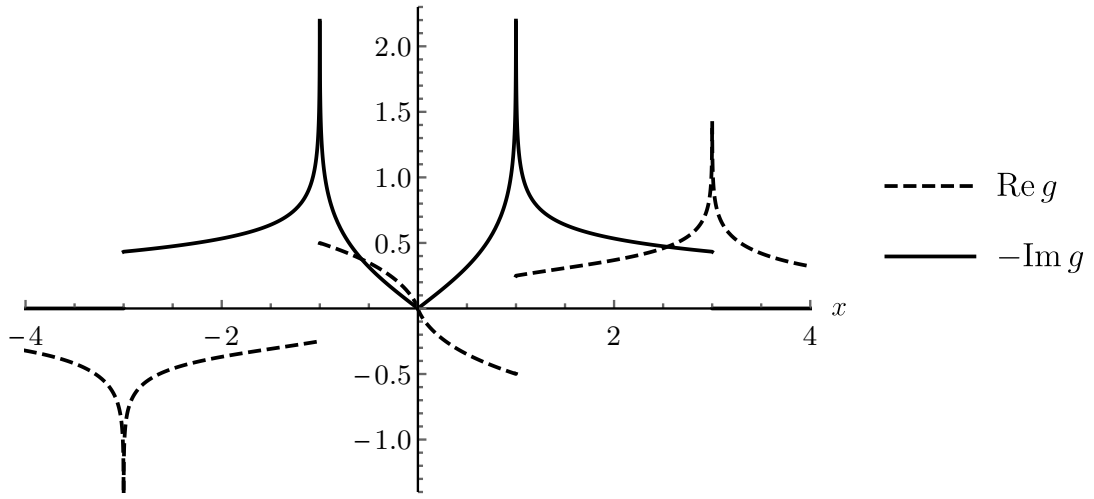

Figure 3.8: The plot of the diagonal Green's function $g_{00}(z)$ for the uniform hexagonal lattice (e.g., graphene) as a function of reduced energy $x = \frac{E-\epsilon_0}{t}$. Here, we set $t = 1$.

As we will later study adsorption on two-dimensional hexagonal boron nitride (hBN) structure, we derive here its Green's function. In essence, we return to the Hamiltonian in the tight-binding basis (see Eq. 3.47) with the condition $\epsilon_A \neq \epsilon_B$.

This asymmetry in the Hamiltonian between the A and B sublattices is liable to lift the degeneracy at the Dirac points K and K'. This could also correspond to so-called gapped, or hydrogenated, graphene, in addition to the hBN structure. The Hamiltonian then reads

$$\hat{H}_{AB}(\boldsymbol{k}) = \begin{pmatrix} \epsilon_A & tS(\boldsymbol{k}) \\ tS^*(\boldsymbol{k}) & \epsilon_B \end{pmatrix} \tag{3.59}$$

where again $S(\boldsymbol{k}) = \sum_{\boldsymbol{\delta}} e^{i\boldsymbol{k}\cdot\boldsymbol{\delta}} = 2\exp(ik_y a/2)\cos\Big(k_x a\sqrt{3}/2\Big) + \exp(-ik_y a)$.

If we set $0 = \frac{\epsilon_A+\epsilon_B}{2}$ and $\Delta = \frac{\epsilon_A-\epsilon_B}{2}$, the Hamiltonian becomes

$$\hat{H}_{AB}(\boldsymbol{k}) = \begin{pmatrix} -\Delta & tS(\boldsymbol{k}) \\ tS^*(\boldsymbol{k}) & \Delta \end{pmatrix}, \tag{3.60}$$

with the eigenvalues

$$\epsilon_{\pm}(\boldsymbol{k}) = \pm\sqrt{\Delta^2 + t^2|S(\boldsymbol{k})|^2}. \tag{3.61}$$

The Green's function in the k-representation is found by inverting the matrix $E\hat{I} - \hat{H}_{AB}$, namely

$$g(E,\boldsymbol{k}) = \lim_{\eta\to 0+} \frac{1}{(E+i\eta)^2 - |\epsilon(k)|^2} \begin{pmatrix} E+i\eta+\Delta & tS(\boldsymbol{k}) \\ tS^*(\boldsymbol{k}) & E+i\eta-\Delta \end{pmatrix}, \tag{3.62}$$

where now $|\epsilon(k)|^2$ is given by Eq. 3.61. Similarly to the procedure above, the real space matrix elements of the Green's function connecting two A sites with positions $\boldsymbol{r_j}$ and $\boldsymbol{r_l}$ are

$$g^{A,A}_{j,l}(E) = \frac{1}{V_{BZ}} \int_{\boldsymbol{k}\in BZ} d^2\boldsymbol{k} \frac{(E+i\eta+\Delta)e^{i\boldsymbol{k}\cdot(\boldsymbol{r_j}-\boldsymbol{r_l})}}{E^2 - \epsilon^2(k) + i\eta}. \tag{3.63}$$

One of the two integrals can be computed analytically using the residue theorem as discussed in the case of graphene. The resulting integral for the diagonal element of the Green's function $j = l = 0$ has the form

$$g^{A,A}_{00}(E) = \frac{ia}{4\pi t^2} \int_{-\pi/\sqrt{3}a}^{\pi/\sqrt{3}a} dk_x \frac{E+\Delta}{\sin(q(k_x,E))\cos\Big(\sqrt{3}k_x a/2\Big)}, \tag{3.64}$$

where $q(q(k_x, E)$ is given as

$$q(k_x,E) = \pm\arccos\frac{(E^2-\Delta^2)/t^2 - 1 - 4\cos^2(\sqrt{3}k_x a/2)}{4\cos\Big(\sqrt{3}k_x a/2\Big)}, \tag{3.65}$$

with its sign selected by imposing that q must necessarily lie within the integration contour of the k_y integral.

The numerical evaluation of $g^{A,A}_{00}(E)$ showing the effect of various values of Δ is shown in Fig. 3.9. Notably, there is an energy gap of 2Δ corresponding to the energy gap in the band structure at the corners of the Brillouin zone, where $S(\boldsymbol{k}) = 0$. Furthermore, we can see that the nonzero Δ breaks the symmetry of the local DOS, meaning that with increasing Δ, more states are localized at one site (here A for $\Delta < 0$) compared to the other lattice site within the unit cell. In the hBN structure, of course, nitrogen attracts more states than boron, since $\epsilon_N < \epsilon_B$. Our results qualitatively agree with published results obtained by DFT [55].

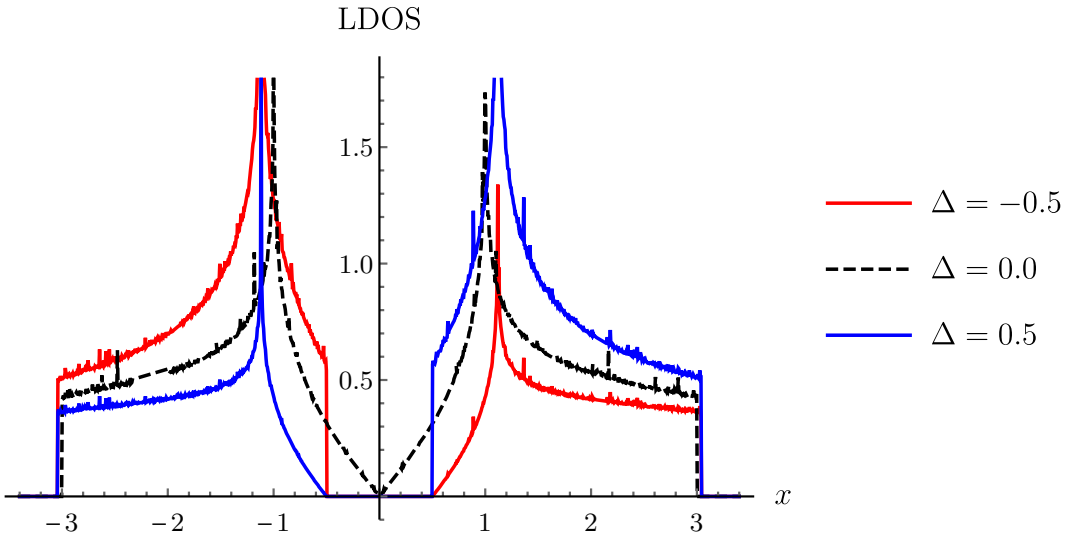

Figure 3.9: The local DOS plot (i.e. negative imaginary part of the diagonal Green's function g_{00}) for the asymetrical hexagonal lattice (e.g. hBN) evaluated numerically according to the Eq. 3.64 with various values of Δ in units of t.

3.4 Systems with a single impurity

In this section, we study the effects of an impurity introduced into a tight-binding system. In particular, we compute the relevant Green's functions and local densities of states to see how the electronic structure changes due to the presence of the impurity. Since the impurity is attached to a single site of one- or two-dimensional systems, we call the impurity an adsorbate.

Consider the simplest adsorbed impurity (e.g., hydrogen) represented by a single orbital with energy level ϵ_a containing a single electron that is connected[7] to a single substrate atom by the perturbation:

$$V = t\,|a\rangle\,\langle 0| + c.c.$$

In matrix representation, the perturbing potential is

$$V = \begin{pmatrix} 0 & t & 0 & \cdots \\ t^* & 0 & 0 & \cdots \\ 0 & 0 & \ddots & \cdots \\ \vdots & \vdots & \vdots & 0 \end{pmatrix}, \tag{3.66}$$

[7] Alternatively, for 2D systems, one can consider more than a single coupling, corresponding to different adatom positions. For example, there is a double coupling or the "bridge" position $V = t(|a\rangle\,\langle 0| + |a\rangle\,\langle 1|) + c.c.$

and the Green's function of the unperturbed Hamiltonian $\begin{pmatrix} \epsilon_a & 0 & \cdots \\ 0 & H_{11} & \cdots \\ \vdots & \vdots & \ddots \end{pmatrix}$ is

$$g = \begin{pmatrix} g_{aa} & 0 & 0 & \cdots \\ 0 & g_{00} & g_{10} & \cdots \\ 0 & g_{01} & g_{11} & \cdots \\ \vdots & \vdots & \vdots & \ddots \end{pmatrix}, \tag{3.67}$$

where the Green's function of the isolated adatom g_{aa} is[8] given by Eq. 2.35 as

$$g_{aa}(E) = \frac{1}{E - \epsilon_a + i\eta}.$$

Certainly for the potential V above it holds that $\det(1 - gV) = 1 - |t|^2 g_{aa} g_{00}$. Consequently one can show by matrix multiplication that Eq. 2.26 gives

$$T = V\frac{1}{1 - gV} = \frac{1}{1 - g_{aa}g_{00}|t|^2} \begin{pmatrix} -g_{00}|t|^2 & t & 0 & \cdots \\ t^* & -g_{aa}|t|^2 & 0 & \cdots \\ 0 & 0 & 0 & \cdots \\ \vdots & \vdots & \vdots & \ddots \end{pmatrix}.$$

We now seek to obtain the Green's function for the whole system, especially its matrix elements for the adatom G_{aa} and the substrate atoms G_{ii}. Utilizing the simple form of the matrix g in Eq. 3.67, a straightforward matrix multiplication $\Delta G = gTg$ gives

$$\Delta G_{aa} = \frac{g_{aa}^2 g_{00}|t|^2}{1 - g_{aa}g_{00}|t|^2} \tag{3.68}$$

and for $i = 0, 1, 2, ...$ we obtain

$$\Delta G_{ii} = \frac{g_{i0}^2 g_{aa}|t|^2}{1 - g_{aa}g_{00}|t|^2}. \tag{3.69}$$

In the following, we will apply these expressions to the one- and two-dimensional systems discussed in previous sections.

3.4.1 Linear tight-binding chains of identical atoms

A tight-binding Hamiltonian describing a system of a single atom coupled to a linear chain with nearest neighbor coupling (hopping parameter) τ and chain energy levels ϵ_0 has the form of a tridiagonal matrix

$$\begin{pmatrix} \epsilon_a & t & 0 & \cdots & 0 \\ t & \epsilon_0 & \tau & 0 & \vdots \\ 0 & \tau & \epsilon_0 & \tau & 0 \\ \vdots & \cdots & \tau & \ddots & \tau \\ 0 & \cdots & 0 & \tau & \epsilon_0 \end{pmatrix} = \begin{pmatrix} \epsilon_a & H_{1a} \\ H_{a1} & H_{11} \end{pmatrix}. \tag{3.70}$$

[8] In what follows, the limit of $\eta \to 0+$ is implicitly assumed, and sometimes even $i\eta$ itself will not be written.

From Chapter 2, we know that the full (retarded) Green's function for the adatom G_{aa} is given by simply adding the self-energy to the isolated adatom's Green's function, namely

$$G_{aa}(E) = \frac{1}{E + i\eta - \epsilon_a - \Sigma(E)} = \frac{1}{E + i\eta - \epsilon_a - H_{1a} g_{11} H_{1a}}, \tag{3.71}$$

with $\Sigma(E)$ being the self-energy and g_{11} the Green's function of the first atom of the chain. Also, we have $H_{1a} = H_{a1}^{\dagger}$.

Analytical expressions for g_{11} were found in Eq. 3.24 for a semi-infinite chain, and in Eq. 3.39 for a finite chain. By plugging in these expressions into Eq. 3.71, we obtain

$$G_{aa}(E) = \frac{1}{E + i\eta - \epsilon_a - \frac{t^2}{|\tau|}\left(x(E) - i\sqrt{1 - x(E)^2}\right)}, \tag{3.72}$$

for a semi-infinite chain and

$$G_{aa}(E) = \frac{1}{E + i\eta - \epsilon_a - \frac{t^2}{|\tau|}\left(\frac{\sin(N \arccos x(E))}{\sin((N+1) \arccos x(E))}\right)}, \tag{3.73}$$

for a finite chain. In our notation, $x = \frac{E + i\eta - \epsilon_0}{2|\tau|}$.

Now the (local) DOS for the adatom within the band $x \in (-1, 1)$ is

$$n_a(E) = -\frac{1}{\pi} \operatorname{Im} G_{aa}(E) = \frac{\sqrt{1 - x(E)^2}}{(E - \epsilon_a - \frac{t^2}{|\tau|} x(E))^2 + 1 - x(E)^2}, \tag{3.74}$$

where the Green's function for a semi-infinite chain was used for illustration purposes. The adatom DOS curves are plotted also for energies outside the band using a proper continuation of Green's functions and an imaginary parameter η for different parameters (see Figs. 3.10 and 3.11), which are discussed in detail below.

Depending on the strength of the adatom coupling t, the adatom DOS can take various forms. In Fig. 3.10, where we set $\epsilon_a = \epsilon_0$, we can first observe the semi-elliptical shape for the case of $t = \tau = -1$. This is the limit of a one-dimensional semi-infinite chain of identical atoms discussed in the preceding chapter. That is, it corresponds to a situation where we have extended the chain by one atom, leading to identical density of states.

Next, if $|t| < |\tau|$, so the adatom coupling is weaker than the substrate hopping, adatom DOS takes the shape of a high narrow Lorentzian peak centered at ϵ_a. In the limit of adatom coupling $t \to 0$, this corresponds to an isolated atomic level ϵ_a. Note that the broadening is due to the inclusion of a small imaginary $\eta = 10^{-4}$. For $\eta \to 0$ and $t \to 0$, this peak tends to a "delta function".

Furthermore, with increasing $|t| > |\tau|$, the adatom DOS decreases in the middle of the energy band and increases at the edges of the band. Note that the changing shape of the DOS curves proceeds in such a way that the area under the curve is preserved, i.e., $\int_{-1}^{1} n_a(x) dx = \text{const}$.

Note the occurrence of localized (split-off) energy levels outside the band for certain values of t or ϵ_a in both figures. In fact, in our model, at most two

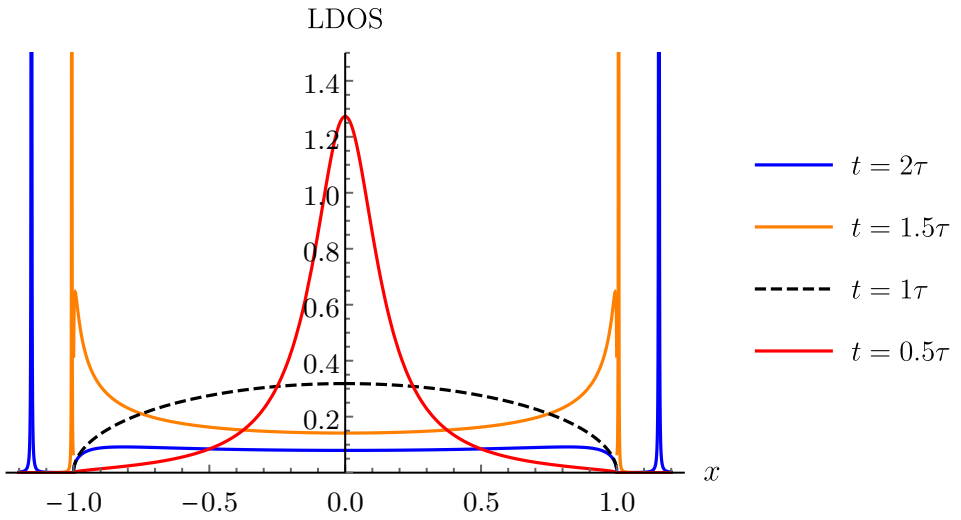

Figure 3.10: A plot of the adatom LDOS for a semi-infinite chain as a function of reduced energy x for various adatom couplings t. We used $\epsilon_a = \epsilon_0 = 0$, $\tau = -1$, $\eta = 10^{-4}$.

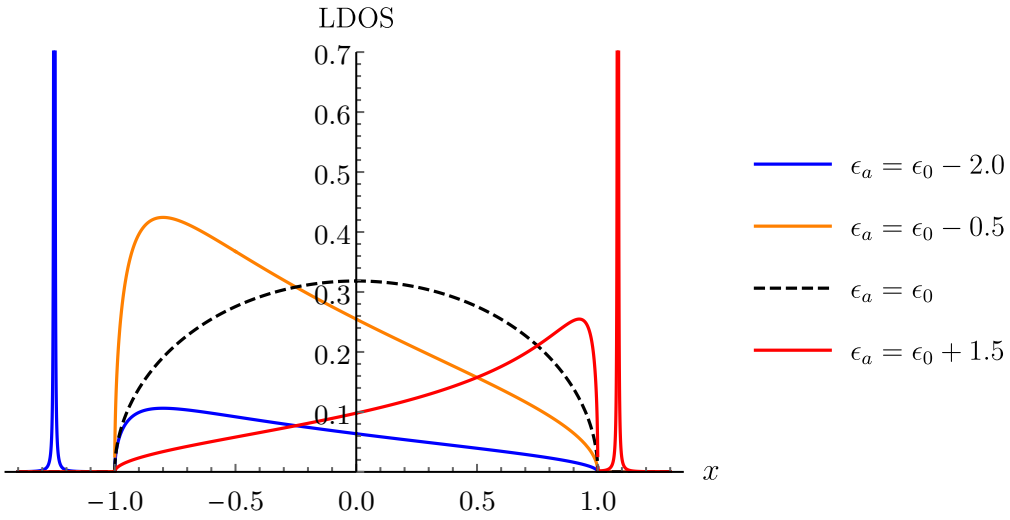

Figure 3.11: A plot of the adatom LDOS for a semi-infinite chain as a function of reduced energy x for various adatom energy levels ϵ_a. Also, $\epsilon_0 = 0$, $t = \tau = -1$, $\eta = 10^{-4}$.

localized states can appear: one above the band and one below.[9] These are given by zeros in the denominator of the Green's function in Eq. 3.72. If we denote by x_l the position of a localized state (its reduced energy), we write the condition

$$2\tau x_l - (\epsilon_a - \epsilon_0) - t^2 \operatorname{Re} g_{11}(x_l) = 0, \tag{3.75}$$

giving the position of the localized (split-off) state outside the band ($|x_l| > 1$) in general. From the properties of Green's functions we know that $|\operatorname{Re} g_{11}(x)|$ is monotonically decreasing outside the band as $|x|$ increases. In fact, the whole left hand side of Eq. 3.75 is a continuous and monotonic function of x for $|x| > 1$ (outside the band). Therefore, there can be at most one localized state, whose presence can be expected for large t. In fact, if we consider the Green's function in the asymptotic region $\operatorname{Re} g_{11}(x) \approx 1/x$ (as $x \to \infty$), we can rewrite the above equation as

$$x_l^2 - \frac{z_a}{2} x_l - \frac{t^2}{2|\tau|} = 0, \tag{3.76}$$

where we denoted $\frac{\epsilon_a - \epsilon_0}{|\tau|} = z_a$. This quadratic equation has solutions

$$x_l = \frac{z_a}{4} \pm \sqrt{\frac{z_a^2}{4} + \frac{2t^2}{|\tau|}}, \tag{3.77}$$

meaning that for $t \gg z_a$, $x_l \propto t$, i.e., the position of the localized state changes linearly with t.

We will now discuss the occurrence of localized states in the case of a semi-infinite chain. Inserting the Green's function for a semi-infinite chain into Eq. 3.75 gives

$$2|\tau| x_l - (\epsilon_a - \epsilon_0) - \frac{t^2}{|\tau|} \left(x_l - \operatorname{sgn} x_l \sqrt{x_l^2 - 1} \right) = 0. \tag{3.78}$$

In Fig. 3.10, the adatom DOS is presented for $\epsilon_a = \epsilon_0 = 0$. In this case localized states can occur once $2|\tau| x_l - \frac{t^2}{|\tau|} \left(x_l - \operatorname{sgn} x_l \sqrt{x_l^2 - 1} \right) = 0$, which reduces to $x_l^2 = \frac{(t/\tau)^4}{4((t/\tau)^2 - 1)}$. This function satisfies $x_l^2 \geq 1$ for $|t| > |\tau|$, which means we should see the localized states for $|t| > |\tau|$. And this is indeed observed.

Consider the case of $t = \tau = -1$ as in Fig. 3.11. Again we see that for $\epsilon_a = \epsilon_0$ we recover the LDOS of the semi-infinite chain. As ϵ_a increases from $\epsilon_0 - 2$ to $\epsilon_0 + 1.5$, the location of the maximum of the LDOS traverses the reduced spectrum from left to right (i.e., below to above the band). In case of $\epsilon_a = \epsilon_0 - 0.5$, no localized state exists and the area under the DOS curve attains its largest value within the band.

For $t = \tau$, the condition of Eq. 3.78 gives

$$x_l = \frac{z_a}{2} + \frac{1}{2 z_a}, \tag{3.79}$$

so for $x_l > 1$ (a state localized above the band) we must have necessarily $z_a > 1$. Similarly, if $x_l < -1$, then $z_a < -1$ must hold. This means that the energy

[9] These are also called surface states, due to their exponential localization on the surface atom (adatom), and also sometimes called bonding and antibonding due to similarities with chemical molecular orbital theory [44].

difference has to be larger than the coupling in the chain. For further discussion of these states, and how the values of the interaction parameters determine their occurrence and the character of the surface bond (metallic, ionic, etc.), see [56] and [57].

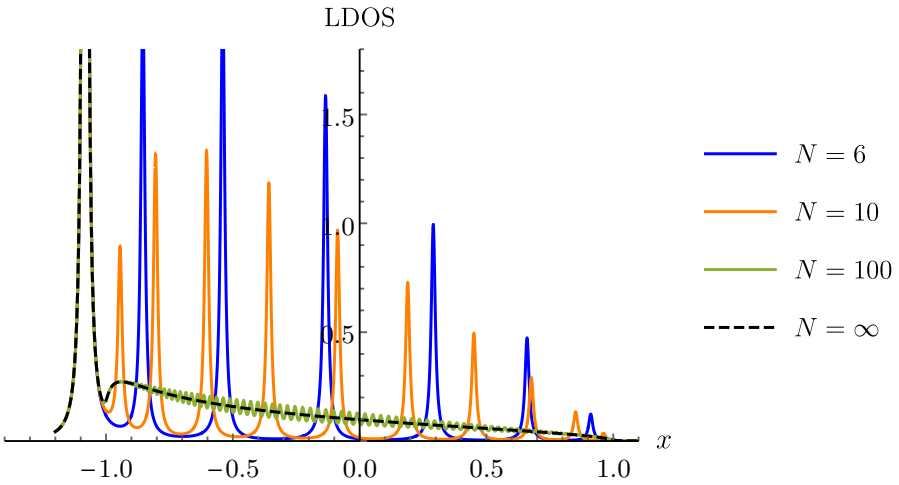

Figure 3.12: A plot of the adatom LDOS as a function of reduced energy x for linear chains of different lengths N. The peaks are broadened with the imaginary $\eta = 10^{-2}$. Other parameters are $\epsilon_a = -1.5$, $\epsilon_0 = 0$, $\tau = t = -1$.

Considering now finite chains of length N, i.e., Eq. 3.73, the shape of the LDOS converges towards the shape of the semi-infinite chain, however, this is only visible once η is large enough, see Fig. 3.12. For example, the LDOS for the $N = 100$ chain appears to be very similar to the case of a semi-infinite limit, but this is only due to the artificial broadening. Note that since $\epsilon_a = -1.5 < 0 = \epsilon_0$, a localized state appears below the band not only just for the semi-infinite chain but also for all finite chains shown in the figure. This state moves further from the band with increasing $|t|$.

As in the discussion above, the occurrence of localized states is given by poles of the Green's function. Analogously to the semi-infinite case, the finite chain of length N has N delocalized states in the energy band for $\epsilon_a - \epsilon_0 = 0$. As the parameter z_a increases above zero, the energies of the band states slightly increase until at $z_a = 1$ a surface state separates out of the band, leaving $N - 1$ states in the band. This exponentially localized state becomes more concentrated on the adatom as z_a further increases. A more detailed discussion of these states can be found in [44].

3.4.2 Embedding a finite linear chain

In the preceding section, we discussed the case of a single adatom coupled to a linear chain. This can be viewed as embedding a single atom in a linear chain, as we will now show. Subsequently, we will embed a finite chain with an adatom in another (in)finite chain and study the changes of adatom DOS as we add more "environment" atoms, in which our linear chain is embedded.

In general, we consider the following partitioning of the full system into part I and part II. The Hamiltonian matrix reads

$$\begin{pmatrix} E - H_{11} & -H_{12} \\ -H_{21} & E - H_{22} \end{pmatrix} = \begin{pmatrix} g_1^{-1} & -H_{12} \\ -H_{21} & g_2^{-1} \end{pmatrix} = \begin{pmatrix} G_{11} & G_{12} \\ G_{21} & G_{22} \end{pmatrix}^{-1}, \tag{3.80}$$

leading to the Green's function of part I

$$G_{11}(E) = [g_1^{-1} - H_{12} g_2 H_{21}]^{-1} = [g_1^{-1} - \Sigma(E)]^{-1}, \tag{3.81}$$

where we define the self-energy matrix (representing the effect of part II on part I) as

$$\Sigma(E) = H_{12} g_2 H_{21}. \tag{3.82}$$

Previously, we discussed a single adatom ϵ_a coupled to the substrate by a coupling t, meaning that $H_{11} = \epsilon_a$, $H_{12} = H_{21}^T = (t, 0, ...)$. The Green's function for the adatom ($G_{\text{aa}} = G_{11}$) was shown to have the following form:[10]

$$G_{11}(E) = \frac{1}{E - \epsilon_a - t^2 g_2^{(11)}}, \tag{3.83}$$

i.e., in this case, Σ is a number (not a matrix), and $g_2^{(11)}$ is the first element of the Green's function of part II.

Further, let us consider a two-level system of ϵ_a (adatom) and ϵ_0 (substrate atom) coupled together with t as the region I. Then $H_{11} = \begin{pmatrix} \epsilon_a & t \\ t & \epsilon_0 \end{pmatrix}$. If only the second atom is coupled to region II with parameter τ, then $H_{12} = H_{21}^T = \begin{pmatrix} 0 & 0 & ... \\ \tau & 0 & ... \end{pmatrix}$, and for the self-energy we obtain

$$\Sigma(E) = \begin{pmatrix} 0 & 0 \\ 0 & \tau^2 g_2^{(11)} \end{pmatrix}. \tag{3.84}$$

Then from Eq. 3.81 we obtain that the Green's function of the region I reads

$$\begin{aligned} G_{11} &= \begin{pmatrix} E - \epsilon_a & -t \\ -t & E - \epsilon_0 - \Sigma^{(22)}(E) \end{pmatrix}^{-1} = \\ &= \frac{1}{(E - \epsilon_a)(E - \epsilon_0 - \Sigma^{(22)}(E)) - t^2} \begin{pmatrix} E - \epsilon_0 - \Sigma^{(22)}(E) & t \\ t & E - \epsilon_a \end{pmatrix}. \end{aligned}$$

Therefore, Green's function of the adatom is $G_{aa} = \frac{1}{E - \epsilon_a - t^2 (E - \epsilon_0 - \Sigma^{(22)}(E))^{-1}}$. This amounts to terminating the continued fraction expansion of a Green's function (see Eq. 2.25) by the self-energy.

In general, we consider part I consisting of N atoms, one of which is the adatom. If we use the Green's function of the semi-infinite chain given in Eq. 3.24, we obtain for the only non-zero self-energy matrix element[11]

$$\Sigma_\infty(E) = |\tau| \Big(x - i\sqrt{1 - x^2} \Big). \tag{3.85}$$

[10] Here, superscripts refer to particular elements of matrices.

[11] From now on we denote by $\Sigma(E)$ the only non-zero element of self-energy matrix to simplify the notation.

While this is the exact expression and it is useful, we would also like to have a simplified, energy independent approximation of the self-energy to use in Schrödinger's equation. This can be done in several ways. First, using the definition of reduced energy $x|\tau| = (E - \epsilon_0)/2$, we can try to approximate $\Sigma(E)$ to remove its dependency on energy E as

$$\Sigma_\tau = -i|\tau|, \tag{3.86}$$

which becomes equal to $\Sigma_\infty(E)$ if $x = 0$, if we also assume $\epsilon_0 \neq 0$, we can write

$$\Sigma_{\text{approx.}} = -\frac{\epsilon_0}{2} - i\left(|\tau| - \frac{\epsilon_0^2}{8|\tau|}\right). \tag{3.87}$$

This expression is exact for $E = 0$ and should be less accurate for energies farther from zero.

We now calculate the LDOS for the adatom in a finite chain embedded in a semi-infinite chain. We account for the semi-infinite chain using the exact self-energy and the two approximations. Note that the adatom DOS curves are given (up to π) by the negative imaginary part of the first matrix element G_{aa} of the embedded Green's function

$$G_{\text{emb}}(E) = (E + i\eta - H_{\text{emb}})^{-1}, \tag{3.88}$$

where

$$H_{\text{emb}} = \begin{pmatrix} \epsilon_a & t & 0 & \cdots & 0 \\ t & \epsilon_0 & \tau & 0 & \vdots \\ 0 & \tau & \epsilon_0 & \tau & 0 \\ \vdots & \cdots & \tau & \ddots & \tau \\ 0 & \cdots & 0 & \tau & \epsilon_0 + \Sigma \end{pmatrix}. \tag{3.89}$$

Fig. 3.13 shows results for the embedding of a chain of length N (with the first atom being the adatom) in a semi-infinite chain. We show the negative imaginary parts of Green's functions regularized with imaginary η. Clearly, the approximations are only valid for certain energies. The real part of the self-energy $\operatorname{Re}\Sigma_{\text{approx.}} = -\frac{\epsilon_0}{2}$ shifts the states in the continuum band to the left (since in our example $\epsilon_0 > 0$) and this shift is greater for energies in the positive part of the reduced energy spectrum. The approximation of $\Sigma_\tau = -i|\tau|$ works well for $x \approx 0$ whereas $\Sigma_{\text{approx.}}$ curve lies close to the infinite limit in the vicinity of $x = -\epsilon_0/2|\tau| = -0.5$. In either case, the embedding gives the correct shape of the DOS, however, the broadening parameter η must be large enough to observe this. We note that for η large enough, all the curves coalesce. Nevertheless, the size of the peaks at a given η gives us some estimate how far the LDOS curve is from the semi-infinite limit.

Embedding a finite chain of N_1 atoms into another finite chain of length N_2 gives precisely the same adatom DOS as if we take the long chain of $N_1 + N_2$ atoms, as shown in Fig. 3.14 (compare curves denoted as Σ_{10} and $N = 17$). This eliminates the need to invert large matrices for the cost of adding an energy-dependent embedding potential (see Eq. 3.39)

$$\Sigma_N(E) = H_{12} g_2 H_{21} = |\tau| \left(\frac{\sin(N \arccos x(E))}{\sin((N+1)\arccos x(E))}\right), \tag{3.90}$$

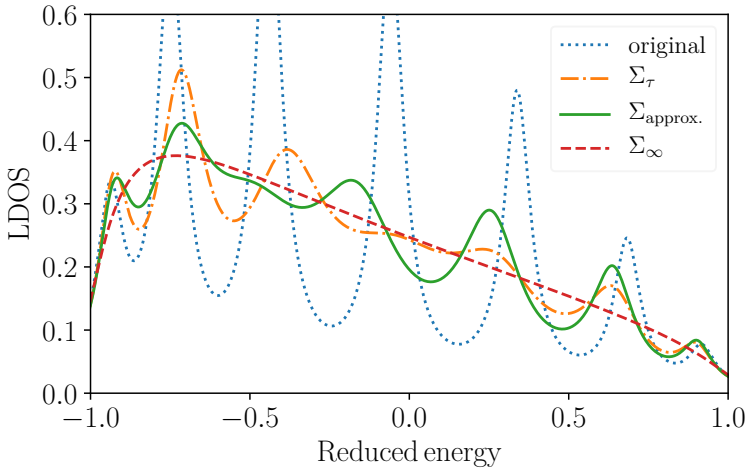

Figure 3.13: Adatom DoS for a chain of $N = 7$ atoms (first one of which is the adatom with energy $\epsilon_a = 0.5$ corresponding to the reduced energy of -0.25). Also, results for three embedding potentials Σ are shown. The substrate atoms have energy levels equal to $\epsilon_0 = 1$. Also, the broadening $\eta = 0.1$ and the coupling is the same throughout the whole chain $t = \tau$.

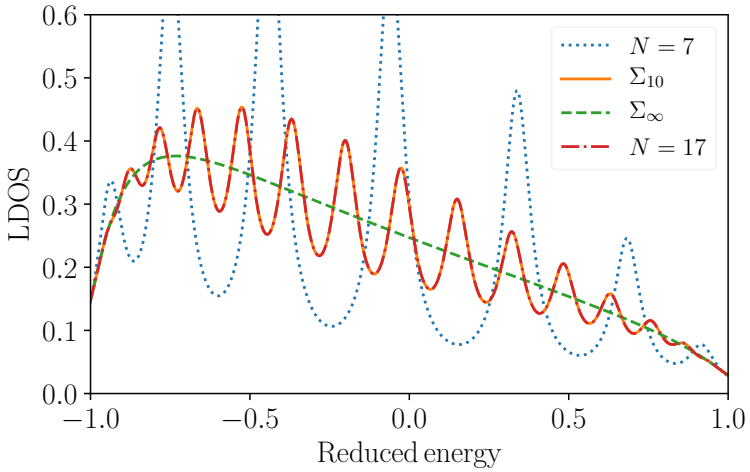

Figure 3.14: Adatom DoS for a chain of $N = 7$ atoms (first of which has energy $\epsilon_a = 0.5$) embedded in another chain of $N = 10$ atoms with levels $\epsilon_0 = 1$. Adatom DoS for a chain of $N = 17$ atoms is also shown for comparison. Σ_∞ is the semi-infinite chain limit. Here, $\epsilon_0 = 1$, $\eta = 0.1$ and the coupling is the same throughout the whole chain $t = \tau$.

with $x = (E + i\eta - \epsilon_0)/(2|\tau|)$. Even though in our example here we do not save any computational effort, this approach can sometimes be advantageous for large systems, e.g., if we only seek the Green's function or LDOS in some finite energy interval.

3.4.3 Diatomic tight-binding chains with realistic parameters

In this section, we proceed to a few more "realistic" cases of 1D tight-binding chains. We will discuss diatomic chains, as opposed to the chain of identical atoms in the preceding sections. The systems studied consist of a single adatom coupled to the substrate consisting of either boron and nitrogen atoms (BN) or magnesium and oxygen (MgO) atoms. The choice of these systems is motivated by their expected physical properties such as the presence of an energy gap in BN, and the ionic character of MgO bonds. We wish to elucidate the role of relative energy levels of neighbouring atoms in tight-binding systems with an emphasis on the adatom density of states (DOS).

As in the previous sections, we study finite systems in the LCAO tight-binding approximation, i.e., we work with one valence orbital for every atom of the 1D "solid" and parametrize the Hamiltonian with orbital energies on the diagonal and interatomic matrix elements (off-diagonal) between nearest-neighbor orbitals. In order to have a realistic estimate of the tight-binding parameters, we employ the model of Harrison [58]. He assumed that nearest neighbor hopping integrals are proportional to the inverse square of the bond length: $H_{\mathrm{mn}} = \eta_{\mathrm{mn}} \frac{h^2}{4\pi^2 m_e d^2}$, where the numerical factor η depends in general on the angular type of the atomic orbitals and the direction cosines of the vector that starts from the atom of the orbital m and ends at the atom of the orbital n. Namely, we use Harrison's values of η for hopping between s and p atomic orbitals: for σ bonds as $\eta_{s,s} = -1.32$, $\eta_{s,p} = 1.42$, $\eta_{p,p} = 2.22$, and for π bonds $\eta_{p,p,\pi} = -0.63$.

As we will later on study carbon structures as well, we discuss here both carbon and boron nitride models. We will assume a single p_z orbital per atom, forming a π band determining relevant electronic properties. Distances between the atoms are picked according to the nearest neighbor distances of two-dimensional analogs of graphene and hBN, namely 1.42 Å and 1.45 Å. For the carbon chains, we write $H_{\mathrm{mn}} = \eta_{p,p,\pi} \frac{h^2}{4\pi^2 m_e d^2} \approx -2.38$ eV, which is close to the usual value -2.7 eV, often found in literature [59]. For the boron nitride chain we get -2.28 eV when considering the Harrison's value of $\eta_{p,p,\pi}$. The orbital energies and hopping elements are in Tab. 3.1.

Table 3.1: Tight-binding parameters: Hartree-Fock orbital energies ϵ and nearest neighbor hopping values τ. All data are in eV and taken from Harrison [58].

	graphene	hBN		MgO	
	C	B	N	Mg	O
ϵ_s	–17.52	–12.54	–23.04	–6.86	–29.14
ϵ_p	–8.97	–6.64	–11.47	–2.99	–14.13
τ	–2.38 (p-p,π)	–2.28 (p-p,π)		±2.43 (s-p,σ)	

Our ionic MgO chain model consists of a diatomic chain of s and p orbitals connected by sigma bonds with a hopping parameter $\pm\tau$:

$$\begin{array}{cccccccccccc} \mathrm{O} & & \mathrm{O} & & \infty & & \mathrm{O} & & \infty & & \cdots \\ \epsilon_{ad} & t & \epsilon_s & \tau & \epsilon_p & -\tau & \epsilon_s & \tau & \epsilon_p & -\tau & \cdots \end{array}$$

In this case, we obtain for the hopping parameter from Harrison's model: $H_{\mathrm{mn}} = \eta_{s,p,\sigma}\frac{h^2}{4\pi^2 m_e d^2} \approx 2.43$ eV, which corresponds to the ionic bond length of 2.11 Å. Note, however, due to sp^2 hybridization, this is a poor estimate, and the value of 1.1 eV can be found in the literature [60].

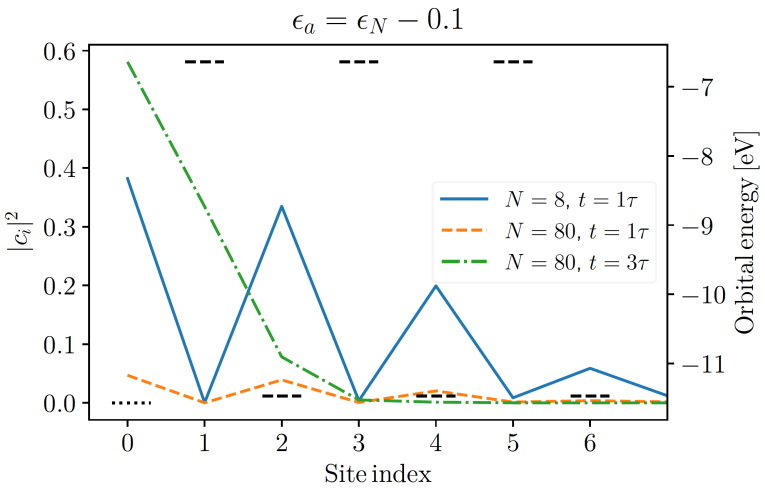

Figure 3.15: Ground state LCAO coefficients (squared) on specific atoms in the tight-binding chain of boron and nitrogen atoms of total length N. The adatom orbital energy is chosen to be $\epsilon_N - 0.1$ eV and two values of adatom coupling t are considered: weak $t = \tau$ and strong $t = 3\tau$.

In the preceding section concerning monatomic chains, we concluded that the localized states occur whenever the adatom level ϵ_a is sufficiently far from the center of the band and the adatom coupling t is large enough (see Eq. 3.75 and the succeeding discussion of some special cases). In case of the diatomic chains, the presence of a gap tends to decrease the total width of the continuum in DOS, as we know from Equation 3.26 and Fig. 3.3. Thus, more localized states can be expected in general as we will see in the following.

In Figs. 3.16 and 3.17, we observe a maximum of three localized states. This is because the gap opens space for the third localized state in addition to the two split-off states studied earlier (arising from the single adatom coupled to a single substrate atom). Interestingly, localized states are more likely to form if the adatom level is close to the energy level of the first atom of the chain, to which it is coupled. In other words, the difference between ϵ_{a} and the energy of the first substrate atom ϵ_1 plays a big role in the occurrence of the localized state.

We now start the discussion of the dependence of the LDOS on the different parameters of the model. We first present the results for the BN chain. We set-up the model so that the chain ends with a B atom and the adatom is attached to it. Fig. 3.15 presents squared LCAO coefficients $|c_i|^2$ on each atom of the BN

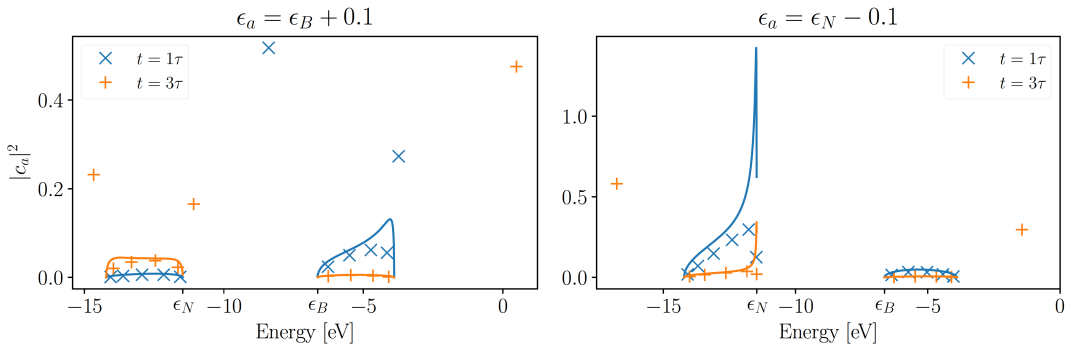

Figure 3.16: Adatom DOS for a BN chain of $N = 11$ atoms including a single adatom. The adatom orbital energy is chosen to be either $\epsilon_B + 0.1$ eV (left) or $\epsilon_N - 0.1$ eV (right) and two values of adatom coupling t are considered: weak $t = \tau$ and strong $t = 3\tau$. Lines represent infinite limits computed analytically for band energies. Here, $\eta = 10^{-3}$.

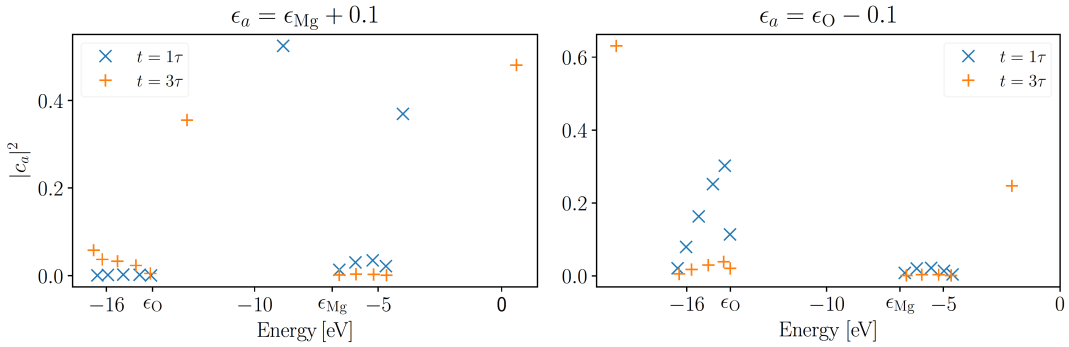

Figure 3.17: Adatom DOS for an MgO chain of $N = 11$ atoms including a single adatom. The adatom orbital energy is chosen to be either $\epsilon_{\mathrm{Mg}} + 0.1$ eV (left) or $\epsilon_O - 0.1$ eV (right) and two values of adatom coupling t are considered: weak $t = \tau$ and strong $t = 3\tau$. Here, $\eta = 10^{-3}$.

chain, starting with 0 as the adatom and 1 as a B atom, for the state with the largest value of the adatom LCAO coefficient $|c_a|^2$. We set the energy of the adatom to $\epsilon_a = \epsilon_N - 0.1$. This means that for $t = \tau$ the chain behaves almost as unperturbed. In this case, clearly, there is a partial localization due to the small offset of ϵ_a from ϵ_N and the c_0 coefficient decreases with increasing length of the chain. On the other hand, for stronger coupling $t = 3\tau$, there is a localized state characterized by the exponential decay, which is not affected by the length of the chain. This feature was already seen in adatom DOS of Fig. 3.12 where we saw that the position of a localized state is the same for finite N and for the infinite limit, whereas energies of delocalized states change within the band.

We now turn to the dependence of the adatom LDOS on the coupling. For BN we consider two cases. First, the energy of the adatom close to to boron energy ($\epsilon_a = \epsilon_B + 0.1$) and second, the adatom energy close to the nitrogen energy level ($\epsilon_a = \epsilon_N - 0.1$). In each case, the chain starts with a boron atom. The results are

shown in Fig. 3.16 (left for the first case and right for the second one). We can see that the N case with weak coupling does not produce any localized states (this is also visible in Fig. 3.15) and the LDOS follows the shape of the infinite limit computed analytically for band energies. With strong coupling, two localized states emerge. However, in the B case there are two localized states even with the weak coupling, and with strong coupling, there are already three of them. For the adatom energy close to the B atom energy, there is a strong interaction between the adatom and the first atom and the split-off states appear already for weak coupling. Finally, we note that the LDOS is similar to the infinite limit already for $N = 11$.

In case of the MgO chain, starting with the Mg atom, we observe similar behavior as for the BN system (see Fig. 3.17). There is a small difference in the behavior for the stronger coupling: when the adatom energy is close to the Mg level, the lowest-lying localized state is weaker (i.e., has a smaller $|c_a|^2$ coefficient) compared to the BN case and the localized state in the energy gap is accordingly stronger (compared to the BN system). Apart from this minute difference, the LDOS are very similar in both cases of diatomic tight-binding chains.

3.4.4 2D finite tight-binding models

In this section, we study tight-binding models with a single atom coupled to one (or more) atom(s) of a two-dimensional substrate. As in the previous section, we use realistic tight-binding parameters (orbital energies and hopping elements), as summarized in Tab. 3.1, with only nearest-neighbour coupling. We restrict ourselves to the case of a hexagonal lattice. For example, in the so-called top adatom position, we couple the adatom to a single substrate atom, which is then coupled to its three nearest neighbours. These are then coupled each to their two nearest neighbours, etc. Clearly, compared to the 1D finite chain case, now the (orbital) matrix representation of the tight-binding Hamiltonian does not have a simple tridiagonal form. We want to understand new features in the adatom DOS, compared to the 1D model, as we add more atoms into our system. We only study systems with up to $N = 38$ atoms.

Adatom DOS for 2D finite model of graphene with an adatom in the top position is shown in Figs. 3.18 and 3.19 for the weak and strong coupling, respectively. We show the data for models of different size as well as the infinite limit. Clearly, we can observe that the finite models' results tend to follow the LDOS shape of the infinite graphene sheet limit calculated calculated analytically according to Eq. C.5. However, we cannot say that there is clear convergence towards the infinite limit with increasing size of the finite model N, since even for the largest $N = 38$, there is still a considerable amount of the datapoints sitting far from the $N = \infty$ curve. These differences are most probably due to the atoms at the edges of our tight-binding models, which are only coupled to one or two neighbouring atoms within our model. The fraction of these "edge" atoms is decreasing very slowly. The position and strength of two localized states (one below and one above the band) for $t = 3\tau$ seems to converge quickly with system size, although slower compared to the 1D chain. In particular, the position of the state below the band agrees with the infinite limit to within 10^{-1} reduced energy units $(E - \epsilon_C)/|\tau|$ for $N = 5$, and to within $3 \cdot 10^{-3}$ for $N = 20$, and lastly to

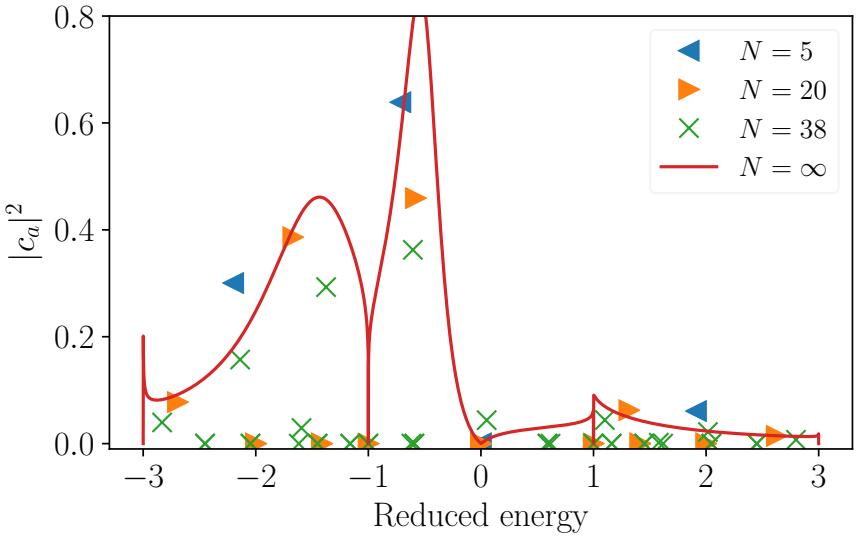

Figure 3.18: Adatom DOS for 2D models of graphene with an adatom with reduced energy of -1 in the top position. The adatom-substrate coupling is equal to $t = \tau$. The limit of $N = \infty$ is calculated analytically. N is the total number of atoms in the system.

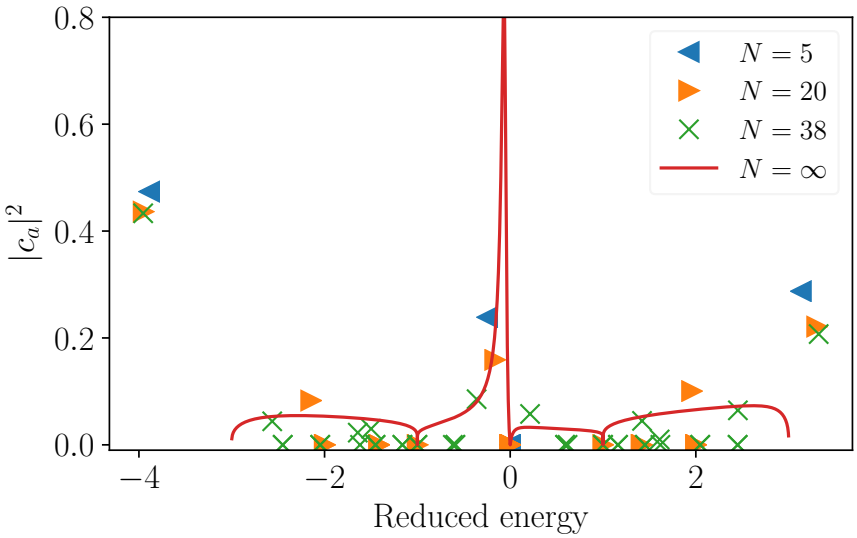

Figure 3.19: Adatom DOS for 2D models of graphene with an adatom with reduced energy of -1 in the top position. The adatom-substrate coupling is equal to $t = 3\tau$. The limit of $N = \infty$ is calculated analytically. N is the total number of atoms in the system.

within $3 \cdot 10^{-4}$ for $N = 38$.

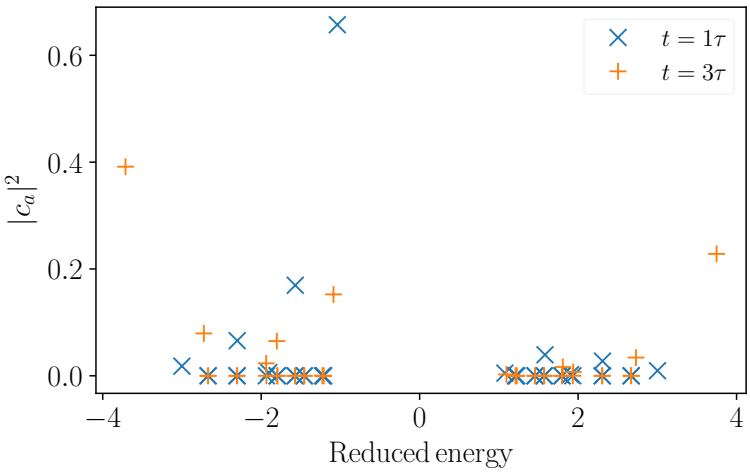

Figure 3.20: Adatom DOS for 2D finite models of hBN with the adatom in the top position. The adatom's reduced energy is -1. The total number of atoms is $N = 38$.

If we compare to the case of the hBN substrate in Fig. 3.20, we immediately notice the presence of the energy gap, which facilitates the formation of another localized state within the gap, thus preventing further interaction with continuum (band) states. However, notice that in the case of strong coupling $t = 3\tau$, the LDOS of both graphene and hBN are very similar in our model, including the positions and strengths of the localized states below and above the band. We note that no analytical result is available for the hBN case.

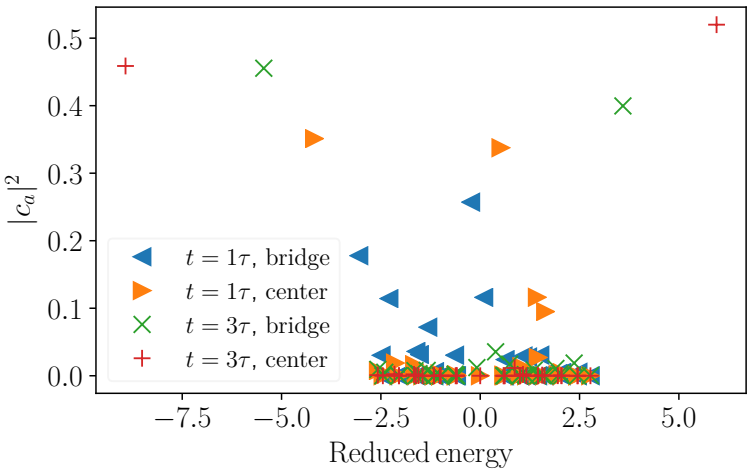

Figure 3.21: Adatom DOS for 2D finite models of graphene with different adatom positions. The adatom's reduced energy is -1. The adatom-substrate coupling is indicated in the figure. The total number of atoms is $N = 38$.

In Fig. 3.21, the adatom LDOS is plotted for graphene models with an adatom in bridge (coupling with two substrate atoms), and center (coupling with 6 substrate atoms) positions again for two strengths of coupling. Clearly the more substrate atoms to couple with, the further away from the band a localized state is formed. Moreover, we note that in the case of the center position there is a localized state already for weaker coupling $t = \tau$. Comparing with the LDOS for the top position (Fig. 3.18) the adatom seems to interact more with the continuum states, i.e., there are more states with nonzero c_a coefficients within the band when the adatom is coupled to more substrate atoms.

3.4.5 Adsorption energies and electron occupancies

In this section, we calculate "integral"[12] properties of one- and two-dimensional substrates with adatoms. Namely, we compute the electron occupancy of the adsorbed atom, and the adsorption energy, i.e., the difference of total energies of a coupled substrate and adsorbate system and the uncoupled system (i.e. with zero adatom hopping parameter t). Even though in reality this quantity is defined thermodynamically and includes various contributions, we consider here only the electronic energy contribution.

The adatom occupancy N_a is given as an integral over the adatom density of states up to the maximally occupied energy level E_F (see Eq. 2.34). To express the change in occupancy of the adatom ΔN_a, we use Eq. 3.68 and write

$$\Delta N_a = -\frac{2}{\pi}\,\mathrm{Im}\int_{-\infty}^{E_F} dE \Delta G_{aa} = -\frac{2}{\pi}\,\mathrm{Im}\int_{-\infty}^{E_F} dE \frac{g_{aa}^2 g_{00}|t|^2}{1 - g_{aa}g_{00}|t|^2}. \tag{3.91}$$

We note that we assume that a level can be doubly occupied. Also, g_{aa} and g_{00} are Green's functions of the isolated adatom and the first substrate atom, respectively. Upon adsorption, the Green's function of the adatom changes by $\Delta G_{aa} = G_{aa} - g_{aa}$. From Eq. 2.46 we obtain for the adsorption energy

$$E_{\mathrm{ads}} = (2\theta(E_F - \epsilon_a) - 1)\epsilon_a + \frac{2}{\pi}\,\mathrm{Im}\int_{-\infty}^{E_F} \log\Big(1 - g_{00}g_{aa}t^2\Big) dE. \tag{3.92}$$

We found that these integrals are not well suited for numerical calculations and it is necessary to undertake further steps to transform them into more numerically stable forms. The integrals are manipulated by methods of contour integration in the complex plane (see Appendix D for the derivation) to obtain the following forms suitable for numerical calculations

$$N_a = 1 + \frac{2}{\pi}\,\mathrm{Re}\int_0^1 ds \frac{1+\eta}{s^2} G_{aa}\left(E_F + i\frac{1+\eta-s}{s}\right), \tag{3.93}$$

for the electron occupancy on the adatom, and

$$E_{\mathrm{ads}} = -|\epsilon_a| - \frac{2}{\pi}\,\mathrm{Re}\int_0^1 ds \frac{1+\eta}{s^2} \log\Big(1 - g_{00}(z(s))g_{aa}(z(s))t^2\Big), \tag{3.94}$$

for the adsorption energy. Here, $z(s) = E_F + i\frac{1+\eta-s}{s}$.

In this section, we assume that before the adsorption, the adatom level ϵ_a is singly occupied, and after the adsorption, it is doubly occupied if $E_F = 0 > \epsilon_a$ and

[12] Meaning that they are given as integrals of Green's functions.

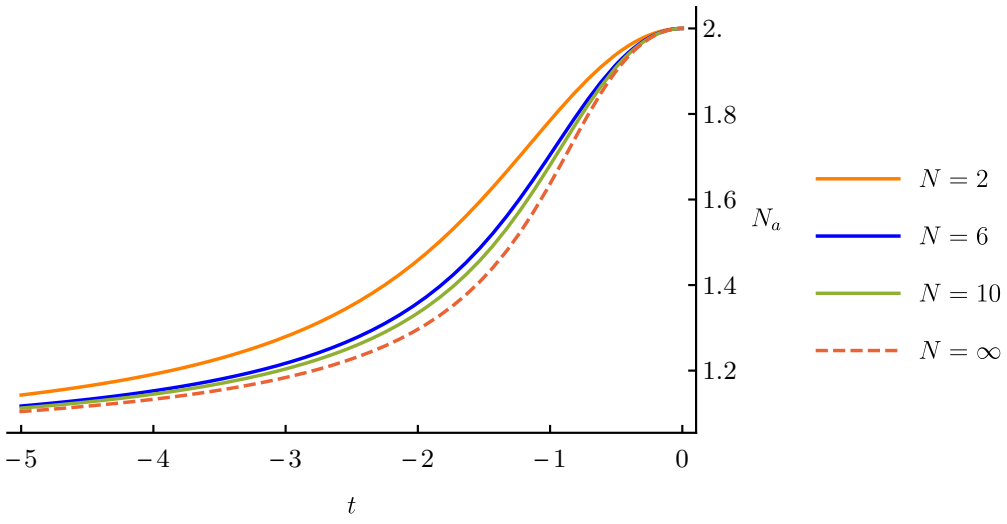

Figure 3.22: Adatom occupancy N_a for finite 1D chains as a function of the coupling parameter t for $\epsilon_a = -1$ computed numerically according to Eq. 3.93. Note the semi-infinite chain limit (dashed line). Also, $|\tau| = 1$, $\epsilon_0 = E_F = 0$, and $\eta = 10^{-6}$.

not occupied otherwise. Furthermore, we will mostly consider the case of half-filled energy band ($E_F = 0$) since this choice maximizes the adsorption energy in our model, as we show later on. There is no adsorption energy (difference in energy from the unperturbed case) for $E_F \to \infty$, even though individual levels may shift.[13] This follows from the fact that the perturbing potential V is purely off diagonal in the site representation, i.e., we have $\mathrm{Tr}\, H = \mathrm{Tr}\, H_0$.

In Fig. 3.22, the electron occupancy N_a of a single adatom connected to various finite and semi-infinite chains is shown as a function of the adatom coupling t. The adatom energy level is lower than the maximally occupied level of the substrate, $\epsilon_a = -1 < E_F$, therefore the physical intuition dictates to expect higher electron occupancy. Indeed, in the limit of the adatom coupling $|t| \to 0$, the occupancy $N_a \to 2$, corresponding to an isolated orbital that can accommodate a maximum of two electrons. On the other hand, in the limit of $t \to \infty$, $N_a \to 1$ with the convergence being faster with increasing length of the chain N. In other words, the adatom occupancy decreases with increasing length for fixed t.

[13] For E_F sufficiently large, the interaction energy between the adatom and the substrate vanishes (compare with Fig. 3.26). To show this, we manipulate the integral above using per-partes:

$$E_{\mathrm{ads}} = \frac{-2}{\pi}\left[E\,\mathrm{Im}\ln\left(1 - t^2 g_{aa} g_{00}\right)\right]_{-\infty}^{E_F} - \\ - \frac{2}{\pi}\,\mathrm{Im}\int_{-\infty}^{E_F} E\left(t^2 g_{00}(E) g_{aa}^2(E) + t^2 g_{aa}(E) g_{00}^2(E)\right)\frac{dE}{(1 - t^2 g_{aa} g_{00})}.$$

In this expression, the surface term vanishes since for any energy outside the band, the argument of Log is real, the second term can be transformed into a contour integral that can be closed in the lower half-plane of the energy plane, where no poles are present. Since the integrand approaches $1/E^2$ asymptotically (because $g(E) \sim 1/E$), the semicircular path vanishes and the integral is zero [40].

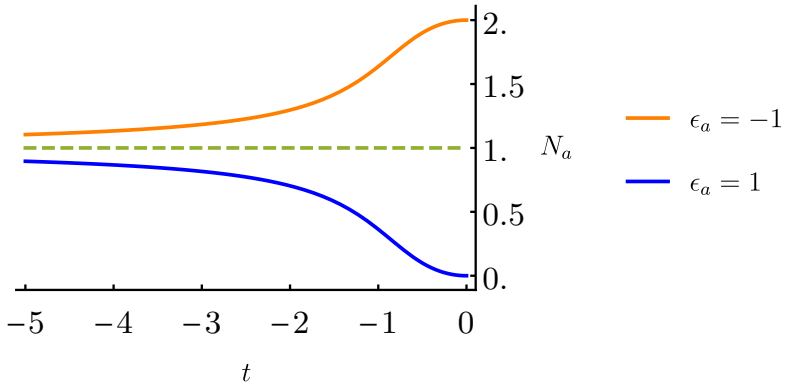

Figure 3.23: Adatom occupancy N_a on a 1D semi-infinite chain as a function of the coupling parameter t for $\epsilon_a = \pm 1$ computed numerically according to Eq. 3.93. Also, $\tau = -1$, $E_F = 0$, and $\eta = 10^{-6}$.

Let us now compare with the case of the adatom level above the filled part of the band, i.e., $\epsilon_a = 1 > E_F$, as shown in Fig. 3.23 for the half-filled semi-infinite chain of atoms with orbital levels $\epsilon_0 = 0$. Clearly, the two cases of $\epsilon_a = \pm 1$ are symmetric, i.e., the occupancy N_a decreases with $|t|$ and eventually goes to 0 for $|t| \to 0$ if $\epsilon_a > \epsilon_0$. Furthermore, note that for $|t| \to \infty$, N_a goes to 1 for both $\epsilon_a = \pm 1$. In fact, this is the case for any ϵ_a since, with increasing t, the imaginary part of the adatom's Green's function goes to zero for energies within the band and the only contribution to its integral N_a is given by a localized state below the band, which appears regardless of the value of ϵ_a for t sufficiently large.

In Fig. 3.24, we plot the adatom occupancy N_a as a function of both the adatom coupling t and the adatom energy level ϵ_a for a half-filled semi-infinite chain. Besides the already discussed increase (decrease) in the occupation of the adatom site if the adatom level ϵ_a is below (above) the substrate Fermi level $E_F = 0$, there is no change in the adatom occupancy for varying t if the adatom and substrate orbital levels coincide, i.e., $\epsilon_a = \epsilon_0$, in accordance with physical intuition.

The adsorption energies of a single atom connected to a linear chain are linear with respect to the adatom coupling t for large $|t| > |\tau|$ (compare Fig. 3.25). This can be understood from the behavior of the integrand in Eq. 3.92 by noting that $\operatorname{Im} \log z = \arg z = \arctan \frac{\operatorname{Re} z}{\operatorname{Im} z}$. In our case, $z = 1 - g_{00} g_{aa} t^2$ and it is easy to show that for t large, the arctangent approaches a constant with respect to t. However, as we integrate from $-\infty$, clearly, for the integral to be convergent, the constant must be zero for sufficiently negative energies. However, we must take into account the effect of a possible localized state lying below the band, which is expected to appear, as we have shown earlier, for large t. In fact, between the localized state and the bottom of the band, the integrand is a non-zero constant [40]. Therefore, since the localized state is linear in t, as we showed in Eq. 3.77, also the $E_{\text{ads}} \propto t$ for large t.

Similarly, for t small, the integrand behaves as $\arctan t^2 \approx t^2$, i.e., the adsorption energy is quadratic in t. This behaviour is also visible in Fig. 3.25. Also, one can notice that there is not much variation with respect to the length of the chain N. This gives us hope that we can expect quite fast convergence with respect to

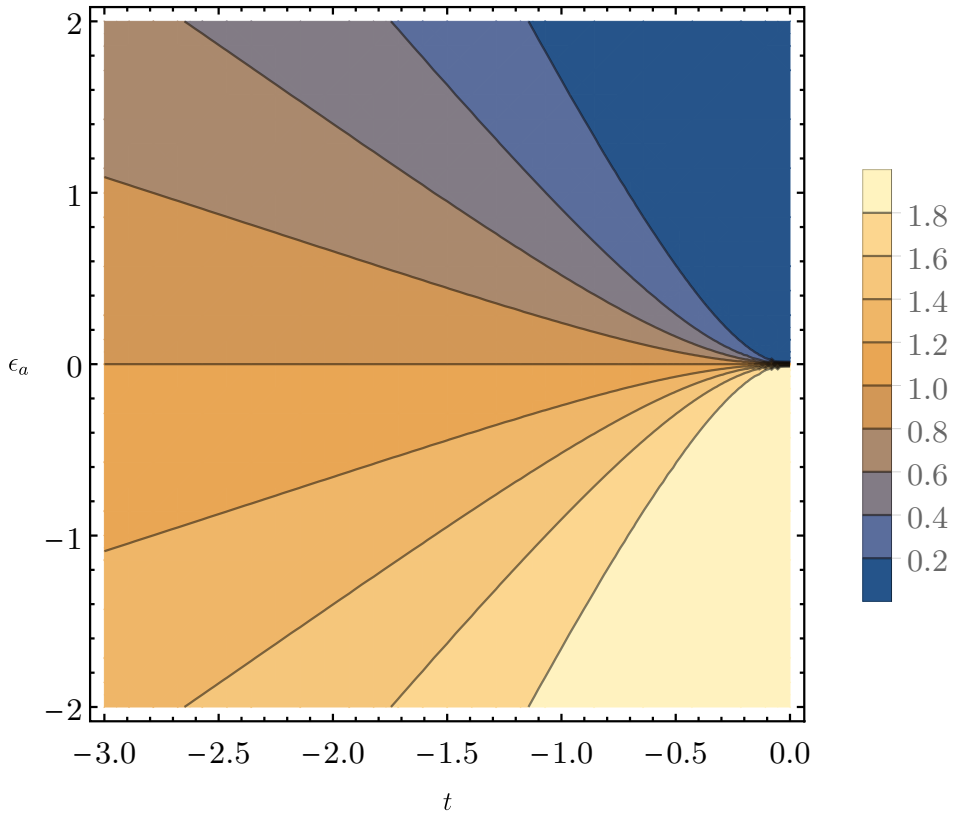

Figure 3.24: Contour plot of the adatom occupancy N_a in the parameter space of ϵ_a and the coupling parameter t for a 1D semi-infinite chain computed numerically according to Eq. 3.93. Here, we set $\tau = -1$, $E_F = 0$, $\eta = 10^{-6}$.

the size of the system also in the case of more realistic models.

It is interesting to calculate E_{ads} as a function of E_F, i.e., filling of the band of the chain. In Fig. 3.26, we can see the convergence of the "step" plots for increasing N towards an inverted triangle structure with the triangle vertex located at $E_F = \epsilon_a$. In essence, $|E_{\text{ads}}|$ is maximum when $E_F = \epsilon_a$. In this case, upon switching the interaction the maximum number of electrons have their energies lowered and only a few electrons having their energies raised. In other words, the adatom level is broadened by the interaction with the substrate. When it is half-filled, electrons take most advantage of this broadening. The adsorption energy then decreases linearly until it vanishes at the top of the band. This is tentatively similar to the d-band model predicting trends in adsorption energies of small adsorbates on transition metal surfaces based on the d-band filling [61].

A contour plot of the adsorption energy is plotted in the ϵ_a, t parameter space in Fig. 3.27) for the case of semi-infinite linear substrate. We can observe that the E_{ads} is even with respect to ϵ_a due to the fact that the Green's function $g_{00}(z)$ is purely imaginary for imaginary z. Also, E_{ads} is always negative due to the presence of the term $-|\epsilon_a|$ in Eq. 3.94, and it decreases with increasing coupling strength $|t|$.

Let us now proceed to the case of a two-dimensional substrate. To evaluate adatom occupancies and adsorption energies for the case of the 2D hexagonal

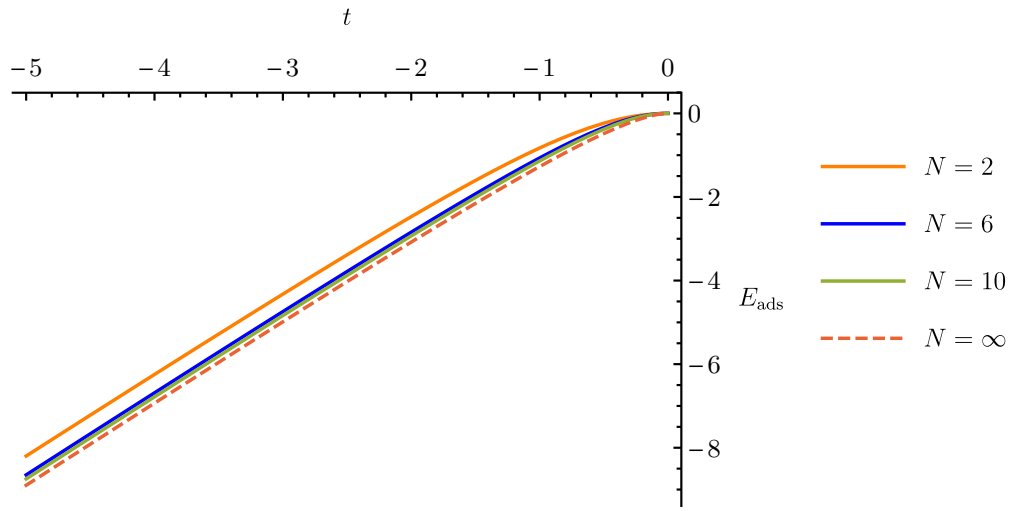

Figure 3.25: Adsorption energy E_{ads} as a function of the coupling parameter t for various linear chain substrates computed according to Eq. 3.94. Here, we set $\tau = -1$, $\epsilon_a = 0 = \epsilon_0 = E_F$, $\eta = 10^{-6}$.

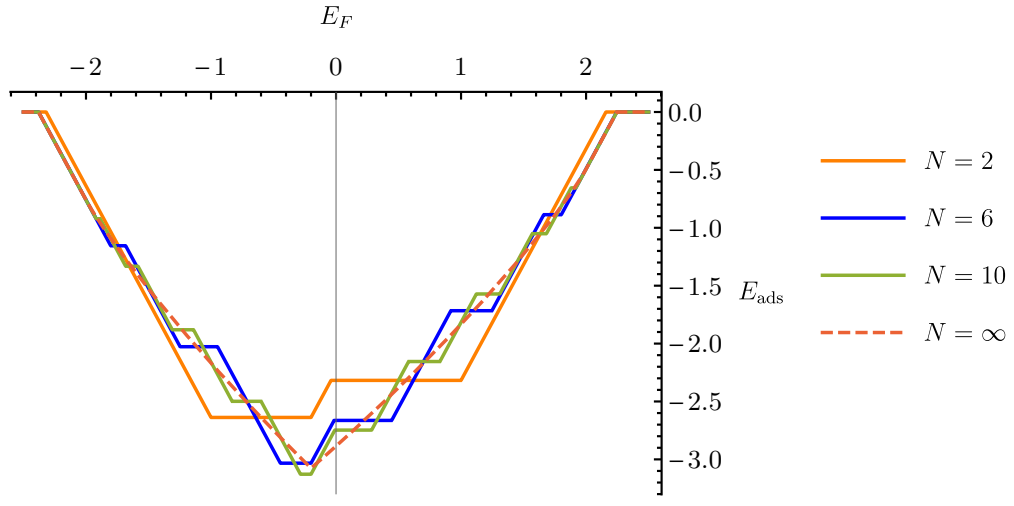

Figure 3.26: Adsorption energy E_{ads} as a function of E_F for the coupling parameter $t = -1.5$ for a various linear chain substrates computed according to Eq. 3.94. Here, we set $\tau = -1$, $\epsilon_a = -0.1$, $\eta = 10^{-6}$.

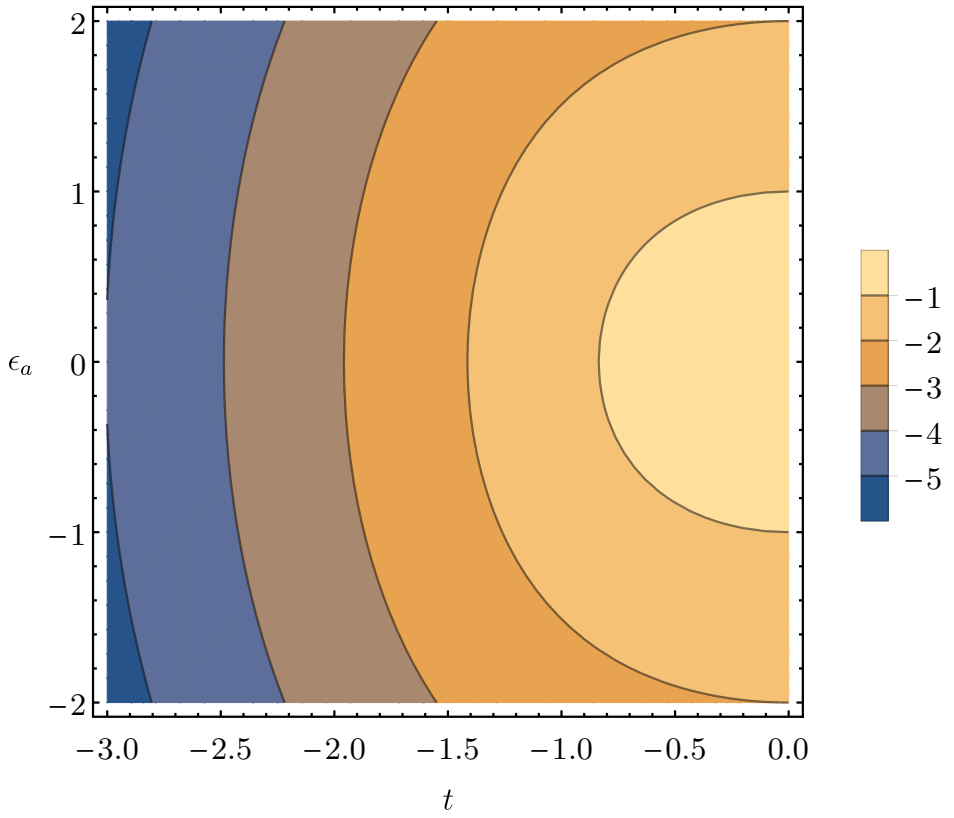

Figure 3.27: Contour plot of the adsorption energy E_{ads} as a function of ϵ_a and the coupling parameter t for a 1D semi-infinite chain computed according to Eq. 3.94. Here, substrate coupling $\tau = -1$, $E_F = 0$, $\eta = 10^{-6}$.

(graphene) substrate, we use the diagonal Green's function expressed in terms of complete elliptic integrals of the first kind as described in Appendix C. However, various numerical problems arise when computing integrals above, due to the discontinuities in the Green's functions which survive even after the analytic continuation into the complex plane.

The adatom occupancy as a function of the adatom energy level ϵ_a and the coupling t is shown in Fig. 3.28. The adatom is in the atop (t) position, coupling only to the nearest substrate atom. Compared to the 1D semi-infinite chain, the occupancy changes more abruptly nearby $\epsilon_a = 0 = E_F$ for a given coupling t. These jumps in the occupancy can be seen in the plot as zigzag lines. On the other hand, we can also observe that as we fix $\epsilon_a \neq 0$ and increase t towards ∞, N_a converges towards 1 slower than in the case of the 1D chain.

The plot of adsorption energy shows some differences compared to the case of the linear chain (see Fig. 3.29 for the case of $\epsilon_a = 0 = E_F$). In particular, note that the linear regime starts earlier (i.e., for a smaller coupling t) in the case of the 1D chain. In fact, E_{ads} of an adatom on graphene starts to move away from 0 only once the adatom coupling is similar to the substrate coupling $t \approx \tau$. The adsorption energy of an atom on graphene as a function of both the adatom energy level ϵ_a and the coupling t is shown in Fig. 3.30. Clearly, for $t = 0$, the E_{ads} is symmetric with respect to ϵ_a, as it should be. With increasing

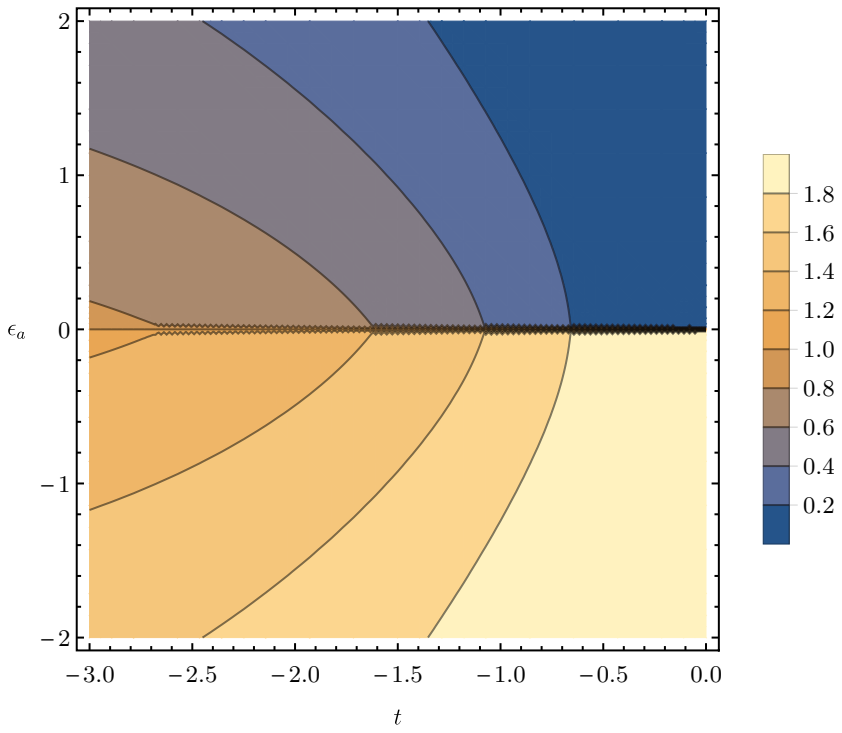

Figure 3.28: Adatom occupancy N_a as a function of ϵ_a and the coupling parameter t for a hexagonal sheet of graphene. Here, the substrate coupling $\tau = -1$, $E_F = 0$, $\eta = 10^{-5}$.

coupling strength $|t|$, an asymmetry with respect to ϵ_a develops. In particular, E_{ads} decreases with decreasing adatom energy ϵ_a. This can be partly attributed to the specific form of the LDOS, which includes discontinuities and a singularity (see Fig. 3.19). Note that the constant term in our prescription for E_{ads} (see Eq. 3.94), for $\epsilon_a > 0$, causes E_{ads} to first increase with t and then decrease.

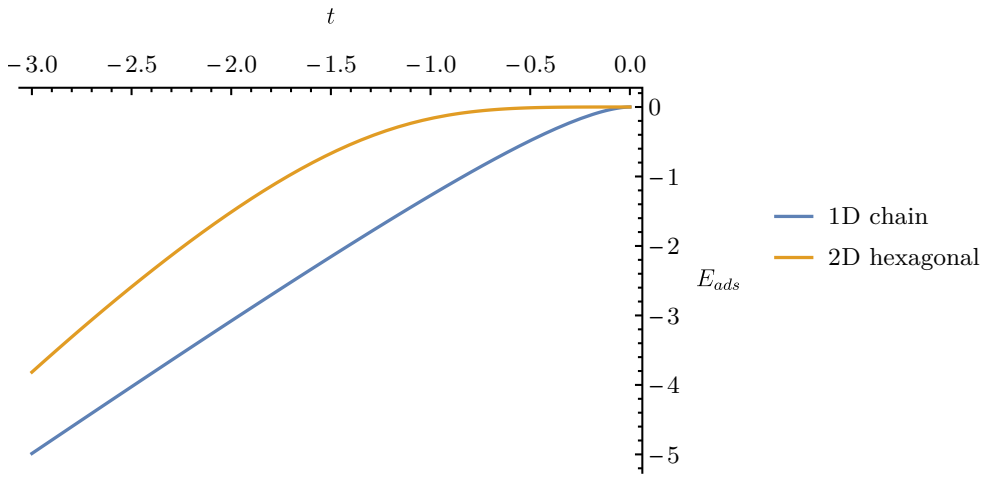

Figure 3.29: Adsorption energy E_{ads} as a function of the adatom coupling parameter t for 1D chain and a hexagonal sheet of graphene. The other parameters are $\epsilon_a = 0$, $\tau = -1$, $E_F = 0$, $\eta = 10^{-6}$.

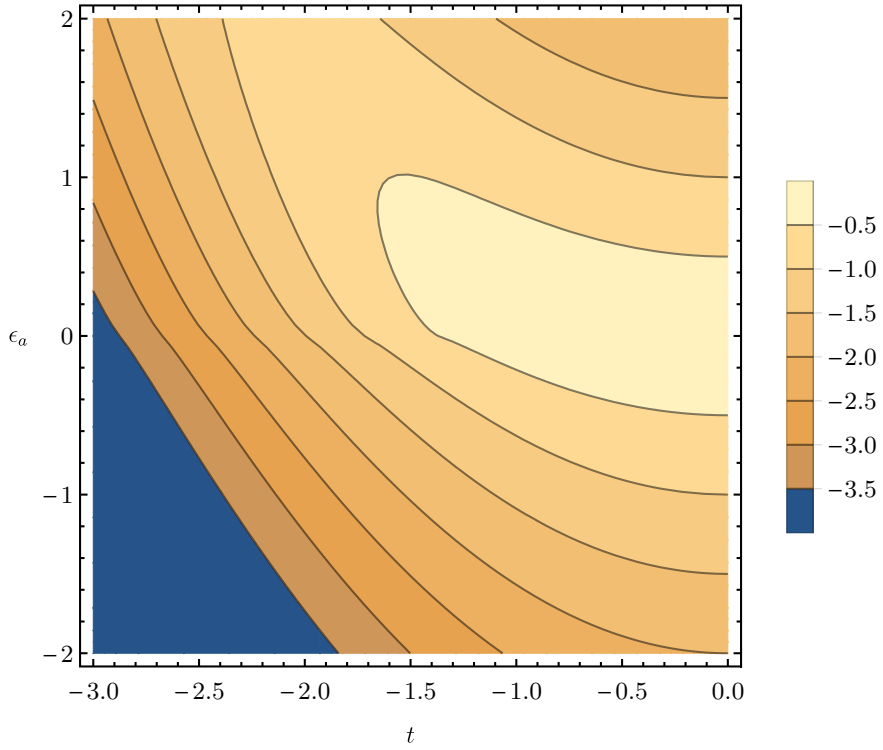

Figure 3.30: Adsorption energy E_{ads} as a function of ϵ_a and the coupling parameter t for a hexagonal sheet of graphene. Here, the substrate is 2D honeycomb lattice with coupling $\tau = -1$, $E_F = 0$, $\eta = 10^{-6}$.

4. Ab initio calculations

In this chapter, we study the convergence of the adsorption energy of small closed-shell atoms and molecules on different substrates and their models of increasing size. Furthermore we analyze how the convergence is affected by the subtractive embedding scheme.

The adsorption energy is the interaction energy of the substrate and the adsorbate

$$\Delta E = E_{\text{total}} - E_{\text{substrate}} - E_{\text{adsorbate}}, \tag{4.1}$$

where the energies refer to internal electronic energies. We set the temperature to zero and do not consider quantum nuclear effects.

There are two main approaches how to treat adsorption on solid surfaces using the methods of quantum chemistry. First, periodic boundary conditions can be applied so that the system is treated as effectively infinite. This is beneficial if adsorption of a molecular overlayer is studied but less efficient when one is interested in an adsorption of a single molecule. The second approach takes a finite cluster from the surface and treats the surface as a big molecule. This is guided by the idea that bonding on surfaces is a local process.[1] The critical issue in this case is the convergence of adsorption energy with the cluster size.

In this chapter, we consider adsorption of neon and hydrogen fluoride on graphene and hexagonal boron nitride surfaces. Apart from treating the surfaces using periodic boundary conditions, we adsorb the molecules on finite cluster models of the surface. This allows us to understand how the adsorption energy converges with the cluster size.

The two basic approaches for treating adsorption can be combined using embedding schemes. Assuming that the adsorbate perturbs the system in some limited region, we treat this active region as accurately as possible and use a simpler scheme to describe the effect of the environment. In this subtractive embedding approach, the region of interest (I) is treated with a more accurate method, giving energy contribution E_I^{acc}. The effect of the environment is accounted for by the energy difference $E_{I+II}^{\text{approx}} - E_I^{\text{approx}}$ obtained with the less accurate (cheaper) method:

$$E_{I+II}^{\text{acc}} = E_I^{\text{acc}} + E_{I+II}^{\text{approx}} - E_I^{\text{approx}}. \tag{4.2}$$

The benefit of this approach is that there is no interaction term, the drawback is that the cheaper method must be able to describe the region I at least qualitatively correctly. We use accurate methods (e.g., MP2) for the active region (cluster) whereas the presence of the environment is accounted for using low-level methods. These include various mean-field theories, e.g., Hartree-Fock (HF), or the approximations of density functional theory (DFT). In this part we seek to find how large the active region should be in order to capture the essential part of the interaction. Moreover, we were able to obtain the adsorption energy with the high-level method for several systems using periodic boundary conditions and we are thus able to directly assess how efficient the embedding is.

[1] The validity of this picture thus depends on the localization of the electronic orbitals, which can be estimated to be inversely proportional to the width of the band gap. Hence the cluster approach is most appropriate for wide-gap insulators (see, e.g., Refs. [62],[63]), but it has also been used for metal surfaces [64].

4.1 Computational details

We now summarize the set-up used to obtain accurate estimates of adsorption energies. The finite cluster calculations are performed with the accurate and low-level methods and the set-up is discussed next. Subsequently, we summarize the settings of the methods used for the treatment of the periodic environment.

As the accurate scheme, we use the second order perturbation theory (MP2) on top of a mean-field Hartree-Fock calculation (i.e., HF orbitals are used as reference). Calculations of interaction energies of finite clusters are performed within the Molpro package [65]. The program uses Gaussian orbitals, and the Dunning's correlation-consistent aug-cc-VTZ (AVTZ) basis set is employed for all calculations together with F12-correction to speed up the convergence and account for the electron cusp. The advantage of this combination of F12 and AVTZ basis set is that it leads to MP2 results effectively very close to the complete basis set (CBS) limit [66], thus eliminating the need for extrapolation procedures. Density fitting is also used to speed up more demanding calculations. In order to avoid the basis set superposition error (BSSE) in interaction energies, the counter-poise correction is also employed, i.e. dummy centers (ghost orbitals) are used in all calculations of monomers.

The adsorption energies of adsorbates on two dimensional materials were obtained using the VASP package [67] employing periodic boundary conditions. VASP uses plane wave basis set together with projector-augmented wave (PAW) potentials [68], which reduce the computational effort by approximating the effect of the core electrons. The calculations were performed in a 4×4 supercell to reduce the interaction between periodic images of adsorbed molecules together with the vacuum layer of $20-25$ Å. A $2\times2\times1$ k-point set and a plane-wave basis-set cut-off of 600 eV were used.

We use the Hartree-Fock as the cheap low-level method. However, this scheme does not account for weak dispersion interactions (i.e., long-range electron correlations) which are important for the correct description of processes at surfaces. To account for these, we employ a so-called dispersion correction DFT scheme, in which two-body additive dispersion corrections are added to the DFT energy. The atom-centered dispersion correction scheme is based on the leading order interaction C_6/r^6, where C_6 depends on the polarizability of atoms α. In this work, we use the zero damping DFT-D3 method of Grimme [69], which also includes the C_8/r^8 term, as implemented in the VASP package [67] with parameters for Perdew-Burke-Ernzerhof (PBE) [70] DFT exchange-correlation functional.

The MP2 scheme is known to give satisfying results for interaction energies of systems with localized electrons. However, when the electrons are delocalized, higher-order perturbation theory terms leading to a so-called screening of the interaction become important. This screening was discussed in the context of the Dyson equation, see Eq. 2.26. The random phase approximation (RPA) is a scheme which includes screening and is thus a promising method for the treatment of extended systems. It describes various types of bonding with consistent accuracy. In adsorption systems, underbinding of $10-20\%$ was observed [71], but this can be alleviated by employing the singles corrections [72]. The RPA adsorption energies on two dimensional materials were also obtained using VASP. We note that the application of RPA is not straightforward, especially if one wants

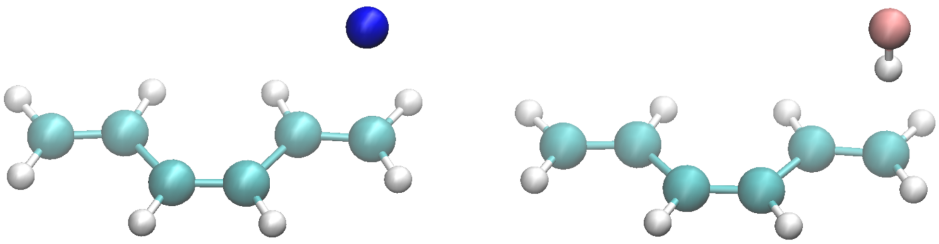

Figure 4.1: Geometries of C_8H_{10} with neon (left) and HF (right).

to converge the results with good precision, since the energies strongly depend on the basis set size, the volume of the supercell, and the k-point set. The RPA interaction energies of the finite clusters were calculated using a code written by Marcin Modrzejewski [73], employing atomic-like localized basis sets and the PBE functional for obtaining Kohn-Sham orbitals. The code computes RPA correlation energies and singles corrections using a highly sophisticated scheme capable of using very large basis sets such as Dunning's augmented correlation-consistent polarized valence quadruple zeta (aug-cc-PVQZ) basis set. All RPA interaction energies of finite clusters were extrapolated towards the complete basis set limit (CBS) according to Ref. [74].

4.2 Polyacetylene

To model adsorption at the end of a one-dimensional chain, we study trans-polyacetylenes of various lengths interacting with small atoms or molecules. Polyacetylenes are hydrocarbons characterized by a chain of conjugated single and double carbon–carbon bonds. The calculations were performed for chains of four different lengths. Two closed-shell adsorbates are studied: neon, which is expected to interact through van der Waals (dispersion) interaction and hydrogen fluoride (HF molecule), where we expect more electrostatic contributions within mean-field approximation. In Fig. 4.1, geometries of C_8H_{10} interacting with both neon and HF molecule are shown.

In Figs. 4.2 and 4.4, we plot binding curves of systems consisting of a C_nH_{n+2} ($n = 2, 4, 6, 8$) molecule and a neon or HF molecule. Obviously, the binding energy is one order of magnitude greater for the HF molecule. The binding curves change less in both cases as we add more atoms at the end of the chain, i.e., increase n towards the maximum of $n = 8$. Note that the convergence of the adsorption energy with the chain length is monotonous for neon but not for hydrogen fluoride.

However, the main point of this section is to assess the convergence of the subtractive embedding scheme. We therefore use the MP2 interaction energies as the "accurate" ones and check the applicability of Hartree-Fock with dispersion correction as the low-level or approximate methods. Specifically, we seek to obtain the MP2 interaction energy on the C_8H_{10} molecule, the shorter molecules are then the "active sites" and the correction term is between the MP2 scheme and

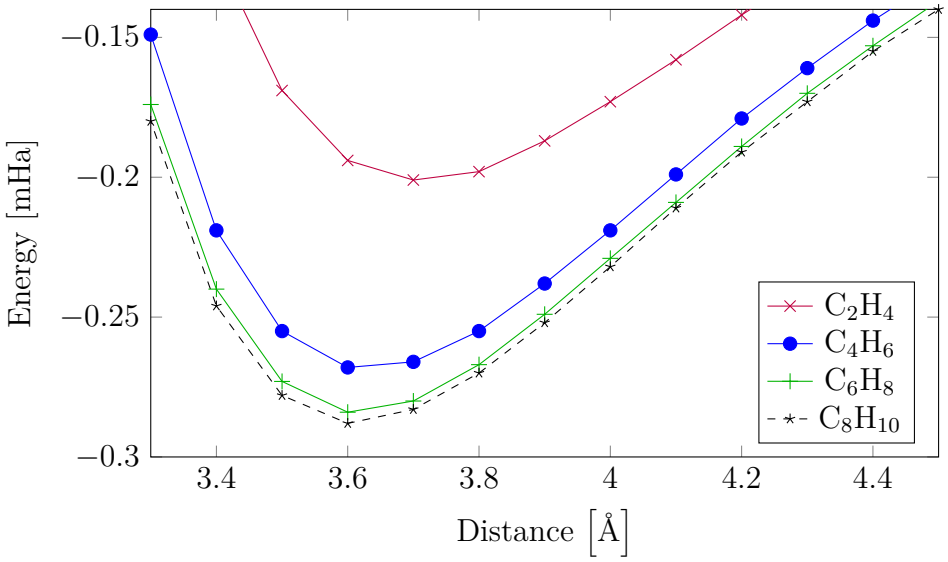

Figure 4.2: Binding curves of a neon atom with four different C_nH_{n+2} molecules. Ab initio MP2 results were obtained with Molpro package.

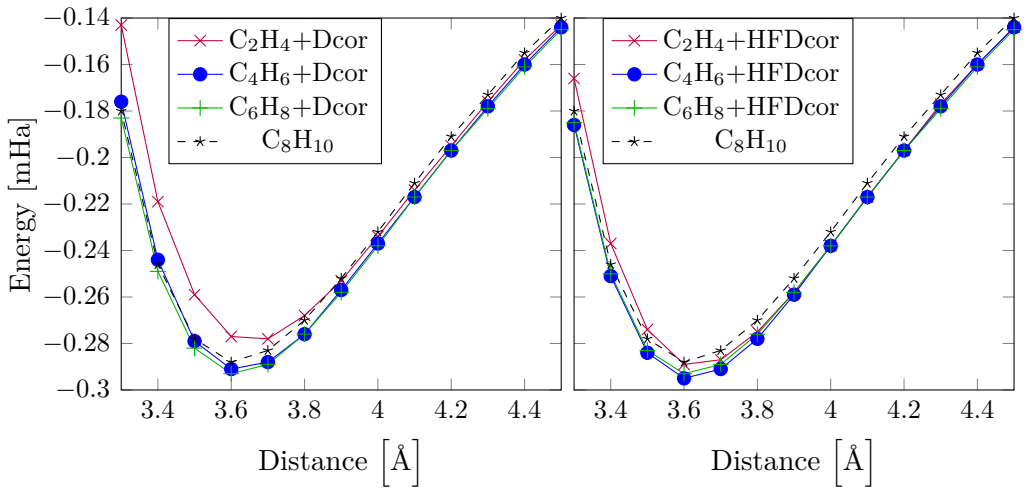

Figure 4.3: Binding curves of a neon atom with four different C_nH_{n+2} molecules with dispersion corrections (left) and Hartree-Fock+dispersion corrections (right) with respect to the reference of C_8H_{10}.

low-level method:

$$E_{\text{int}}^{\text{MP2}}(C_8H_{10}) = E_{\text{int}}^{\text{MP2}}(C_nH_{n+2}) + E_{\text{int}}^{\text{(HF)D}}(C_8H_{10}) - E_{\text{int}}^{\text{(HF)D}}(C_nH_{n+2}),\ n = 2, 4, 6, \tag{4.3}$$

where (HF)D means that either both Hartree-Fock (HF) and dispersion (D) corrections are used, or only dispersion.

From the results (in Figs. 4.3 and 4.5), one can see that the convergence of the combined HFD embedding scheme is very fast, with relative error of less than 3% from the reference already from the smallest chain with $n = 2$. Clearly, the convergence of the dispersion-only scheme is slower for the adsorption of the HF molecule, however, the results for the Ne atom show that a very good agreement of

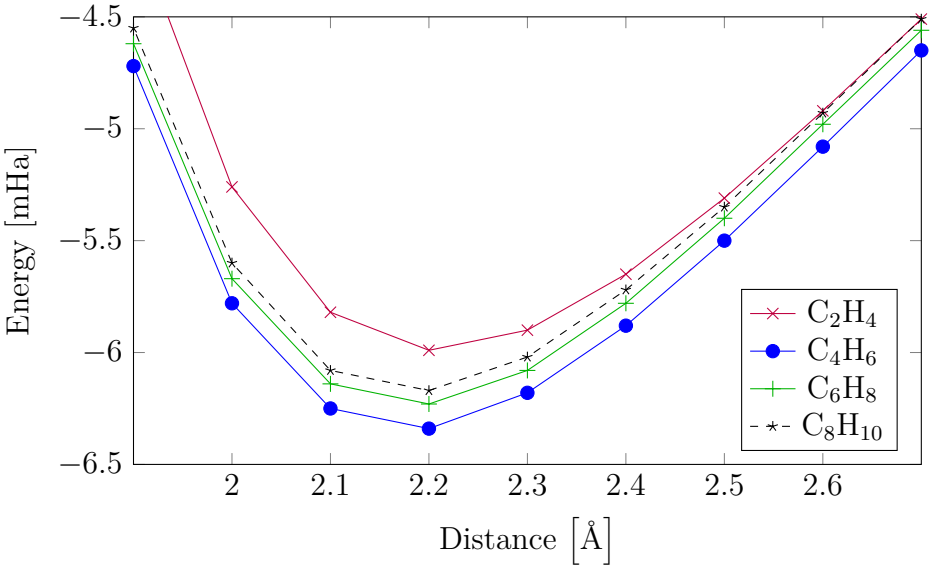

Figure 4.4: Binding curves of an HF molecule with four different C_nH_{n+2} molecules. Ab initio MP2 results were obtained with Molpro package.

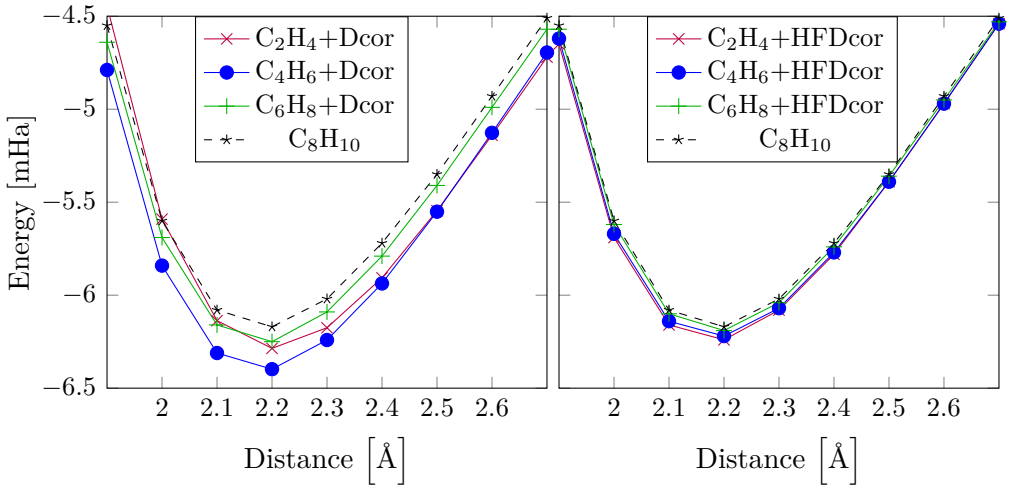

Figure 4.5: Binding curves of an HF molecule with four different C_nH_{n+2} molecules with dispersion corrections (left) and Hartree-Fock+dispersion corrections (right) with respect to the reference of C_8H_{10}.

1% is obtained already with $n = 4$. The binding curves show that the interactions with neon are well described by dispersion corrections, and the HF molecule, due to its high dipole moment, interacts more through the electrostatics captured with Hartree-Fock.

4.3 Two-dimensional systems

In this section, we calculate adsorption energies of small closed-shell systems on two-dimensional clusters of aromatic systems (benzene, naphthalene, etc.) and

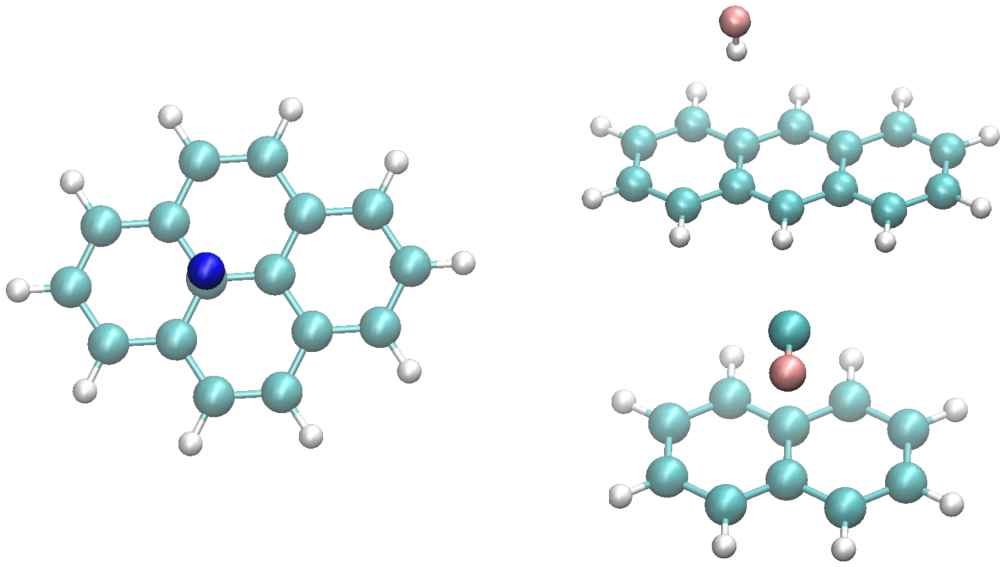

Figure 4.6: Geometries of a four-ring cluster with neon (left), anthracene with a HF molecule (right top) and naphthalene with CO (right bottom). All adsorbates are in top (t) position.

their BN analogs, and study the convergence of adsorption energies towards the infinite 2D sheet limit. The molecules that we use are neon, hydrogen fluoride, and carbon monoxide.

In Tab. 4.1, adsorption (interaction) energies of small atoms and molecules (see Fig. 4.6) on top of carbon atoms of various aromatic systems are presented. The adsorbates are placed 3 Å from the surface, which is close to the energy minimum but not exactly in it. We can observe that the Hartree-Fock results converge faster than MP2 correlation energies for Ne. Therefore, long-range correlations are important for adsorption on graphene. In fact, due to the vanishing gap in graphene, also higher-order correlation effects are important, as we will see later. For the HF molecule and partly also the CO molecule, the Hartree-Fock convergence is similar to MP2. As for polyacetylene, long-range electrostatics is expected to slow down the convergence with respect to the cluster size.

Table 4.1: Adsorption energies for various adsorbates on aromatic π systems, placed at 3 Å distance. The molecules were placed on top of carbon atom and neon either at the top position or above center of the ring. Total adsorption energies are here decomposed into Hartree-Fock (HF) and MP2 correlation contributions. All data are in mHa, computed with the AVTZ basis set (except for coronene, where VTZ basis set is used for carbon atoms).

	benzene		naphthalene		anthracene		coronene	
	HF	MP2	HF	MP2	HF	MP2	HF	MP2
Ne (t)	2.1	−2.1	1.9	−2.5	1.9	−2.6	1.8	−2.8
Ne (c)	1.8	−2.3	1.7	−2.4	1.6	−2.6	1.5	−2.8
HF (t)	−3.1	−0.8	−2.8	−1.3	−2.6	−1.4	−2.0	−1.9
CO (t)	7.0	−7.8	6.2	−10.0	6.2	−10.3	6.7	−11.3

In the case of boron nitride structures, we distinguish the cases when the adsorbates are either on top of B or N atom (see Tab. 4.2). The HF molecule

Table 4.2: Adsorption energies for various adsorbates on top of either B or N atom of aromatic BN π systems, placed at 3 Å distance. For neon also the structure in the middle of the ring was considered. Total adsorption energies are here decomposed into Hartree-Fock (HF) and MP2 correlation contributions. All data are in mHa, computed with the AVTZ basis set.

	borazine		$B_5N_5H_8$		$B_7N_7H_{10}$		$B_{12}N_{12}H_{12}$	
	HF	MP2	HF	MP2	HF	MP2	HF	MP2
Ne (t) B	1.3	−1.3	1.4	−1.7	1.4	−1.7	1.3	−1.9
Ne (t) N	1.7	−1.4	1.7	−1.8	1.7	−1.8	1.7	−2.1
Ne (c)	1.4	−1.6	1.3	−1.7	1.3	−1.9	1.2	−2.0
HF (t) B	−0.7	−1.3	−0.7	−1.5	−0.7	−1.5	−0.0	−1.9
HF (t) N	−1.6	−1.1	−0.8	−1.6	−0.8	−1.6	−0.6	−1.8
CO (t) B	6.8	−6.1	6.6	−7.7	6.6	−7.9	6.8	−9.0
CO (t) N	5.6	−5.3	6.2	−7.4	6.3	−7.5	5.9	−8.5

points perpendicular to the plane of aromatic molecules with H below F. The CO molecule is flat, with the C atom either on top of B or N. Note that the adsorption energies tend to be smaller compared to the carbon substrate, and the convergence behaviour with system size appears to be very similar, with only minor changes. The differences between two variants of adsorbates being on top of either B or N atoms are rather small. There is mostly cca 10−20% relative change, with Hartree-Fock results differing more than MP2 correlations. The highest relative change is 35% in the case of the HF molecule on top of borazine. The convergence with the system size does not seem to be affected with the choice of the B/N top position. Note that absolute values of the individual Hartree-Fock and MP2 adsorption energies are higher for the CO molecule compared to hydrogen fluoride. However, they are of opposite sign and mostly cancel each other out when added together.

Next, the subtractive embedding method is employed, similarly to the previous case of the polyacetylene chains, i.e., we study the convergence of the scheme

$$E_{\text{int}}^{\text{MP2}}(\text{sheet}) \approx E_{\text{int}}^{\text{MP2}}(\text{cluster}) + E_{\text{int}}^{\text{HFD}}(\text{sheet}) - E_{\text{int}}^{\text{HFD}}(\text{cluster}), \tag{4.4}$$

where HFD means that both Hartree-Fock (HF) and dispersion (D) corrections are used.

In Fig. 4.7, we present binding curves for the Ne adsorbate on top of four clusters representing graphene and hBN with applied correction according to the embedding scheme above. At the first glance, it appears that the convergence of the embedding method is faster in the case of boron nitride clusters because the curves lie closer together. This feature is probably due to lower polarizability of BN rings compared to carbon rings. However, note that the curves corresponding to two largest clusters $C_{14}H_{10}$ and $C_{16}H_{10}$ are closer to each other compared to their BN counterparts. This is apparent especially in the region to the right of the minimum of the curves.

In the case of the HF molecule on top of a carbon or boron atom,[2] we can see in Fig. 4.8 that the adsorption energy is approximately three to four times larger

[2]Note that in the following, we only consider the adsorbate in the top position, i.e., either on a carbon atom, or a boron atom, in case of hBN structures.

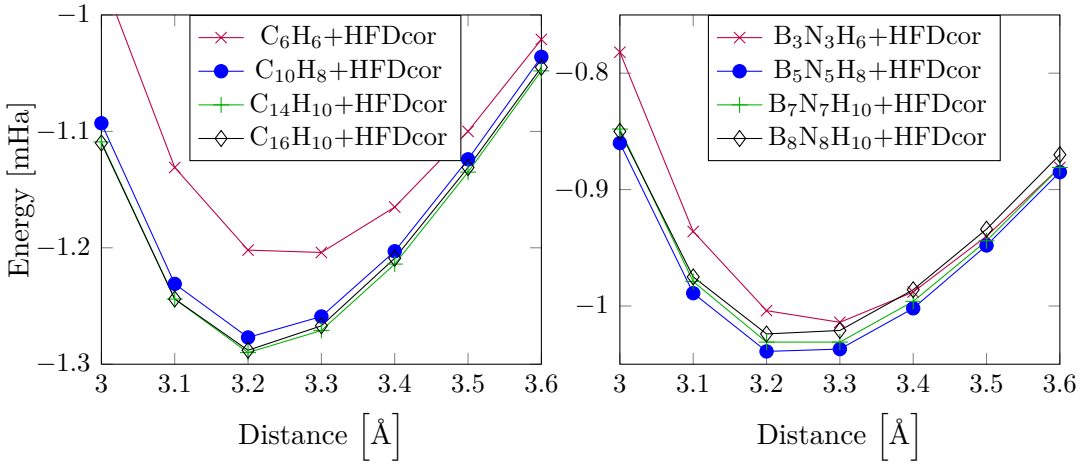

Figure 4.7: Binding curves of a Ne atom on top of graphene (left) and hBN (right) within the subtractive embedding scheme assuming Hartree-Fock+dispersion corrections with respect to the sheet reference.

than in the case of Ne. Furthermore, convergence of the embedding method is clearly slower than in the Ne case, as can be seen from the y-axis range of the respective figures. This is probably due to the high dipole moment of HF interacting electrostatically with the substrate, which is a longer-range effect compared to the van der Waals dispersion dominating in the interaction of Ne. Therefore, we conclude that the embedding scheme works better for the neon atom than for the HF molecule, placed on top of either graphene, or hBN substrates.

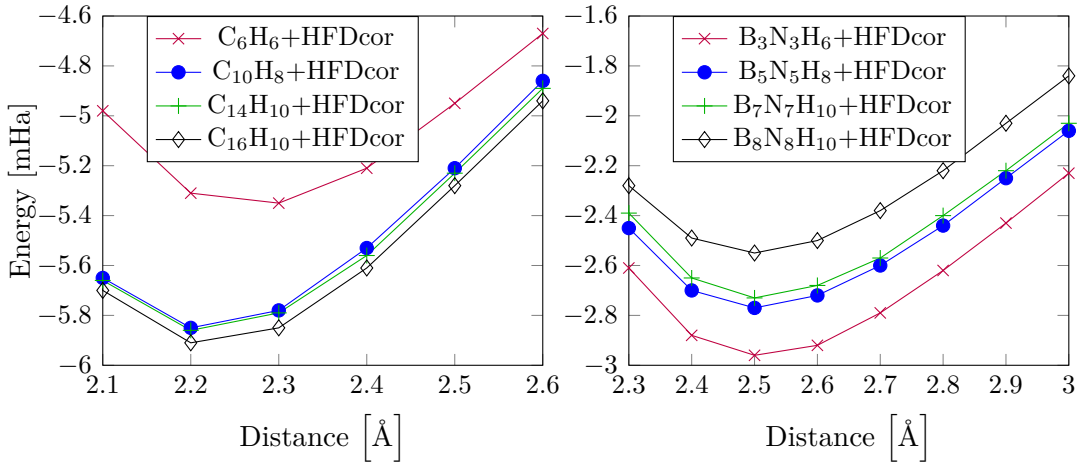

Figure 4.8: Binding curves of an HF molecule on top of graphene (left) and hBN (right) within the subtractive embedding scheme assuming Hartree-Fock+dispersion corrections with respect to the sheet reference.

To assess the accuracy of our embedding scheme, we seek to calculate the correlation energies for the infinite sheet. In case of graphene, due to its semimetallic character, the perturbative evaluation of correlation energies within MP2 breaks down. A natural way to proceed is to use a treatment involving higher-

order terms of the perturbation theory, such as the random phase approximation (RPA). RPA takes screening into account by summing a certain class of Feynman diagrams to infinite order in the Coulomb interaction. It is expected to give good description of dispersion bonded systems, although it is well known that it does not describe covalent bonds very well [75].

For RPA calculations, we set-up the subtractive embedding scheme as follows:

$$E_{\mathrm{int}}^{\mathrm{RPA}}(\mathrm{sheet}) \approx E_{\mathrm{int}}^{\mathrm{RPA}}(\mathrm{cluster}) + E_{\mathrm{int}}^{\mathrm{EXXD}}(\mathrm{sheet}) - E_{\mathrm{int}}^{\mathrm{EXXD}}(\mathrm{cluster}), \tag{4.5}$$

where EXXD means that both exact-exchange energy, i.e., the non-self-consistent Hartree-Fock exchange energy with PBE orbitals (EXX), and dispersion (D) corrections with respect to the sheet reference are used. We note that exact-exchange energy is the Hartree-Fock exchange energy analog using Kohn-Sham orbitals.

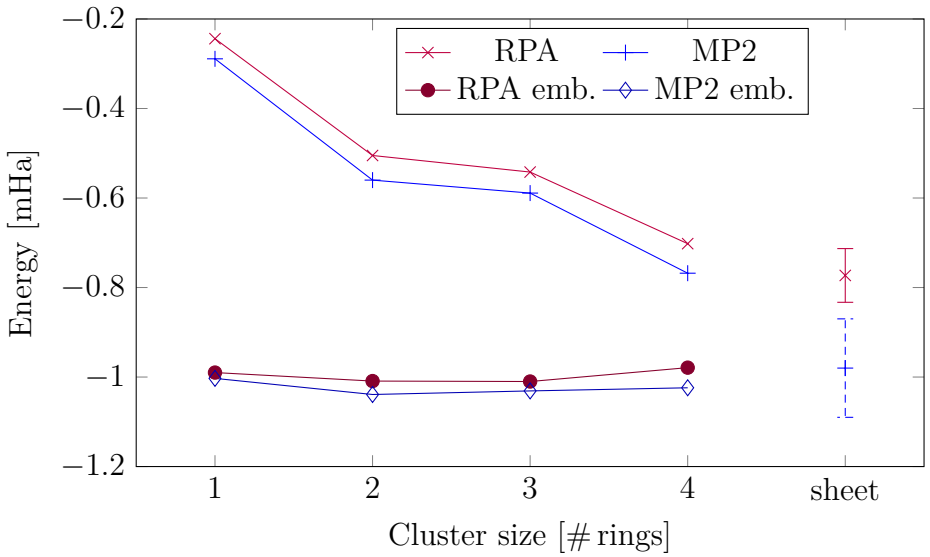

Figure 4.9: Convergence of RPA and MP2 adsorption energies for Ne on top of hBN in 3.2 Å distance towards the infinite sheet limit compared with the RPA and MP2 embedding schemes defined in Eqs. 4.4 and 4.5.

Let us now compare the performance of MP2 and RPA for the adsorption energies of Ne on hBN or graphene. In Figs. 4.9 and 4.10, we plot MP2 and RPA adsorption energies for a Ne atom on top of boron nitride or carbon aromatic structures. We observe that the convergence with the cluster size towards the infinite sheet limit is monotonic and fast. A slow-down in convergence is only seen between the two- and three-ring structure (naphthalene and anthracene), which is due to the fact that the additional ring is farther from the adatom. In the case of hBN, the MP2 energy curve lies close to the RPA curve, however, in the case of carbon rings the MP2 energies seem to diverge with increasing cluster size. This is clearly the case because of the diminishing electronic gap. For RPA, the vanishing gap does not pose a problem and the convergence is similar to the hBN case.

The performance of both MP2 and RPA embedding schemes is fast in the sense that already with the smallest cluster (one ring) the results are within 20% of the infinite limit. However, with the increasing cluster size, the convergence

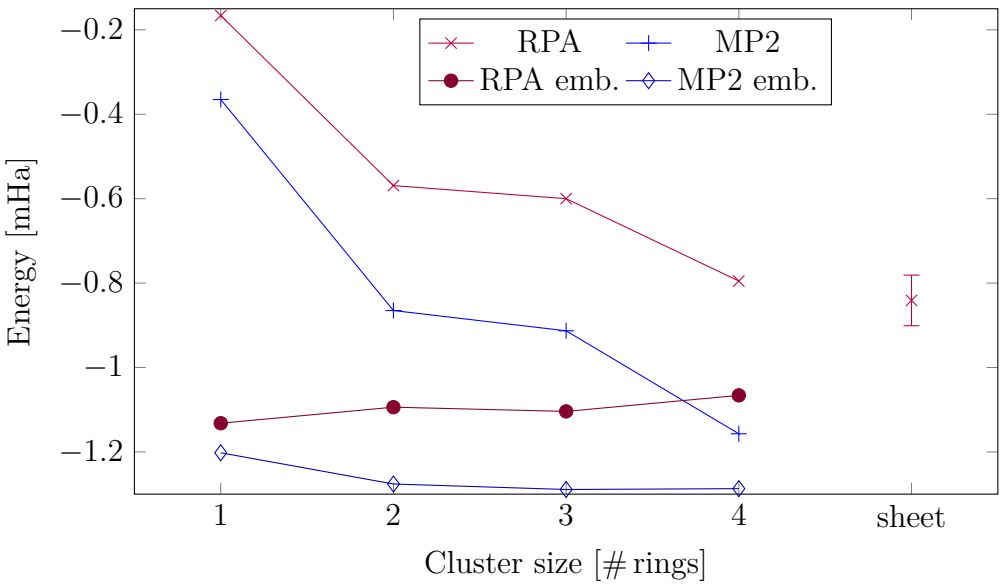

Figure 4.10: Convergence of RPA and MP2 adsorption energies for Ne on top of graphene in 3.2 Å distance towards the infinite sheet limit compared with the RPA and MP2 embedding schemes defined in Eqs. 4.4 and 4.5.

is not entirely satisfactory. When the dispersion corrections are added within the embedding scheme, the dependence of adsorption energies on the cluster size becomes flatter, meaning that the two-body dispersion describes the correlation part of the interactions between Ne and hydrogenated carbon and BN rings reasonably well. Also, note that the vertical error bars in the periodic results mean that the calculations are not completely converged. To obtain more converged results, a higher number of k-points, larger basis set and better PAW potentials need to be used.

In Fig. 4.11, we plot MP2 and RPA adsorption energies for the HF molecule on top of boron nitride structures and observe that the convergence with the cluster size is not monotonic as in the case of BN clusters. In particular, note that this is due to mean-field Hartree-Fock and EXX adsorption energies. Convergence of correlation energies is indeed monotonic. With the corrections of the embedding schemes of Eqs. 4.4 and 4.5, the convergence is smoother but slower. This might be due to the poor performance of the two-body D3 dispersion correction method for the system under study. Also, we note that due to the high dipole moment of the HF molecule, the periodic result can contain an additional error coming from the interaction of periodic images, since the dimensions of the supercell might not be sufficient to make this interaction negligible.

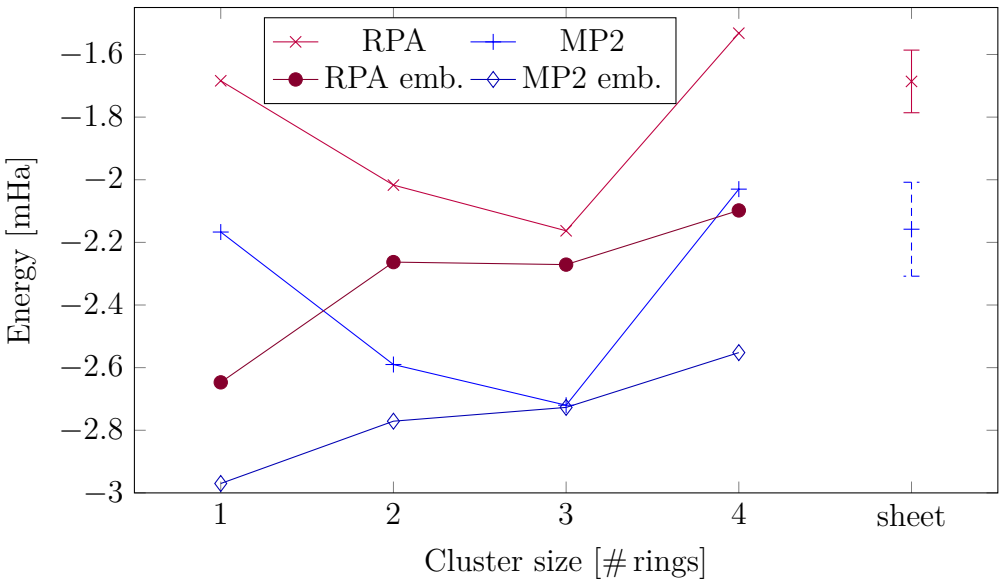

Figure 4.11: Convergence of RPA and MP2 adsorption energies for the HF molecule on top of hBN clusters in 2.5 Å distance towards the infinite sheet limit compared with the RPA and MP2 embedding schemes defined in Eqs. 4.4 and 4.5.

Conclusion

In this thesis, we studied adsorption by means of embedding methods. In particular, two different approaches were investigated: tight-binding and ab initio approach. In the tight-binding approach, we employed the Green's function formalism to obtain local densities of states and adsorption energies, which are quantities of interest in many theoretical and experimental studies. It was found that so-called localized states play a significant role in convergence of adsorption energies with respect to various parameters of studied systems. Their occurrence was discussed based on different tight-binding parameters. It was shown that the properties of these localized states converge very quickly with the system size. Moreover, the energy of these states was found to be dependent on the number of substrate atoms coupled to the adatom. Our results show that while the tight-binding model is not expected to provide reliable results comparable to experiments, it provides physical insight into the essential quantum mechanical phenomena at play. For example, we found a qualitative relation between the adsorption energy and the filling of the substrate energy band.

Within tight-binding approximation, we studied the perturbed-cluster embedding method in LCAO formalism in order to incorporate the effect of the "environment" atoms on a small active site encompassing the adatom and its neighboring atoms. We found explicit formulae for self-energies of finite and infinite chains, allowing us to restrict the Hamiltonian matrix dimension and speed up the calculation of properties of interest. We assessed the applicability of several approximations to self-energy, which is a non-local energy-dependent term in the Hamiltonian, in the simple one-dimensional chain model. The non-homogeneity of the substrate and the presence of an energy gap were found to have a profound effect on the adatom density of states.

We also applied the perturbed-crystal embedding method with the Dyson equation to study theoretically adsorption energies and adatom electron occupancies for a single atom adsorbed to a semi-infinite chain and two-dimensional hexagonal graphene sheet. Explicit results for the hexagonal sheet of graphene were obtained by means of numerical integration of Green's functions, and compared with the case of the one-dimensional chain of atoms.

In the last part of this thesis, state-of-the-art ab initio methods were employed to study adsorption energies and convergence of the subtractive embedding scheme. First, polyacetylene molecules of various lengths were considered as quasi-1D models. The effect of chain length on the interaction of the chain with small adsorbates was assessed. The convergence of the combined Hartree-Fock with dispersion (HF+D) subtractive embedding scheme was found to be very fast, with relative error of less than 3% from the reference already from the smallest chain with $n = 2$. Clearly, the convergence of the dispersion-only scheme was slower for the adsorption of the HF molecule, compared to the Ne atom. The binding curves show that the interactions with neon are well described by dispersion corrections, and the HF molecule, due to its high dipole moment, interacts more through the electrostatics captured with Hartree-Fock.

Finally, convergence of adsorption energies of small adsorbates on top of two-dimensional carbon and boron nitride aromatic structures with increasing cluster

size was studied. We found that whereas for Ne adatom the convergence is monotonic and fast, for the hydrogen fluoride molecule, this is not the case. To obtain the adsorption energy for the infinite hexagonal sheet, we relied on the subtractive embedding method, applying the computationally demanding scheme only for the area (cluster) around the adsorption site and using a simpler mean-field approaches for the rest of the system (environment). In particular, we assessed the self-consistent Hartree-Fock scheme, the non-self-consistent Hartree-Fock with PBE orbitals, also called exact-exchange (EXX), and the DFT-D3 dispersion method. Our higher-level methods for electronic correlation included MP2 and RPA. We found that the convergence of the embedding method towards the infinite sheet limit is slower in the case of the HF molecule compared to the Ne atom. This is probably due to the high dipole moment of HF interacting electrostatically with the substrate, which is a longer-range effect compared to the van der Waals dispersion dominating in the interaction of Ne.

Moreover, we were able to obtain the adsorption energy with the RPA method within periodic boundary conditions for the neon atom on hexagonal BN and graphene surfaces, and for the HF molecule on the hBN surface. The performance of the combined EXX+dispersion embedding scheme was found to be satisfactory. We saw that in the case of graphene, where it is impossible to obtain the MP2 energy for the infinite sheet, the embedding method proved to be a useful tool for obtaining an estimate of the adsorption energy of a small atom or molecule with a surface.

To conclude, in this work, some aspects of the embedding method were discussed along with the effects of a local perturbation on single-electron states of extended systems. Theoretical results from the tight-binding model, including explicit expressions for Green's functions of one- and two-dimensional lattices were obtained and analyzed. The efficiency and applicability of subtractive embedding scheme were also assessed for several systems by using various ab initio methods available in super-computing environments. We found that the studied subtractive embedding scheme is sensitive to the cluster electronic structure convergence. In particular, changes in mean-field adsorption energies of hydrogen fluoride were not reflected by the two-body dispersion scheme. This issue could be alleviated by using a many-body dispersion method instead of the two-body dispersion. Alternatively, one could go even further and use more sophisticated methods as both high- and low-level schemes, e.g., the combination of CCSD(T) and RPA methods. However, we note that the coupled CCSD(T) has a high computational scaling of $O(N^7)$ with the system size, compared to $O(N^3)$ of RPA. Also, as a further extension of this work, various other embedding schemes could be studied, e.g. electrostatic embedding, or projector-based embedding of Manby et al. [15].

Finally, we note that the embedding schemes for adsorption may be useful for studying precision of electronic structure methods. In our calculations, we used different implementations of these methods, and compared results of the order of mHa, obtained by subtracting large numbers of the order of tens of Ha. Thus, embedding schemes for adsorption are sensitive to precision of the used methods leading to opportunities for validation and assessment of precision of different implementations. This ultimately leads to the question of reproducibility of results, which is currently a hot topic for developers [76].

Bibliography

[1] J. Peng, J. Guo, P. Hapala, D. Cao, R. Ma, B. Cheng, L. Xu, M. Ondráček, P. Jelínek, E. Wang, and Y. Jiang. Weakly perturbative imaging of interfacial water with submolecular resolution by atomic force microscopy. *Nature Communications*, 9(122), 2018.

[2] L. Hedin. New method for calculating the one-particle green's function with application to the electron-gas problem. *Physical Review*, 139, 1965.

[3] P.L. Altick and A. E. Glassgold. Correlation effects in atomic structure using the random-phase approximation. *Physical Review*, 133(A632), 1964.

[4] Ch. Møller and M. S. Plesset. Note on an approximation treatment for many-electron systems. *Physical Review*, 46(618), 1934.

[5] J. Čížek. On the correlation problem in atomic and molecular systems. calculation of wavefunction components in ursell-type expansion using quantum-field theoretical methods. *Journal of Chemical Physics*, 45(4256), 1966.

[6] W. M. C. Foulkes, L. Mitas, R. J. Needs, and G. Rajagopal. Quantum Monte Carlo simulations of solids. *Reviews of Modern Physics*, 73:33, 2001.

[7] I.M. Georgescu, S. Ashab, and F. Nori. Quantum simulation. *Reviews of Modern Physics*, 86(153), 2014.

[8] C. A. White, Johnson B. G., P. M.W. Gill, and M. Head-Gordon. Linear scaling density functional calculations via the continuous fast multipole method. *Chemical Physics Letters*, 253(268), 1996.

[9] M. Schutz and H-J. Werner. Low-order scaling local electron correlation methods. IV. linear scaling local coupled-cluster (LCCSD). *Journal of Chemical Physics*, 114(661), 2001.

[10] S. R. White. Density matrix formulation for quantum renormalization groups. *Physical Review Letters*, 69(2863), 1992.

[11] L. Cao and U. Ryde. On the difference between additive and subtractive QM/MM calculations. *Frontiers in Chemistry*, 6(89), 2018.

[12] Q. Sun and K.-L. Chan. Quantum embedding theories. *Accounts of Chemical Research*, 49(12), 2016.

[13] C. Huang, M. Pavone, and E. A. Carter. Quantum mechanical embedding theory based on a unique embedding potential. *Journal of Chemical Physics*, 134(154110), 2011.

[14] F. Libisch, M. Marsman, J. Burgdorfer, and G. Kresse. Embedding for bulk systems using localized atomic orbitals. *Journal of Chemical Physics*, 147(034110), 2017.

[15] F. R. Manby, M. Stella, J. D. Goodpaster, and T. F. Miller. A simple, exact density-functional-theory embedding scheme. *Journal of Chemical Theory and Computation*, 8(8), 2012.

[16] G. Kotliar, S. Y. Savrasov, K. Haule, V. S. Oudovenko, O. Parcolet, and C.A. Marianetti. Electronic structure calculations with dynamical mean-field theory. *Reviews of Modern Physics*, 78(865), 2006.

[17] A.A. Kananenka, E. Gull, and D. Zgid. Systematically improvable multiscale solver for correlated electron systems. *Physical Review B*, 91(121111), 2015.

[18] G. Knizia and K.-L. Chan. Density matrix embedding: A simple alternative to dynamical mean-field theory. *Physical Review Letters*, 109(186404), 2012.

[19] T. B. Grimley and C. Pisani. Chemisorption theory in the Hartree-Fock approximation. *Journal of Physics C: Solid State Physics*, 7, 1974.

[20] A. J. Fisher. Methods of embedding for defect and surface problems. *Journal of Physics C: Solid State Physics*, 21:3229–3249, 1988.

[21] J. E. Inglesfield. *The Embedding Method for Electronic Structure*. First ed. IOP Publishing, Bristol, UK, 2015.

[22] K. von Klitzing, G. Dorda, and M. Pepper. New method for high-accuracy determination of the fine-structure constant based on quantized hall resistance. *Physical Review Letters*, 45(494), 1980.

[23] K. S. Novoselov, A. K. Geim, S. V. Morozov, D. Jiang, Y. Dubonos S. V. Zhang, I.V. Grigorieva, and A.A. Firsov. Electric field effect in atomically thin carbon films. *Science*, 306(5696), 2004.

[24] P. Vogt, P. Padova, C. Quaresima, J. Avila, E. Frantzeskakis, M. C. Asensio, A. Resta, B. Ealet, and G. Le Lay. Silicene: Compelling experimental evidence for graphenelike two-dimensional silicon. *Physical Review Letters*, 108(155501), 2012.

[25] M.E. Davila, L. Xian, S. Cahangirov, A. Rubio, and G. Le Lay. Germanene: a novel two-dimensional germanium allotrope akin to graphene and silicene. *New Journal of Physics*, 16(095002), 2014.

[26] F-f. Zhu, W.-j. Chen, Y. Xu, Ch-l. Gao, D-d. Guan, D. Qian, and S-c. Zhang. Epitaxial growth of two-dimensional stanene. *Nature Materials*, 14, 2015.

[27] F. Karlicky, K. K. R. Datta, M. Otyepka, and R. Zbořil. Halogenated graphenes: Rapidly growing family of graphene derivatives. *ACS Nano*, 7:6434–6464, 2013.

[28] J. Kane and E. J. Mele. Quantum spin hall effect in graphene. *Physical Review Letters*, 95(226801), 2005.

[29] K. Zhang, Y. Feng, F. Wang, Z. Yang, and J. Wang. Two dimensional hexagonal boron nitride (2d-hBN): synthesis, properties and applications. *Journal of Materials Chemistry C*, 46, 2017.

[30] E. N. Economou. *The Physics of Solids: Essentials and Beyond*. First ed. Springer, Berlin, 2010.

[31] F. Bloch. Über die Quantenmechanik der Elektronen in Kristallgittern. *Zeitschrift fur Physik*, 52(555), 1928.

[32] L.-M. Liu, C. Zhang, G. Thornton, and A. Michaelides. Structure and dynamics of liquid water on rutile TiO2(110). *Physical Review B*, 82(161415), 2010.

[33] V. Heine. Electronic structure from the point of view of the local atomic environment. *Solid state physics*, 35, 1980.

[34] J. C. Slater and G. F. Koster. Simplified LCAO method for the periodic potential problem. *Physical Review*, 94(6), 1954.

[35] M. S. Hybertsen and S. G. Louie. Electron correlation in semiconductors and insulators: Band gaps and quasiparticle energies. *Physical Review B*, 34(5390), 1986.

[36] E. N. Economou. *Green's Functions in Quantum Physics*. Third ed. Springer, Berlin, 2006.

[37] A. J. Guttmann. Lattice green's functions in all dimensions. *Journal of Physics A: Mathematical and Theoretical*, 43(305205), 2010.

[38] Y. L. Loh. A general method for calculating lattice green functions on the branch cut. *Journal of Physics A: Mathematical and Theoretical*, 50(405203), 2017.

[39] R. Haydock. The recursive solution of the schrodinger equation. *Solid state physics*, 35, 1980.

[40] T. L. Einstein and J. R. Schrieffer. Indirect interaction between adatoms on a tight-binding solid. *Physical Review B*, 7(8), 1973.

[41] P. Lloyd. Wave propagation through an assembly of spheres: II. the density of single-particle eigenstates. *Proceedings of the Physical Society*, 90(1), 1967.

[42] S. Datta. *Quantum Transport: Atom to Transistor*. First ed. Cambridge University Press, Cambridge, 2005.

[43] G. A. Baraff and M. Schluter. The LCAO approach to the embedding problem. *Solid State Physics*, 19(4383), 1986.

[44] S. G. Davison and M. Steslicka. *Basic Theory of Surface States*. First ed. Clarendon Press, Oxford, 1992.

[45] J. Prachar. Tight-binding model and its application for molecular electronics and transport in mesoscopic systems. Bachelor thesis, Faculty of Mathematics and Physics, Charles University, 2006.

[46] R. Bass. The Green's function for a finite linear chain. *Journal of Mathematical Physics*, 26(3068), 1985.

[47] N. M. R. Peres, T. Stauber, and J. M. B. Lopes dos Santos. Lattice Green's function approach to the solution of the spectrum of an array of quantum dots and its linear conductance. *Physical Review B*, 79(035107), 2009.

[48] M. Abramowitz and I. A. Stegun. *Handbook of Mathematical Functions*. Revised. Dover Publications, New York, 1965.

[49] T. Morita. Useful procedure for computing the lattice Green's function-square, tetragonal, and bcc lattices. *Journal of Mathemathical Physics*, 12(1744), 1971.

[50] T. Morita and T. Horiguchi. Calculation of the lattice Green's function for the bcc, fcc, and rectangular lattices. *Journal of Mathemathical Physics*, 12(986), 1971.

[51] C. Bena and G. Montambaux. Remarks on the tight-binding model of graphene. *New Journal of Physics*, 11(095003), 2009.

[52] S. R. Power and M. S. Ferreira. Electronic structure of graphene beyond the linear dispersion regime. *Physical Review B*, 83(155432), 2011.

[53] T. Horiguchi. Lattice Green's functions for the triangular and honeycomb lattices. *Journal of Mathemathical Physics*, 13(1411), 1972.

[54] T. G. Pedersen and J. G. Pedersen. Self-consistent tight-binding model of B and N doping in graphene. *Physical Review B*, 87(155433), 2013.

[55] M. Topsakal, E. Akturk, and S. Ciraci. First-principles study of two- and one-dimensional honeycomb structures of boron nitride. *Physical Review B*, 79(115442), 2009.

[56] T. B. Grimley. The wave mechanics of the surface bond in chemisorption. *Advances in Catalysis*, 12(1), 1960.

[57] S. G. Davison and K. W. Sulston. *Green Function Theory of Chemisorption*. First ed. Springer, Dordrecht, 2006.

[58] W. A. Harrison. *Electronic Structure and the Properties of Solids: The Physics of the Chemical Bond*. Second ed. Dover Publications, New York, 1989.

[59] S. Ihnatsenka and G. Kirczenow. Dirac point resonances due to atoms and molecules adsorbed on graphene and transport gaps and conductance quantization in graphene nanoribbons with covalently bonded adsorbates. *Physical Review B*, 83(245442), 2011.

[60] S. Moukouri and A. I. Noguera. Theoretical study of small mgo clusters. *Zeitschrift fur Physik D - Atoms, Molecules and Clusters*, 24:71–79, 1992.

[61] R. A. van Santen and I. Tranca. How molecular is the chemisorptive bond? *Physical Chemistry Chemical Physics*, 18:20868–20894, 2016.

[62] B. Li, A. Michaelides, and M. Scheffler. How strong is the bond between water and salt? *Surface Science*, 602:L135, 2008.

[63] A. D. Boese and J. Sauer. Accurate adsorption energies of small molecules on oxide surfaces: Co-mgo(001). *Physical Chemistry Chemical Physics*, 15:16481, 2013.

[64] A. Groß. *Theoretical Surface Science: A Microscopic Perspective*. First ed. Springer, Berlin, 2009.

[65] H.-J. Werner, P. J. Knowles, G. Knizia, F. R. Manby, and M. Schutz. Molpro: a general-purpose quantum chemistry program package. *WIREs Computational Molecular Science*, 2:242–253, 2012.

[66] J. Hofierka. Lattice energies of molecular solids. Bachelor thesis, Faculty of Mathematics and Physics, Charles University, 2017.

[67] G. Kresse and J. Furthmüller. Efficient iterative schemes for ab initio total-energy calculations using a plane-wave basis set. *Physical Review B*, 54:11169, 1996.

[68] G. Kresse and J. Joubert. From ultrasoft pseudopotentials to the projector augmented wave method. *Physical review B*, 59, 1999.

[69] S. Grimme, J. Antony, S. Ehrlich, and H. Krieg. A consistent and accurate ab initio parametrization of density functional dispersion correction (DFT-D) for the 94 elements h-pu. *Journal of Chemical Physics*, 132(154104), 2010.

[70] J. P. Perdew, K. Burke, and M. Ernzerhof. Generalized gradient approximation made simple. *Physical Review Letters*, 77(3865), 1996.

[71] X. Ren, A. Tkatchenko, P. Rinke, and M. Scheffler. Beyond the random-phase approximation for the electron correlation energy: The importance of single excitations. *Physical Review Letters*, 106:153003, 2011.

[72] J. Klimeš, M. Kaltak, E. Maggio, and G. Kresse. Singles correlation energy contributions in solids. *Journal of Chemical Physics*, 143(102816), 2015.

[73] M. Modrzejewski, S. Yourdkhani, and J. Klimeš. Random phase approximation for many body noncovalent systems. *In preparation*, 2019.

[74] T. Helgaker, A. Halkier, P. Jørgensen, W. Klopper, and J. Olsen. Basis-set convergence of the energy in molecular Hartree–Fock calculations. *Chemical Physics Letters*, 302:437–446, 1999.

[75] J. Klimeš. Lattice energies of molecular solids from the random phase approximation with singles corrections. *Journal of Chemical Physics*, 145(094506), 2016.

[76] K. Lejaeghere et al. Reproducibility in density functional theory calculations of solids. *Science*, 351(6280), 2016.

[77] F. Sols, M. Macucci, U. Ravaioli, and K. Hess. Theory for a quantum modulated transistor. *Journal of Applied Physics*, 66(3892), 1989.

[78] R. Zeller, J. Deutz, and P. H. Dederichs. Application of complex energy integration to selfconsistent electronic structure calculations. *Solid state communications*, 44(7), 1982.

[79] J. Lawlor. *Electronic properties of doped carbon-based nanostructures.* PhD thesis, Trinity College Dublin, 2016.

A. Calculation of Green's functions using complex analysis

A.1 Infinite chain

We want to solve the following integral:

$$\hat{g}_{\mathrm{j,l}}(E) = \frac{a}{2\pi}\int_{-\pi/a}^{\pi/a} dk \frac{e^{ika(j-l)}}{E + i\eta - \epsilon_0 - 2\tau\cos(ka)} = \frac{a}{4\pi\tau}\int_{-\pi/a}^{\pi/a} dk \frac{e^{ika(j-l)}}{\cos(ka) + \frac{E+i\eta-\epsilon_0}{2|\tau|}}, \tag{A.1}$$

where we assumed that $\tau < 0$. We proceed by introducing the complex variable $w = e^{ika}$, so that $2\cos(ka) = w + w^{-1}$ and rewriting the integral as a contour integral along the unit circle

$$\hat{g}_{\mathrm{j,l}}(z) = \frac{1}{2\pi i\tau}\oint_{|w|=1} dw \frac{w^{|j-l|}}{w^2 + 2xw + 1}, \tag{A.2}$$

with the notation $x = \frac{z-\epsilon_0}{2|\tau|}$ and $z = E + i\eta$.

The integrand has two poles:

$$w_\pm = -x \pm \sqrt{x^2 - 1}, \tag{A.3}$$

which satisfy $w_+ w_- = 1$, meaning that only one of them lies inside the unit circle. We have to keep a small imaginary $\eta = \mathrm{Im}\{x\}$, since for $x \in \mathbb{R}\,\&\,x \in (-1, 1)$ both roots lie on the unit circle, and the integral above is not well defined.

We note that if x is real (i.e., in the limit $\eta \to 0+$)

$$|w_\pm|^2 - 1 = 2\sqrt{x^2-1}\left(\sqrt{x^2-1} \mp x\right) < 2\sqrt{x^2-1}\,(|x| \mp x) \text{ for } |x| > 1, \tag{A.4}$$

meaning that w_+ is inside the unit circle for $\mathrm{Re}\{x\} > 1$ and w_- lies inside the unit circle $\mathrm{Re}\{x\} < -1$.

Then, for $\mathrm{Re}\{x\} \in (-1, 1)$, w_+ is inside the unit circle provided that η is a positive infinitesimal (this is easy to show because if $\mathrm{Re}\{x\} = 0$ then $w_+ = i(1-\eta)$ since $\eta^2 = 0$).

Therefore, we obtain by the method of residues

$$\hat{g}_{\mathrm{j,l}}(z) = \frac{1}{2\pi i|\tau|} 2\pi i\,\mathrm{Res}_{w_+} \frac{w^{|j-l|}}{(w - w_+)(w - w_-)} = \frac{w_+^{|j-l|}}{\tau(w_+ - w_-)} \tag{A.5}$$

The resulting (retarded) Green's function, which is obtained by a limiting procedure, is valid for the scaled energy parameter $x = \frac{E-\epsilon_0}{2|\tau|} \in [-1, 1]$, defining the only continuous part of the spectrum (band) has the form

$$\hat{g}_{j,l}(E) = \frac{-i}{2|\tau|\sqrt{1-x^2}}(-x + i\sqrt{1-x^2})^{|j-l|}, \tag{A.6}$$

where the minus sign in the numerator is fixed by the requirement that the local density of states

$$n(E) = -\frac{1}{\pi}\,\mathrm{Im}\, g_{jj}(E) \tag{A.7}$$

is positive within the continuum band.

A.2 Semi-infinite chain

We evaluate the integral

$$\hat{g}_{\mathrm{j,l}}(E) = \frac{a}{2\pi}\int_{-\pi/a}^{\pi/a} dk \frac{\sin(jka)\sin(lka)}{E + i\eta - \epsilon_0 - 2\tau\cos(ka)}. \tag{A.8}$$

for $j = l = 1$. Here we denote $x = \frac{z-\epsilon_0}{2|\tau|}$ with $z = E + i\eta$. Substituting $w = e^{ika}$ as above, we obtain

$$\hat{g}_{1,1}(z) = \frac{i}{4\pi|\tau|}\oint_{|w|=1} dw \frac{(w^2-1)^2}{w^2(w^2+2xw+1)}. \tag{A.9}$$

The integrand has three poles:

$$w_0 = 0 \tag{A.10}$$

$$w_\pm = -x \pm \sqrt{x^2-1}, \tag{A.11}$$

which satisfy $w_+ w_- = 1$, meaning that only one of the pair $w_\pm$ lies inside the integration contour (unit circle). As discussed in detail in the preceding section, provided that x includes a positive infinitesimal η, w_+ lies inside for $\mathrm{Re}\{x\} > -1$ and w_- lies inside otherwise. The residues of the integrand at the poles are given by

$$\mathrm{Res}_{w_0} \frac{(w^2-1)^2}{w^2(w^2+2xw+1)} = -2x \tag{A.12}$$

$$\mathrm{Res}_{w_\pm} \frac{(w^2-1)^2}{w^2(w^2+2xw+1)} = \pm 2\sqrt{x^2-1}. \tag{A.13}$$

By the residue theorem, we can write:

$$\hat{g}_{1,1}(z) = \frac{i}{4\pi|\tau|} 2\pi i \left(\mathrm{Res}_{w_0} \frac{(w^2-1)^2}{w^2(w^2+2xw+1)} + \mathrm{Res}_{w_\pm} \frac{(w^2-1)^2}{w^2(w^2+2xw+1)} \right). \tag{A.14}$$

Therefore, the result is

$$\hat{g}_{1,1}(z) = \frac{1}{|\tau|} \begin{cases} (x - i\sqrt{1-x^2}) & \text{if } |x| \le 1 \\ (x - \mathrm{sgn}x\sqrt{x^2-1}) & \text{if } |x| > 1. \end{cases} \tag{A.15}$$

B. Eigenvalues and eigenvectors of a tridiagonal Toeplitz matrix

We wish to calculate the eigenvalues of a symmetric tridiagonal matrix

$$A = \begin{pmatrix} U & \tau & 0 & \cdots & 0 \\ \tau & U & \tau & 0 & \vdots \\ 0 & \tau & \ddots & \cdots & \vdots \\ \vdots & \cdots & \tau & U & \tau \\ 0 & \cdots & 0 & \tau & U \end{pmatrix},$$

of order N with U, τ real or complex constants. The eigenvalue equation $Av = \lambda v$ transforms into a difference equation for the components $v_1, v_2, ..., v_N$ of the eigenvector v:

$$\tau(v_{i-1} + v_{i+1}) + (U - \lambda)v_i = 0,\ i = 1, \ldots, N, \tag{B.1}$$

where we defined that $v_0 = v_{N+1} = 0$. The solution of this linear equation with constant coefficient can be easily found by writing:

$$v_i = am_1^i + bm_2^i, \tag{B.2}$$

with a, b are constants and m_1, m_2 are given by roots of the quadratic equation:

$$\tau(m^2 + 1) + (U - \lambda)m = 0. \tag{B.3}$$

First, since $v_0 = v_{N+1} = 0$, we must have $m_1 \neq m_2$ (otherwise if $m_1 = m_2$ then necessarily $a = b = 0$ and $v = 0$) and:

$$a + b = 0$$
$$am_1^{N+1} + bm_2^{N+1} = 0$$

with solutions:

$$\frac{m_1}{m_2} = e^{\frac{2ik\pi}{N+1}},\ k = 1...N,$$

which together with $m_1 m_2 = 1$ leads to

$$m_1 = e^{\frac{ik\pi}{N+1}}$$
$$m_2 = e^{\frac{-ik\pi}{N+1}}.$$

Then, since we know that

$$m_1 + m_2 = \frac{\lambda - U}{\tau},$$

we can write the general form of the eigenvalues of a symmetric tridiagonal Toeplitz matrix:

$$\lambda_k = U + 2\tau \cos\left(\frac{k\pi}{N+1}\right),\ k = 1, 2, 3..., N, \tag{B.4}$$

interestingly, these are roots of the Chebyshev polynomials of second kind of degree n. The eigenvector corresponding to λ_k is then given by [77]

$$v_k(N) = A\left\{\sin\left(\frac{k\pi}{N+1}\right), \sin\left(\frac{2k\pi}{N+1}\right), ..., \sin\left(\frac{Nk\pi}{N+1}\right)\right\}, \tag{B.5}$$

where the normalization factor can be found in, e.g. Appendix of [77].

C. Analytic expressions for the Green's function of hexagonal lattices

Horiguchi and Morita ([53], [50]) expressed Green's functions recursively for the triangular and honeycomb lattices in terms of the complete elliptic integrals of the first and second kind.

Their expression for the onsite (diagonal) Green's function of a triangular lattice reads

$$g_{00}(z) = \frac{1}{4\pi} g(z) \widetilde{\mathcal{K}}[k(z)], \tag{C.1}$$

where $g(z) = \frac{8}{\sqrt{(\sqrt{2z+3}-1)^3(\sqrt{2z+3}+3)}}$, and $k(z) = \frac{1}{2} g(z) \sqrt[4]{2z+3}$.

Concerning the honeycomb lattice, Horiguchi used a substitution $z' = \frac{z^2-3}{2}$ to obtain the onsite Green's function

$$g_{00}(z) = \frac{z}{4\pi} g(z') \widetilde{\mathcal{K}}[k(z')]. \tag{C.2}$$

Also, the analytic continuation of the complete elliptic integrals of the first kind $\mathcal{K}$ needs to be used in order to capture the behavior of the real part of the Green's function inside the band, namely:

$$\widetilde{\mathcal{K}}[k(z')] = \begin{cases} \mathcal{K}[k(z')] & \text{for } \operatorname{Im} k \cdot \operatorname{Im} z' < 0 \\ \mathcal{K}[k(z')] + 2i\mathcal{K}[\sqrt{1-k^2(z')}] & \text{for } \operatorname{Im} k > 0\,, \operatorname{Im} z' > 0 \\ \mathcal{K}[k(z')] - 2i\mathcal{K}[\sqrt{1-k^2(z')}] & \text{for } \operatorname{Im} k > 0\,, \operatorname{Im} z' < 0 \end{cases} \tag{C.3}$$

The DOS exhibits the characteristic discontinuity at the band edges and $\operatorname{Re}\{g\}$ has a logarithmic singularity. There are singular points within the band where the $\operatorname{Re}\{g\}$ exhibits a discontinuity and the DOS has a logarithmic singularity [36].

Alternatively, Pedersen [54] obtained the following expressions equivalent to those above for $t = 1$:

$$g_{00}(z) = \operatorname{sgn}(z) \operatorname{Re}[3\mathcal{G}(|z|) + \mathcal{G}(-|z|)] + i \operatorname{Im}[\mathcal{G}(|z|) - \mathcal{G}(-|z|)], \tag{C.4}$$

with

$$\mathcal{G}(z) = \frac{\sqrt{z}}{2\pi i t^{3/2}} \mathcal{K}\left[\frac{(3t-z)(t+z)^3}{16 z t^3}\right]. \tag{C.5}$$

In Fig. 3.8, the numerical evaluation of the above expression in Mathematica program is presented. The plot corresponds to the one obtained from numerical integration as discussed in the main text.

D. Contour integration of Green's functions

We seek to calculate the integral

$$I = -\frac{2}{\pi} \operatorname{Im} \int_{-\infty}^{E_F} G_{ii}(E + i\eta) dE. \tag{D.1}$$

First, we recall that the retarded Green's functions $G_{ii}(E + i\eta)$ are by their definition analytic in the upper-half of the complex energy plane defined by $y > 0$ for $z = x + iy$. The current integral lies a small distance $i\eta$ from the real axis. The choice of the path used in a numerical calculation has to be a compromise between an optimally smooth integrand, calling for a path far away from the real axis, and between an optimally short path [78]. We take a straight line from E_F to infinity complemented by a quarter-circle which has to be calculated analytically, see Fig. D.1. In many applications the infinite quarter-circle will give a vanishing contribution.

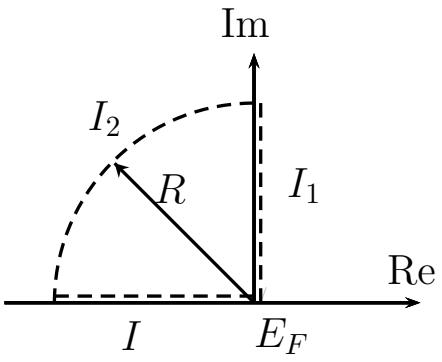

Figure D.1: The complex energy plane with the dashed line representing the integration contour. Note that the section along the real line is shifted upwards by η. The integral is taken counter-clockwise. The contour encloses no singularities and has an arc of radius $R \to \infty$.

From Cauchy's theorem it follows that $I = -I_1 - I_2$. The integral I_2 along the arc can be solved by switching the Green function to polar coordinates $z = Re^{i\theta}$. Following from the definition $G = (E - H)^{-1}$ clearly $G_{ii}(z) \approx 1/z$, therefore

$$I_2 \approx \int_{\pi/2}^{\pi} d\theta \frac{iRe^{i\theta}}{Re^{i\theta}} = i\frac{\pi}{2}. \tag{D.2}$$

If the integrand has the form $\log\det\left(\hat{I} - \hat{g}\hat{V}\right) = \operatorname{Tr}\log\left(\hat{I} - \hat{g}\hat{V}\right)$, as in the case of adsorption energy calculations, the asymptotic behaviour leads to $I_2 = \frac{-i\pi}{2} \operatorname{Tr} \hat{V} = 0$, since V is a traceless matrix.

Let us note that if the integrand is a product of two or more Green's functions, the integral I_2 vanishes as the integrand behaves as $1/R^2$ or faster.

The integral over the imaginary axis I_1 has the form

$$I_1 = i \int_{\eta}^{\infty} G_{ii}(E_F + iy) dy, \tag{D.3}$$

which leads to

$$I = -\frac{2}{\pi}\,\mathrm{Im}\left(-i\int_{\eta}^{\infty} G_{ii}(E_F+iy)dy - i\frac{\pi}{2}\right) = 1+\frac{2}{\pi}\,\mathrm{Re}\int_{\eta}^{\infty} G_{ii}(E_F+iy)dy. \quad \text{(D.4)}$$

It is useful to perform an additional change of variables in order to change the integration limits to a finite range to facilitate numerical evaluation (see Refs. [78] and [79])

$$y = \frac{1+\eta-s}{s},\ dy = -\frac{1+\eta}{s^2}ds, \quad \text{(D.5)}$$

which leads to

$$I = 1 + \frac{2}{\pi}\,\mathrm{Re}\int_0^1 ds\frac{1+\eta}{s^2}G_{ii}\left(E_F + i\frac{1+\eta-s}{s}\right). \quad \text{(D.6)}$$